CATALYTIC CO2 CYCLOADDITION WITH EPOXIDES INTO CYCLIC CARBONATES: SYNERGIES FROM COMPUTATIONAL TO EXPERIMENTAL STUDIES

Md Bin Yeamin

UNIVERSITAT ROVIRA i VIRGILI

Catalytic CO_2 Cycloaddition with Epoxides into Cyclic Carbonates: Synergies from Computational to Experimental Studies

MD BIN YEAMIN

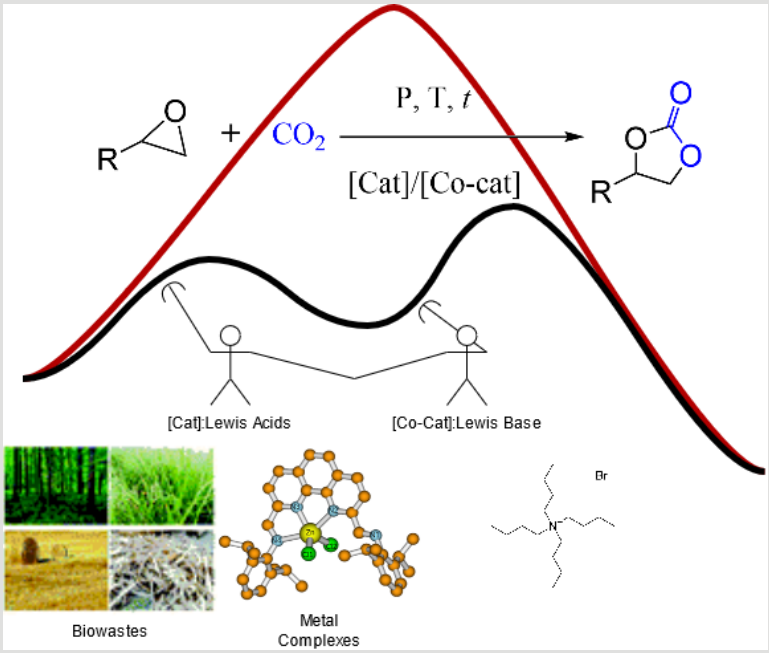

DOCTORAL THESIS
2021

Md Bin Yeamin

Catalytic CO_2 Cycloaddition with Epoxides into Cyclic Carbonates: Synergies from Computational to Experimental Studies

PhD Thesis

Supervised by
Dr. Mar Reguero & Dr. Anna M. Masdeu Bultó

Grupo de Química Quàntica & Grupo de Innovación en Catálisis (innCAT)
Departamento de Química Física i Inorgànica

UNIVERSITAT ROVIRA i VIRGILI

Tarragona, July 2021

UNIVERSITAT ROVIRA i VIRGILI

Department of Physical and Inorganic Chemistry

Dr. M. Mar Reguero, Professor at Quantum Chemistry group and Dr. Anna M. Masdeu Bultó, Professor at Innovation in Catalysis (innCAT) group of the Department of Physical and Inorganic Chemistry of the University of Rovira I Virgili.

We STATE that the present study, entitled "Catalytic CO_2 Cycloaddition with Epoxide into Cyclic Carbonates: Synergies from Computational to Experimental Studies", presented by Md Bin Yeamin for the award of the degree of Doctor, has been carried out under our joint supervision at the Department of Physical and Inorganic Chemistry of this university.

Tarragona, 02 June 2021

Doctoral Thesis Supervisors

M. Reguero

Dr. M. Mar Reguero

Dr. Anna M. Masdeu Bultó

Acknowledgement /Agradecimientos

A short visit to a native (Bangladeshi) mate here in Tarragona in 2013 later was found as the inspiration to find a doctoral fellowship which started in 2017 with a first contact to Dr. M. Mar Reguero, eventually one of my supervisors. Also, Tarragona motivated me with its unprecedented scientific endeavor on CO_2 chemistry.

Immediately after commencing the work, I realized that I often fail to reach a verbal scientific communication to lead a decision. I came to know besides the technical know-how, I also need training on management and/or negotiation conducted by effective communications, I had very little. So, I had many sessions with Mar to make my first calculations running. However, I think, over the time I became dominant to take over. On many intense debates with you, I defeated. Anyhow, you did tolerate me to be so dear to say "No" on many occasions which allowed me to go with the best possible solutions at hand. My pleasure, perhaps, I could put those momenta forward.

Professor Anna M. Masdeu Bultó, my supervisor from Innovation in Catalysis (innCAT) group is a jolly person. Talking to you over the years have been a great pleasure to me. At the first day, you say, get the degree whatever you have after three years! Was a strong moral support for this student, isn't it! Your strong command over the relevant literature was so useful to kick the projects off. Very many social activities headed by you helped to overcome the tension of workplace hurdles. You instruct very

clear, I enjoyed! Often seen, you quickly get my difficulties, was wonderful.

Quantum Chemistry weekly meetings led by Professor Coen de Graaf released a lot of worries to manage my computational tasks, and I discovered Coen also gives suggestions to me! My sincere thanks! You said, knowing the strategies to deal with, PhD is not that difficult. Many understandings became clear without noticing. You know to lead students without dissipating energy, I oversaw over the years. Prof. Dr. Maria Besora Bonet helped me to understand some of the computational strategies were crucial to reach out the computational data analyses of this Thesis. I was benefited from the comments of Prof. Rosa Caballol Lorenzo on how to cite the same literature for multiple times to refer to its different pages. There were many more helps from the faculties; I could not mention here.

Among the mates from Quantum Chemistry (QC) group, I had many helps from Dr. Albert Solé Daura, Antoni Salom Català, Dr. Antonio Moreno Vicente, Dr. Marc Alías Rodríguez. Also, thanks to my office mates from Despacho 203: Dr. Jiangfang Wu offered me Chinese herbal tea and Yannick Rosello Marin corrected the background color of a paragraph. Dr. Almudena Notario Estevez took a care of using "Dispersion correction" keyword in Gaussian. In the beginning days in wet lab, Raquel Rivas Del Valle became a labmate beyond her duty to technical laboratory issues. Dr. Myriam Yasmine Souleymanou helped me in a purification step of ligand preparation. Then, a nice time passed with my labmate Nassima El Aouni. Good luck to you! Maria Elena Moschiano,

a colleague from University of Naples Federico II, Italy, worked with me here at University Rovira I Virgili (URV). Thanks for your accompany, Lady!

Also, I am grateful to Professor Carmen Claver for her support to conduct this research. So many comments from Professor Cyril Godard and from innCAT team were so useful to guide modeling my catalytic reactions from a real chemical model viewpoint. A collaboration with Prof. Francesco Ruffo, University of Naples Federico II, Italy is acknowledged with thanks.

From the technical team of QC group, José Carlos Ortiz Alba helped me with his decent service on the use of the cluster computer, Maginet and its cuota policy. Moises Alvarez Moreno suggested on the interoperability capacities among various application softwares and file managements. Elisenda Mas Ferraté did tolerate many reclaims of solftware installations and office accessory issues.

Coming back to family, my beloved wife Mehenaz Tabassum Trisha gifted me a son, Madyan Yeamin, born at Tarragona in March 2018. Among many helps, Mehenaz sacrificed her spicy food due to my recent health issues also for the sake of this Thesis, I believe. Thanks to Mom, who holds me, and to the departed soul of my father, who enlightened me, in particular, insisted not to have break in studies. So, I am moving on! Also, many thanks to Mohammad Shaiful Alam Amin and his family who supported us mentally and to administrative technological accesses all along this stay here in the neighborhood of Sant Pere I Sant Pau.

Cada vez que vine a España, no regresé con las manos vacías. Observaba, hasta lo más profundo, la sociedad española para descubrirla en toda su profundidad. Me aventuré en todo lo posible. Ello me enseñó a pensar con lógica, y a conocer las leyes fundamentales de dicha sociedad. Dándome cuenta atreves de las acciones institucionales de la carencia en la sociedad en que yo vivía. Estoy muy contento de pasar más tiempo aquí en Tarragona donde he tenido la oportunidad de supervisar las actividades químicas de los alrededores.

Nuestro vecino, Francisco Fernández Mayo y su esposa Ana Maria López son nuestro primer contacto de 24 horas para cualquier solución de problemas sociales/administrativos. Muchas gracias a su hospitalidad. Mi español llegó a un nuevo nivel, gracias a su tutoría natural. Me habéis ayudado de muchas maneras, ¡no puedo enumerarlas aquí!

"Without theory to guide him the experimenter is as lost as a sailor setting out without compass or rudder"

Leonardo da Vinci

Funding Agencies

Fundació Catalunya La Pedrera

UNIVERSITAT ROVIRA i VIRGILI

Table of Contents

Abstract

CO_2 utilization as a chemical feedstock has been proven as a major strategy to reduce CO_2 emissions to the atmosphere, and therefore to find an equilibrium in the natural carbon cycle. However, activating this stable small molecule is very challenging. In fact, high internal energy-containing reactive substrates can facilitate chemical transformations of CO_2 to compensate its thermodynamic stability. Moreover, efficient catalysts are needed to overcome the high kinetic barrier of activation. Among many catalytic methods, thermal catalysis is still the mostly used method to scale up the CO_2 fixation processes at industrial level. Catalysts with higher activity and selectivity in milder reaction conditions are required. Therefore, we aim to assess the efficiency of low-cost earth-abundant materials as catalysts for CO_2 cycloaddition with high energy-containing epoxides. We also aim to understand the behavior of these catalysts from computational mechanistic studies, and to improve on their design corroborating with their experimental catalytic performance for this CO_2 transformation reaction.

In this Thesis, we study three different catalysts for CO_2 cycloaddition reaction with epoxides under thermal gradient. The catalysts are lignocellulosic biomasses as most abundant plant materials, 1,10-phenathronine derived four nitrogen donor containing complexes of zinc, and a cyclam derived complex of the most abundant element iron. The cooperative effects of these binary catalysts in combination of a co-catalyst, tetrabutyl ammonium bromide (TBAB) are elucidated from

computational mechanistic studies. In experimental studies, the catalytic reactions are optimized for standard substrates, and %substrate conversions are corroborated with the activation energy barriers from reaction mechanisms, where applies. Also, the nature of different catalytic active sites is analyzed from substrate scope standpoint.

Chapter 1 agues the need of CO_2 utilization to be an integrated part of circular carbon economy. The chapter begins with a brief discussion on the origin of the disturbance in the natural carbon cycle, and consequent rise of CO_2 concentrations in the atmosphere. Therefore, recycling the CO_2 back into a circular carbon economy is shown as a solution. CO_2 utilization rather than CO_2 capture is shown as a circular carbon economy route. The chapter ends with a discussion on catalytic CO_2 transformations into useful chemicals.

Chapter 2 shows the general and specific objectives of this Thesis.

In Chapter 3, we explain the essential theoretical background for this Thesis. It gives a summary on the nature of the cooperative catalysts used in this study. Then, it recaps some relevant fundamental mechanistic aspects followed by the elementary steps of the mechanism of catalytic CO_2 activation with epoxides. We also summarize main aspects of Density Functional Theory, and the functionals used in this Thesis work. Different corrections and solvation models are also depicted. In a nutshell, this section argues the need of a suitable quantum chemical strategy including individual techniques and/or methods for specific computations.

In Chapter 4, we design the catalytic components of lignocellulosic materials as hydrogen bond donor catalysts. Molecular modelling of these

catalytic reactions found that the 1,2-diol of cellulose and 1,3-diol of lignin fragments activate epoxides by H-bonding. In other words, the -OH groups present in hollocellulose and lignin of lignocellulosic materials contribute to their activity as catalysts. The %substrate conversion by LiG/TBAB binary system was higher than that of CtS/TBAB system which was found in agreement with the lower cyclic carbonate ring-closing activation barrier of the former system.

Chapter 5 describes CO_2 cycloaddition with epoxides catalyzed by 1,10-phenathronine derived four nitrogen donor containing complexes of zinc (Zn-phen-N4R complexes, R = H/Et/iPr). The most stable conformer of Zn-phen-N4H and Zn-phen-N4iPr complexes were found from systematic conformational analyses. However, in case of Zn-phen-N4iPr, the conrotatory and disrotatory motions became almost indistinguishable. Moreover, during the mechanistic studies, the catalytic active site(s) had gone through structural changes that proves that the conformational analysis was useful only to predict the catalytic stability but not the catalytic activity.

Followed by experimental studies, the catalytic activity of Zn-phen-N4iPr/TBAB system was optimized at 80 ^{o}C, 10 bar and 3h with 0.13/0.2 mol% cat/co-cat ratio for the conversion of benchmark substrate, 1,2-epoxyhexane (EPH). At this optimal condition, the increments of %substrate conversion by the catalyst over the co-catalyst were similarly high for PO and EPH to 62% and 63%, respectively. Unfortunately, we could not recycle the catalyst, Zn-phen-N4iPr.

Then, from computational standpoint, we explored two different reaction paths, namely α-path and β-path, for the CO_2 cycloaddition with model substrate, PO. To our surprise, the α-path following a concerted mechanism was found to lower the cyclization barrier to a great extent. According to this path, changing the substituents in Zn-phen-N4R from R = iPr to R = H can lower the epoxide ring-opening step, possibly due to less steric hindrance. Finally, with the Zn-phen-N4iPr/TBAB system, changing the substrate from PO to SO, the activation energy of the ring-opening step lowers twofold, however, the cyclization barrier was still higher than the cyclization barrier for PO followed by α-path.

Chapter 6 presents an Fe (III)-cyclam complex in combination of a nucleophile, TBAB as an active catalytic system in CO_2 cycloaddition reaction with epoxides. The reaction was optimized for the benchmark substrate, 1,2-epoxyhexane. Among a series of substrates, the highest increment of 49% conversion over the co-catalyst TBAB was found in case of propylene oxide. The catalytic system Fe^{III}(c-cyclam-Me,Me)Cl_2]PF_6/TBAB was recycled and reused for the reaction of PO conversion into PC. Based on the types of the substrates, reaction mechanisms were proposed for the formation of cyclic carbonates and/or polycarbonates.

Chapter 7 recollects the general conclusions extracted from this Thesis.

Additional information of Chapter 4, 5 and 6 can be found in corresponding Appendix placed in the end of this report.

UNIVERSITAT ROVIRA I VIRGILI
CATALYTIC CO2 CYCLOADDITION WITH EPOXIDES INTO CYCLIC CARBONATES: SYNERGIES FROM COMPUTATIONAL TO EXPERIMENTAL STUDIES
Md Bin Yeamin

CHAPTER 1:

From Circular Carbon Economy to Carbon Dioxide Utilization: A General Introduction

1.1 Global Warming and Carbon Dioxide in Carbon Cycle

A wide range of social agents, from arctic environmental scientists[1] to teen social activists[2] are warning the recent devastating climate change indices. Governments of global villages are more and more interested in unifying their infrastructures to tackle and make the global economy resilient to the prone changes. Organizations aligned to the European Green Deal have started to discuss to figure out possible pathways to create a resilient economy and prosperous society.[3] All these emergency measures are originated from the single most important factor, the global warming.

The global warming is directly associated to the amount of CO_2 in the atmosphere. In the United States, the National Oceanic and Atmospheric Administration (NOAA)[4] records the level of atmospheric carbon dioxide. The recorded data in parts per million (ppm) can be seen in Figure 1 - 1. It shows a continuous increase in atmospheric CO_2 from 315 ppm to 413 ppm from 1958 to 2020, and yet higher to 415 ppm, as of January 2021.[5]

The global warming is well-understood from the creation of the CO_2 molecule at the beginning of the universe and its movement throughout the earth's carbon cycle. The planets which contain CO_2 are namely Earth, Mars, and Venus. In the beginning of the universe, the water vapors condensed in the Earth atmosphere which eventually made the conditions that create earliest aquatic organisms. These early lives then used energy from sun to photosynthesize water and carbon dioxide into organic compounds and oxygen. At that time, unlike today, the oxygen in the atmosphere increased while the carbon dioxide decreased.

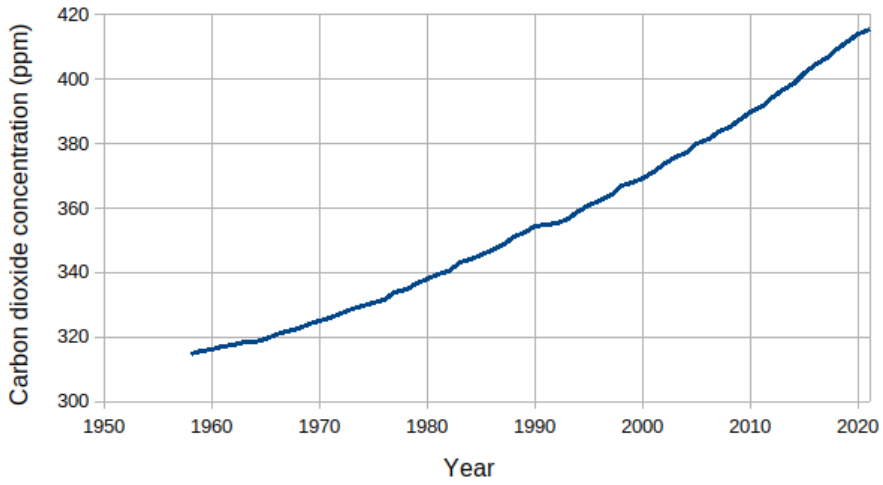

Figure 1 - 1. Atmospheric CO_2 in ppm from 1958 to 2021.[5]

Carbon is present in all forms of lives like in the geological formations, in the oceans as carbonate, also in the atmosphere as CO_2 gas. In the natural carbon cycle, carbon reforms among fossil, terrestrial, oceanic, and atmospheric reservoirs as shown in Figure 1 - 2. The distribution of CO_2 among these reservoirs is regulated by their

interactions with atmospheric gases over the lifetime of the earth. But, the human activities have been disturbing this equilibrium, and by now have added billons of tons of carbon to the cycle. Although the oceans and terrestrial biosphere absorb about half of the CO_2 produced annually from fossil fuel, the rest of CO_2 remains in the atmosphere.

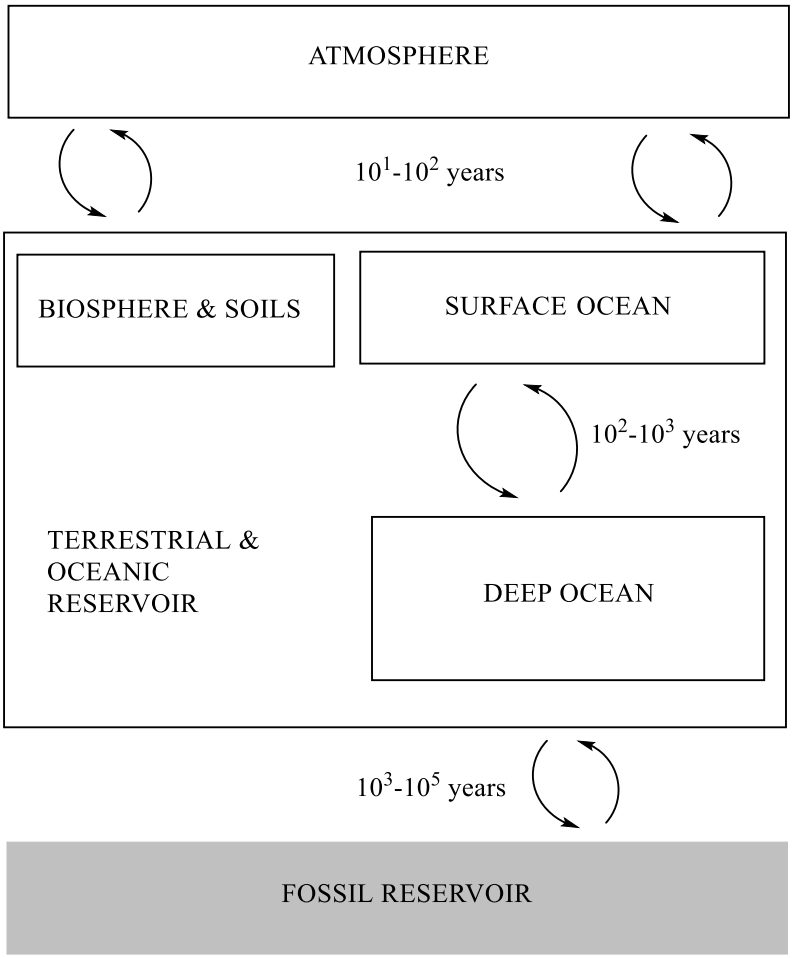

Figure 1 - 2. Natural carbon cycle: carbon pathways among fossil, terrestrial, oceanic, and atmospheric reservoirs. (Adapted from Ozin and Ghoussoub[6])

Sun exposes a combination of UV, visible and infrared light to the earth. In return, the radiation emitted by the earth is mostly of the infrared spectrum. Since CO_2 is an infrared-sensitive molecule, it absorbs the infrared radiation as heat and contributes most in the global warming.

The ability of molecules to absorb and emit radiation comes from the motions of atoms within molecules. The vibrational motions of CO_2 are shown in the Figure 1 - 3. In the symmetric stretching mode, Figure 1 - 3 (a), both the carbon-oxygen bonds are lengthening and shortening at the same time. This mode is infrared inactive. However, in the asymmetric mode, Figure 1 - 3 (b), one carbon-oxygen bond shortens while the other lengthens which is known to absorb the infrared radiation. Finally, both of the bending vibrations in Figure 1 - 3 (c) and Figure 1 - 3 (d) are infrared active.[7]

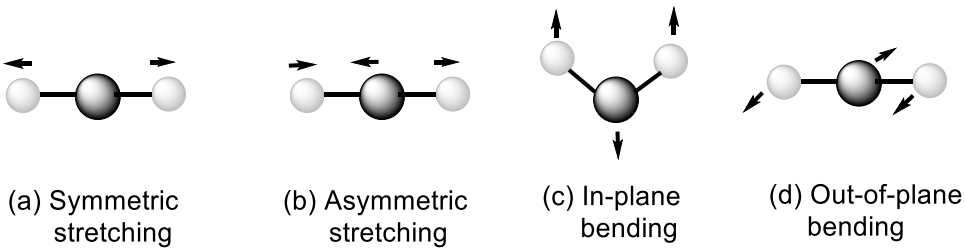

Figure 1 - 3. Different vibrations of CO_2 molecule.

1.2 CO_2 Recycling in Circular Carbon Economy

The industrial revolution allowed us to overcome the scarcity of food, shelter, and clothing by exploiting the opportunity of a linear industrial economy. In this linear process, as shown in the left side of Figure 1 - 4, the products are manufactured, packaged, distributed, consumed, and finally disposed. However, the final step, waste management, is not a liability of the manufacturer which is an overwhelming handicap of the linear industrial model.

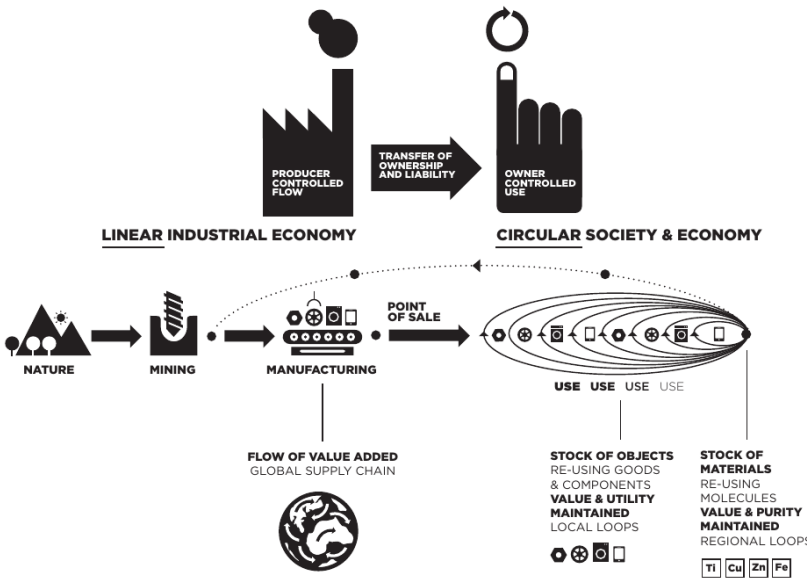

Figure 1 - 4. Features of linear industrial economy in comparison with circular society and economy. (Reused from Stahel[8] with permission)

Introducing a recycling loop to the process, the linear economy transforms to a circular one where at least a fraction of materials would be recovered and reused as shown in the right side of Figure 1 - 4. This model, in contrast to the linear industrial economy, maintains the value and utility, optimizes the stock management (not the flow) and thus increases the efficiency of goods instead of only producing goods. The circular industrial economy also recovers the atoms and molecules of the end-of-service-life objects. In a nutshell, a linear model can be converted into a circular one by transferring its ownership and liability. Eventually, in a matured circular model, the production must follow a sustainable approach.

Current supply chain of chemical industries makes about forty thousand chemicals from oil, gas, and biomass. On the contrary, in a circular CO_2 economy, these fossil resources are eliminated, and excess CO_2 will be converted into value-added products using CO_2-utilization technologies. Also, CO_2 conversion to liquid hydrocarbons could hold the key to decarbonizing the transport sector's stubborn emissions from large transport vehicles.[9]

Saudi Arabia has world's second-largest proven crude oil reserves. The oil company Saudi Aramco[10] has taken rigorous initiatives to an ecosystem of circular carbon economy. It follows the 4 Rs encompass: reduce, reuse, recycle, and remove CO_2. Followed by "Reduce" it builds efficient technology to mitigate the amount of carbon entering the atmosphere. Then, CO_2 capture belongs to "Reuse". The "Recycle" phase includes the chemical transformation of CO_2 into new products. Finally,

the "Remove" era of the encompass is to store the rest of the captured CO_2 underground.

1.3 CO_2 Storage and Utilization

Since power and heat production release large amount of CO_2 into the atmosphere, the industrial processes are adopting technologies to capture the CO_2 by-product from the processing of various raw materials and fuel combustion. The captured CO_2 then is transported and stored permanently underground. An integrated carbon capture infrastructure of Norwegian state enterprise, Gassnova SF, can be seen in Figure 1 - 5. From the intermediate storage, CO_2 can be transported by pipeline or in tanks to the suitable reservoirs where it mostly is converted into mineral carbonates. Geographically the North Sea has been identified as a suitable location both for underground and beneath the seabed CO_2 storage. Other Nordic industrial hubs like Rotterdam also share the same route for the final CO_2 storage.

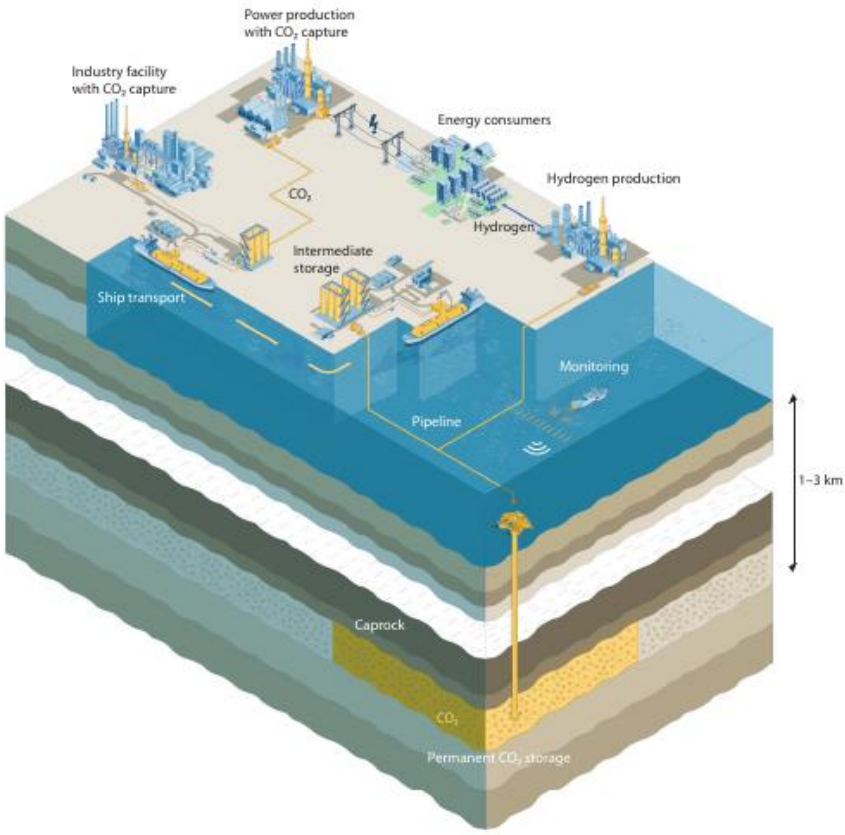

Figure 1 - 5. Gassnova's carbon capture from different industrial facilities and power station.[11] (Reused with permission)

In fact, industries and power stations use amine technologies to capture flue gas. The carbon capture process of Fortum Oslo Varme is shown in Figure 1 - 6.

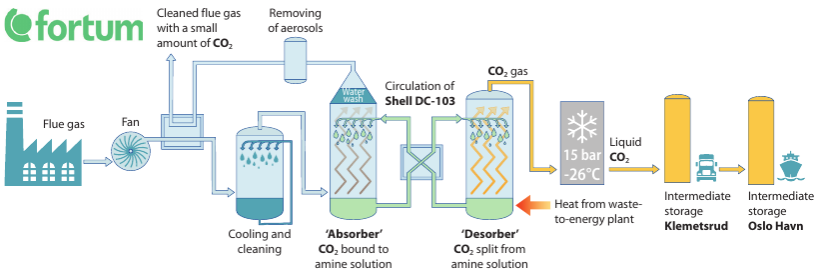

Figure 1 - 6. Fortum Oslo Varme's carbon capture process.[11] (Reused with permission)

After the capture, CO_2 can either be disposed (Carbon Capture and Sequestration, CCS) or can further be utilized (Carbon Capture and Utilization, CCU). CCS and CCU are two different approaches to solve the "CO_2-problem". According to the definition of section 1.2, the CCS corresponds to Linear Carbon Economy whereas CCU is a step forward to Circular Carbon Economy.[12]

Following the CCU approach, different catalytic and biotechnological methods are used to convert CO_2 into various chemicals and fuels as shown in Figure 1 - 7. The catalytic methods are named after the types of catalysis used and are classified by the energy source consumed in the transformation process i.e., heat, light, or electricity. Some types of catalysis take their energy from two sources rather than a single source. For instance, photothermal chemistry-based catalysis takes energy both from light and heat while the catalysis based on photoelectrochemical chemistry are driven by both light and electricity.

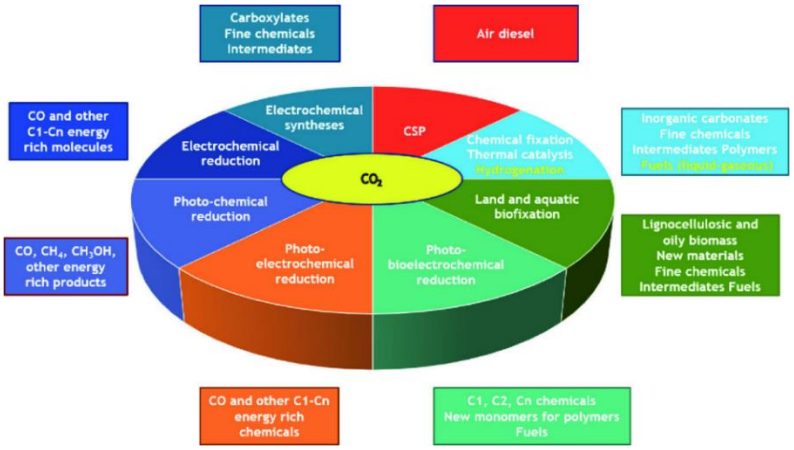

Figure 1 - 7. Different CCU technologies and their end products. CSP stands for Concentrators of Solar Power. The blue routes are to chemicals. All others require water.[12] (Reused with permission)

1.4 Catalytic CO_2 Transformations

The combination of CCS and CCU approaches (CCUS) is getting more and more enforcements worldwide. The European Carbon Dioxide Capture and Storage Laboratory Infrastructure (ECCSEL)[13] keeps increasing the list of new CO_2 utilization facilities under the consortium. Most recently, Accelerating CCS Technologies (ACT)[14] has brought an international initiative to establish CCUS as a tool to combat global warming.

However, in research and innovation, the chemical applications of CO_2 are far more mature. The potential uses of CO_2 in chemical syntheses can be categorized into three broad varieties as can be seen in Scheme 1 - 1. The direct incorporation of the entire CO_2 molecule leads to

carboxylates, carbonates, and carbamates. The products from this route (left) will have a low energy content and may occur at low temperature. On the contrary, the complete reduction of CO_2 (synthesis route on the right) to C_1 (e.g., methane) and C_n molecules (e.g., saturated hydrocarbons) require an input of energy. Such energy input could not come from fossil fuels but might be a solar energy. A third synthetic route (central part of the scheme) is a combination of reduction and bond formation to have a large set of functional molecules. Carbon is partially reduced by the removal of one oxygen atom. Chemical syntheses of this category involve CO_2 reduction using "renewable hydrogen" as a reducing partner which might come from e.g., (photo)electrolysis of water.

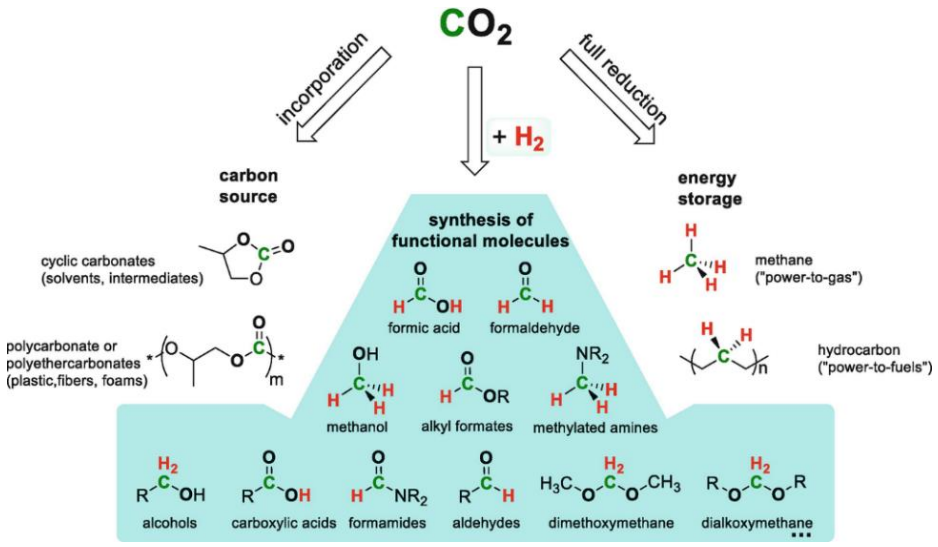

Scheme 1 - 1. Three basic catalytic CO_2 transformation pathways toward the synthesis of value-added products.[15] (Reused with permission)

1.5 CO_2 as a Chemical Feedstock for the Synthesis of Organic Carbonates

Chemical synthesis followed by direct incorporation of the entire CO_2 molecule to organic carbonates might end up to linear or cyclic carbonates, as shown in Scheme 1 - 2. Since CO_2 is a highly stable molecule, these transformations require a catalyst. Organic carbonates mostly are used as reagents, solvents, and monomers for polymers.[16,17] Dimethyl carbonate (DMC) is the mostly used linear carbonate for the synthesis of polycarbonates. DMC is low toxic with no irritating or mutagenic effects and meets the green chemistry principles. Among the cyclic carbonates, ethylene carbonate (EC) and propylene carbonate (PC) are commercially used as reactive intermediates and inert solvents. Industries widely use cyclic carbonates as polar solvents, and as precursors for polycarbonate materials synthesis. They are also used as electrolytes in lithium secondary batteries, in pharmaceutical production, and as raw materials of chemical reactions.

Linear carbonates, Scheme 1 - 2(a), can be found from direct carboxylation of alcohols whereas cyclic carbonates, Scheme 1 - 2(b), are mainly synthesized from the direct carboxylation of epoxides and from the carboxylation of di(poly)ols. Moreover, epoxides are made from oxidation of alkenes using the oxidants O_2, H_2O_2 etc. The complete path is shown in Scheme 1 - 3. Nevertheless, the market of epoxides is much lower than that of carbonates, and epoxides are costly. Therefore, an alternative is a one-step oxidative carboxylation of olefins. Although this

one-pot synthesis would avoid the intermediate synthesis of epoxides, such strategy typically competes with a parallel process of two-oxygen addition to the olefin double bond which results in low yield carbonates. Moreover, the produced complex reaction mixture requires energy for separation.[18]

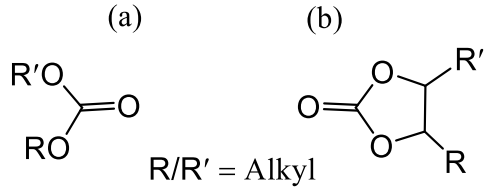

Scheme 1 - 2. (a) Linear and (b) cyclic carbonate.

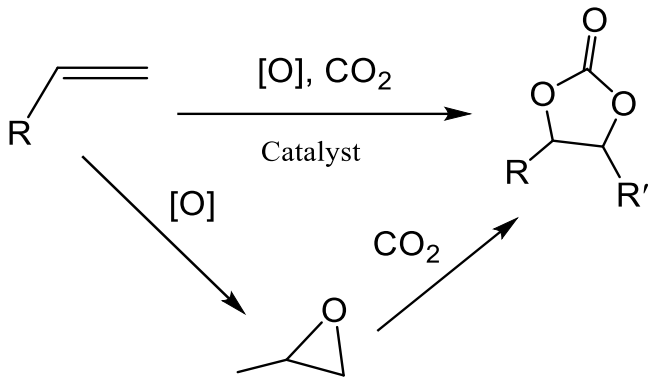

Scheme 1 - 3. Different routes for synthesis of cyclic carbonate starting from alkenes.

A wide variety of other synthetic approaches for the cyclic carbonates is seen in Scheme 1 - 4. In the beginning, highly toxic phosgene and ethylene glycol were reported to produce ethylene carbonates. Today,

various other C_1 building blocks such as linear dimethyl carbonate, urea, CO, and CO_2 are used with diols to produce cyclic carbonates. Also, halohydrins, propargyl alcohols, and even alkenes are used as starting materials.[18]

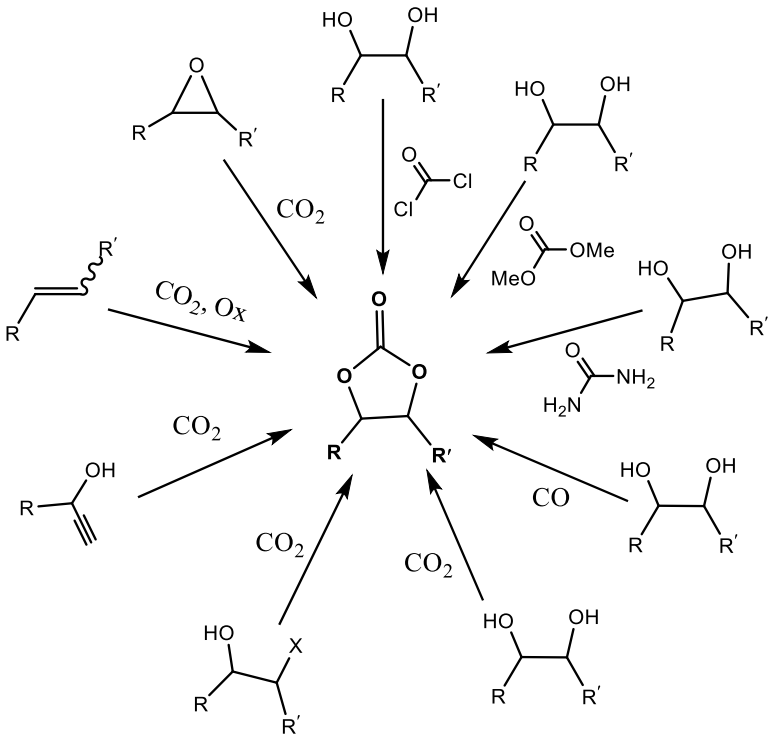

Scheme 1 - 4. Synthetic routes for the formation of cyclic carbonates.[18] (Reproduced with permission)

Catalytic CO_2 cycloaddition reaction to epoxides is already brought from laboratory to industry for the synthesis of cyclic carbonates and/or polycarbonates.[17] This reaction might produce cyclic carbonate or polycarbonates or a mixture of both as shown in Scheme 1 - 5. The

chemoselectivity of this reaction depends on many factors associated with the nature of catalysts and epoxides, and the reaction conditions.[19]

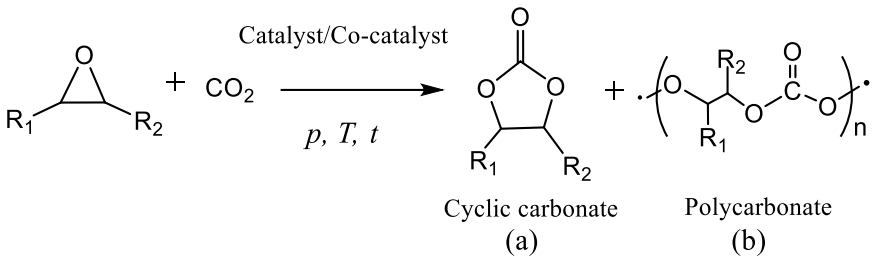

Scheme 1 - 5. Possible products of the reaction of CO_2 with epoxides: (a) cyclic carbonate, (b) polycarbonate.

Uncatalyzed CO_2 fixation with epoxides gives low yield of cyclic carbonates. This low yield is associated with the high activation energy in the rate-determining step of the reaction.[20] Without any catalyst, the activation free energy is as high as 58.92 kcal mol^{-1} but it drops to 28.20 kcal mol^{-1} when the reaction is catalyzed by one of the mostly used catalysts, tetrabutylammonium bromide (TBAB). A binary catalytic system, TBAB/H_2O, further lowers the activation energy to 20.68 kcal mol^{-1}.

CO_2 cycloaddition with epoxides into cyclic carbonates has extensively been studied with a variety of catalysts including metal oxides, alkali metal salts, ionic liquids, transition metal complexes, functional organic compounds, and polymers. However, rational design of highly effective catalysts is still desirable. This thesis studies catalytic CO_2 cycloaddition with epoxides into cyclic carbonates to look for best reaction conditions and try to elucidate the reaction mechanism in detail.

1.6 References

(1) Study of Environmental Arctic Change (SEARCH) https://www.searcharcticscience.org/node/27076 (accessed 2021 -01 -04).
(2) Ernman (mother), M.; Award (2019), F. O.; Prize (2019), R. C.; Award (2019), A. of C.; Award (2019), R. L.; Prize (2019), I. C. P.; Year (2019), T. P. of the; Prize (declined) (2019)[3, N. C. E.; Humanity (2020), G. P. for. Greta Thunberg - Wikipedia https://en.wikipedia.org/wiki/Greta_Thunberg (accessed 2021 -01 -04).
(3) European Green Deal: delivering ambitions through a System Change Compass //events.euractiv.com/event/info/european-green-deal-delivering-ambitions-through-a-system-change-compass (accessed 2021 -01 -04).
(4) National Oceanic and Atmospheric Administration https://www.noaa.gov/ (accessed 2021 -01 -04).
(5) Keeling, R. F.; Keeling, C. D. Atmospheric Monthly in situ CO_2 Data - Mauna Loa Observatory, Hawaii. In *Scripps CO_2 Program Data;* UC San Diego Library Digital Collections. (accessed, 14 April 2021)
(6) Ozin, G. A.; Ghoussoub, M. F. *The Story of CO_2 : Big Ideas for a Small Molecule*; University of Toronto Press: 2020; p 53.
(7) Ozin, G. A.; Ghoussoub, M. F. *The Story of CO_2 : Big Ideas for a Small Molecule*; University of Toronto Press, 2020; p 82.
(8) Stahel, W. R. *The Circular Economy: A User's Guide*; Routledge: New York, 2019; pp 16–17.
(9) Ozin, G. A.; Ghoussoub, M. F. *The Story of CO_2 : Big Ideas for a Small Molecule*; University of Toronto Press, 2020; p 129.
(10) The circular carbon economy https://www.aramco.com/en/making-a-difference/planet/the-circular-carbon-economy (accessed 2020 -12 -12).
(11) Energy, M. of P. and. Meld. St. 33 (2019–2020) https://www.regjeringen.no/en/dokumenter/meld.-st.-33-20192020/id2765361/ (accessed 2020 -12 -17).
(12) Aresta, M. Perspective Look on CCU Large-Scale Exploitation. In *An Economy Based on Carbon Dioxide and Water: Potential of Large Scale Carbon Dioxide Utilization*; Springer International Publishing: Cham, 2019; pp 431–436.
(13) ECCSEL https://www.eccsel.org/facilities/utilisation/ (accessed 2021 -01 -08).
(14) About us — ACT http://www.act-ccs.eu/about-us (accessed 2021 -01 -08).
(15) Beydoun, K.; Klankermayer, J. *Organomet. Green Catal.* **2018**, 39–76.
(16) Dibenedetto, A.; Angelini, A. Synthesis of Organic Carbonates. In *Adv. Inorg. Chem.* **2014**, *66*, 25–81.
(17) Dabral, S.; Schaub, T. *Adv. Synth. Catal.* **2019**, *361* (2), 223–246.
(18) Büttner, H.; Longwitz, L.; Steinbauer, J.; Wulf, C.; Werner, T. Recent Developments in the Synthesis of Cyclic Carbonates from Epoxides and CO2. In *Chemical Transformations of Carbon Dioxide*; Springer International Publishing: Cham, 2018; pp 89–144.
(19) Pescarmona, P. P.; Taherimehr, M. *Catal Sci Technol* **2012**, *2* (11), 2169–2187.
(20) Wang, J.-Q.; Sun, J.; Cheng, W.-G.; Dong, K.; Zhang, X.-P.; Zhang, S.-J. *Phys. Chem. Chem. Phys.* **2012**, *14* (31), 11021–11026.

CHAPTER 2:

Objectives of the Thesis

2.1 Objectives

The general objective of this thesis is to produce cyclic carbonates using a green sustainable approach. To do so, we focused in three points: to use low-cost earth-abundant materials as catalysts for CO_2 cycloaddition with epoxides, to understand the behavior of these catalysts by means of computational mechanistic studies, and to improve their design with the help of the information obtained from the experimental analysis of the performance of the catalysts in different reaction conditions.

Lignocellulosic biomasses as most abundant plant materials, and coordination compounds with low toxic and abundant elements zinc and iron were three class of target catalysts. Due to facile nitrogen donor ligand preparation, four nitrogen containing 1,10-phenathronine derived complexes of zinc (Zn-phen-N4R complexes where R = H/Et/iPr; Figure 2 - 1 (a)), and a cyclam derived complex (Figure 2 - 1 (b)) of the most abundant element iron were used in this study. Also, cooperative effects of these catalysts in combination of a co-catalyst, tetrabutyl ammonium bromide (TBAB) are envisioned to unfold.

The specific aims of each catalytic system are as follows:

1. In a previous study from our research group, vegetal wastes were found to be active catalysts in combination of the co-catalyst, TBAB. In this study, we aim to elucidate the reaction mechanisms of their catalytic reaction for CO_2 cycloaddition to a model substrate, propylene oxide (PO). To develop this study, we will use a model of the cellulose and lignin part of lignocellulose as catalysts. The predictions derived from the activation energy barriers obtained in the mechanistic studies will be compared with the corresponding experimental observations.
2. A series of Zn-phen-N4R complexes were synthesized in a previous work of the group.[1] In this thesis, we aim to optimize the catalytic activity of the synthesized Zn-phen-N4iPr catalyst (Figure 2 - 1 (a)) in combination of TBAB for the conversion of benchmark substrate, 1,2-epoxyhexane (EPH), and to study the scope of the catalyst for various substrates conversions into cyclic carbonates. Then, from a computational standpoint, we aim to elucidate the reaction mechanisms of CO_2 cycloaddition to epoxides catalyzed by these cooperative binary Zn-phen-N4R/TBAB systems. The mechanistic study also plans to verify any possible stereoelectronic effect on catalytic stability due to the change in the R substituents of the aryl moiety of the catalyst structure. Moreover, the effect of

substrate types on reaction paths and therefore on the mechanism is also aimed to be checked.

3. An Fe(III)-cyclam complex (Figure 2 - 1 (b)) was prepared in the research group of Prof. Ruffo from the University of Naples Federico II, Italy. We aim to check the catalytic performance for CO_2 cycloaddition to epoxides in addition to the co-catalyst TBAB. The reaction is aimed to be optimized for the benchmark substrate, EPH, and then to extend for catalytic conversion of other substrates.

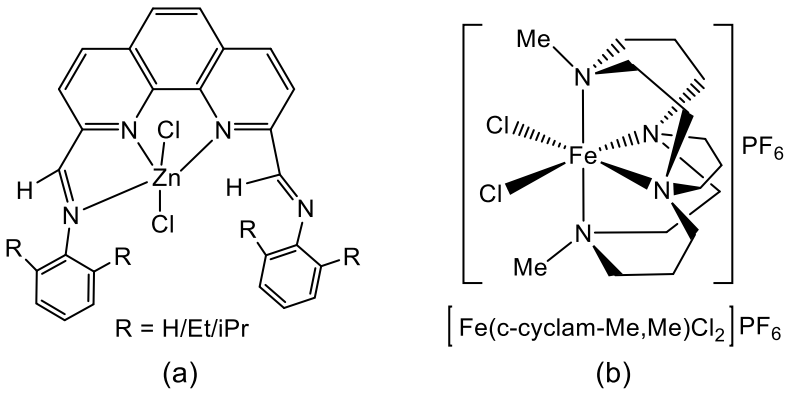

Figure 2 - 1. Four nitrogen containing (a) Zn-Phen-N4R complexes, and (b) Fe(III)-cyclam derived $[Fe^{III}(c\text{-}cyclam\text{-}Me,Me)Cl_2]PF_6$ complex.

2.2 References

(1) López-Redondo, C. *Zn Complexes with N4-donor Ligands for CO_2 Cycloaddition*. Bachelor's Thesis, 2015.

CHAPTER 3:

Chemical and Quantum Chemical Principles of CO_2 Cycloaddition with Epoxides into Cyclic Carbonates

This chapter presents the essential theoretical background involved in this work. Section 3.1 gives a summary on the nature of the cooperative catalysts used in this study. Then, section 3.2 introduces the mechanisms of catalytic CO_2 activation with epoxides. Section 3.3 recaps some relevant fundamental mechanistic aspects. Finally, section 3.4 argues the need of a suitable quantum chemical strategy including the individual techniques and/or methods for specific experiments.

3.1 A Brief on Cooperative Catalysis

Ligands are organic molecules or molecules of main-group elements or ions that bind to metal centers to make coordination complexes. These bonding interactions between metal and ligands modulate the electronic properties of the metal and determine the steric environment of coordination sphere, so thereby ligands control over the structure and reactivity of metal complexes. An understanding of ligands' influence on structural and reactivity properties of metal species driven

by creative design of ligand motifs allows the discovery of new and improved metal-catalyzed reactions.[1] This design architecture of catalysts is exploited in a wide variety of syntheses, from pharmaceuticals to polymers. Following such approach, chemists can isolate and examine reactive intermediates of relevant importance. One could uncover new modes of bonding between metals and organic or main-group compounds which would alter the chemical reactivity and catalytic activity of a newly synthesized metal complex.

Synthetic strategies of catalytic reactions can be divided in three categories[2] based on the modes of catalysis and role of the involved nucleophiles (represented by $Nu:^-$, $Nu^{\ominus}$ or Nu^-) and electrophiles (represented by E) as shown in Scheme 3 - 1. In bifunctional catalysis both nucleophile and electrophile are activated separately by individual functional groups of the same catalyst (Scheme 3 - 1 (a)). When two catalysts work in a concerted way to activate only one of the reacting partners, it is called double activation catalysis (Scheme 3 - 1 (b)). However, when the nucleophile and the electrophile are simultaneously activated by two separate catalysts, the strategy is termed synergistic or cooperative catalysis (Scheme 3 - 1 (c)). Simultaneous activation of nucleophiles and electrophiles by synergistic use of Lewis acid (LA) and Lewis base (LB) is an attractive way of enhancing chemical reactivity.[3] As it will be discussed later, this is the case of the binary catalytic systems studied in this thesis.

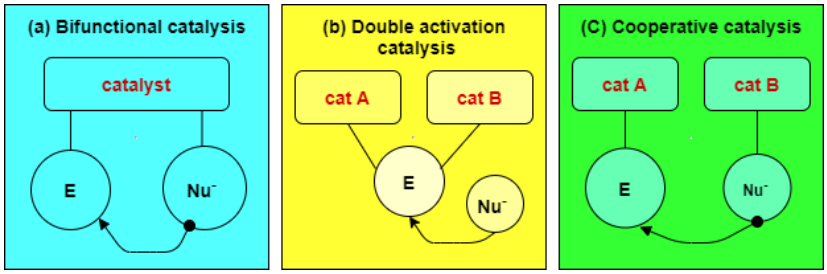

Scheme 3 - 1. Different modes of catalysis.

Lewis acids act as catalysts to activate electrophiles. A Lewis acid coordinates to a lone pair of electrons thus withdraws electron density and thereby activates an electrophile. The changes in the frontier orbital energies of the reactants are identified as the key effect of Lewis acids and Lewis bases on the reactivity of a given system. Following this phenomenon, the LUMO (lowest unoccupied molecular orbital) energy of an electrophile lowers whereas the HOMO (highest occupied molecular orbital) energy of a nucleophile increases. Simultaneous activation brings the LUMO of the electrophile and the HOMO of the nucleophile close in energy resulting in a further increase of reactivity of the system as shown in Scheme 3 - 2. Such dual activation can be reached using a bifunctional catalyst containing a LA/LB pair or by using two separate catalysts that act following the cooperative catalytic approach shown in Scheme 3 - 1.

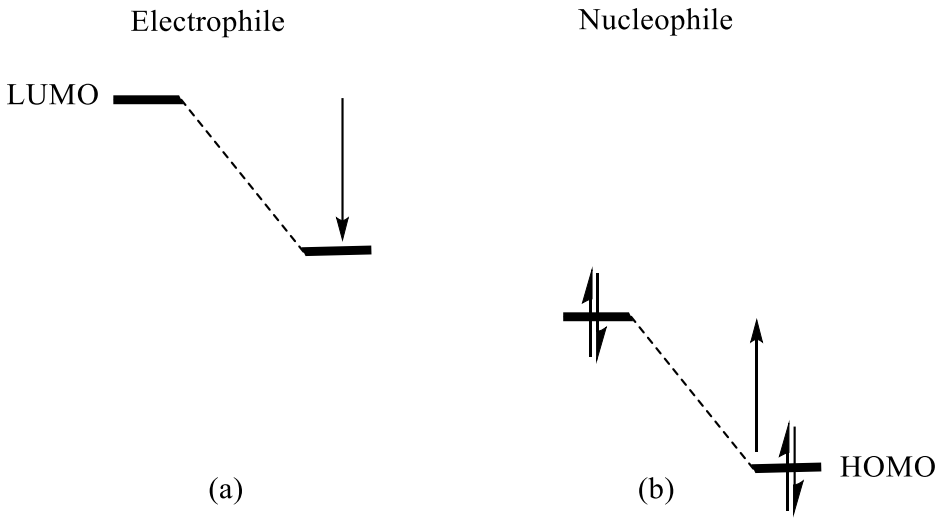

Scheme 3 - 2. (a) Electrophilic and (b) nucleophilic activation.

The general overview of cooperative catalysis is schematically shown in Scheme 3 - 3. The left panel shows how a traditional catalyst makes more favorable the catalytic reactions in comparison with an uncatalyzed reaction by lowering the HOMO-LUMO energy gap (ΔE). However, the right panel of Scheme 3 - 3 shows how cooperative catalysis involves the concurrent activation of both a nucleophile and an electrophile. This approach simultaneously creates two reactive species, one with higher HOMO energy and other with a lower LUMO energy than the non-activated system and thus provides further lowering of the HOMO-LUMO gap in comparison with the respective ground state starting materials. These activated species can quickly couple; otherwise, the chemical reaction would be difficult using the traditional mono-catalysis methods.

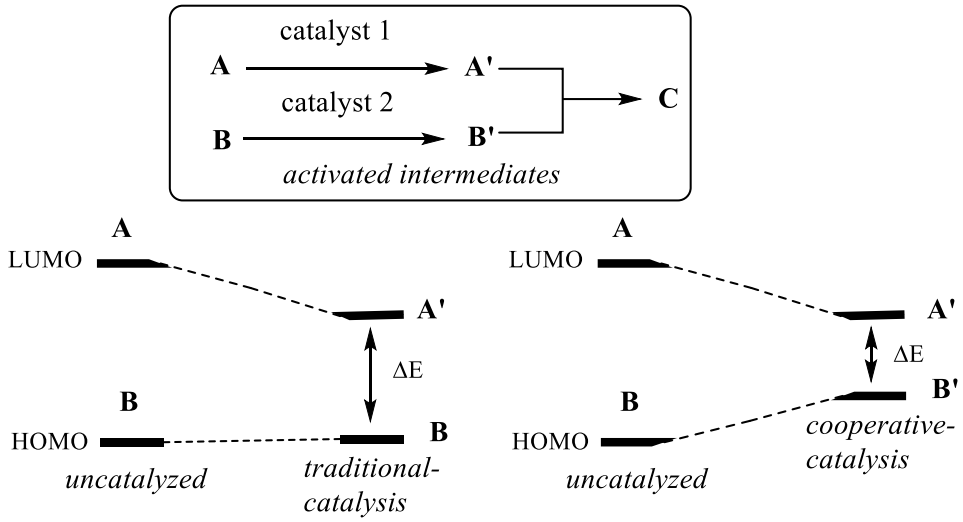

Scheme 3 - 3. Illustration of the concept of cooperative catalysis (right) v.s. traditional catalysis (left).[2]

3.2 Catalytic CO_2 Activation with Epoxides

CO_2 is a non-polar stable molecule with a π system formed by four electrons delocalized over three centers. Thus, to activate CO_2, high-energy substrates e.g., organometallic reagents and 3-membered ring compounds are used in CO_2 transformations. Also, high-energy additives (nucleophiles) might be added to trigger the reaction and to provide energy for a catalytic cycle. Moreover, application of catalysts could accelerate the transformation by lowering the energy barrier of transition states (TSs) which is the key to achieve thermodynamically favored reactions.[4]

According to Wang et. al.[4], CO_2-incorporated cyclization could be categorized in three different modes as shown in Scheme 3 - 4. In Mode I, a prior nucleophilic attack on CO_2 leads to an intramolecular cyclization to yield carboxylative cycles. In the case when a good leaving group (LG) is present in the molecule, it is eliminated (Scheme 3 - 4 b). This mode is the one corresponding to the cycloaddition of CO_2 with epoxides into cyclic carbonates which will be discussed latter. Alternatively, a sequential nucleophilic attack on CO_2 with substrates containing two nucleophilic sites gives cyclic carbonyl derivatives as depicted in Mode II. A third possible way, Mode III, shows nucleophilic attack on the reduced CO_2 followed by cyclization generating cyclic derivatives. The substrate in Mode I provides an electrophilic site to accept excess electrons from oxygen while Mode II offers nucleophilic sites to attack CO_2 giving place stable heterocycles.

However, in Mode III, depending on the electron acceptor properties of the central carbon, the valence of central carbon of CO_2 changes, and it may act as flexible one-electron synthetic building block (synthon) e.g., “CH”, “CO” or “CH_2” to construct heterocycles. Being an electrophile, CO_2 could easily be trapped by various strong nucleophiles to form C-N, C-O or C-C bonds with some negative charge shifted to the O atom of CO_2. Resulting nucleophilic oxygen anions drive many substrates to undertake tandem cyclizations assisted by a catalyst or a base to produce various valuable chemicals such as 2-oxazolidinones, cyclic carbonates, and lactones.

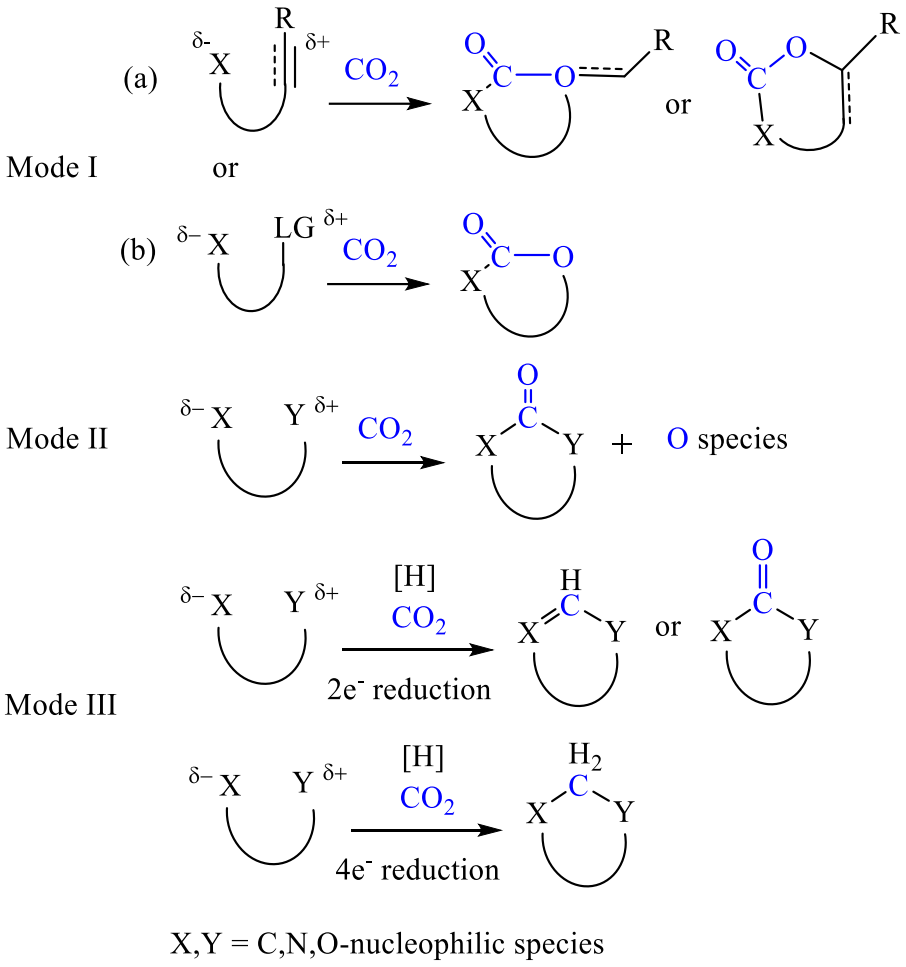

Scheme 3 - 4. Reaction modes of nucleophile-driven CO_2-incorporated annulation. LG stands for leaving group. (Adapted from Wang and Xi[4])

Epoxides are high-energy reactive substrates due to the presence of a heteroatom and high strain energy of three-membered ring (~28.44 kcal mol^{-1}). The elementary reaction steps involved to the cyclic carbonate synthesis from epoxides and CO_2 are sketched in Scheme 3 - 5.[5] Basically,

it is a three-step mechanism: (I) epoxide ring opening, (II) CO_2 insertion, and (III) intramolecular cyclization (ring-closing).

The epoxide activation requires a transition metal as Lewis acid or hydrogen bond donor (HBD) groups e.g., -OH, -COOH, -NH- and a nucleophile opens the epoxide ring, together they act as cooperative catalysts (Scheme 3 - 1 (c)). The acidic metal center of Lewis acids coordinates to oxygen of epoxides, and thus can activate the C-O bond of the epoxide to facilitate the ring-opening. In this work, zinc and iron complexes have been used as catalyst (Chapter 4 and 6). HBD groups binds to the oxygen atom of epoxide through formation of hydrogen bonds and polarizes its C-O-ring bond.[5] Lignocellulosic materials as HBD have been used in Chapter 4. Both events produce two electrophilic carbons in the epoxide. Eventually, a nucleophile might attack at less substituted carbon, C_b or at more substituted carbon, C_a, followed by a S_N2 mechanism. But the best target for the nucleophile in an S_N2 reaction is the carbon that is least hindered. In most of the cases, the activation and ring-opening of epoxides are found as the rate-determining step in the cycloaddition of CO_2 to epoxides. Halides of ammonium salts are commonly used nucleophiles.

Comparing with Scheme 3 - 1 (c), the Lewis acid catalysts of Chapter 5 and 6, and HBD catalysts used in Chapter 4 are of type cat A catalysts. Epoxides are the electrophiles. The co-catalyst, TBAB is of type cat B which delivers the nucleophile, bromide ion.

In step (II), the CO_2 insertion reaction, the readily made open oxyanion intermediate is stabilized by metal ion or HBD group which

facilitates CO_2 insertion leading to the formation of alkyl carbonate intermediate. The insertion occurs through a CO_2^- adduct with the electron-rich alkoxide species that breaks the linearity of CO_2. In fact, the gradual change of the C atom hybridization from sp to sp^2 makes CO_2 a C-electrophile leading to its insertion.

In step (III), the alkyl carbonate intermediate finally undergoes an intramolecular ring-closing with a simultaneous release of nucleophile, producing the cyclic carbonate through a S_N2 mechanism. Finally, step (II) and (III) together consists of 1,3 dipolar cycloaddition mechanism[6], also known as (3+2) cycloaddition, is the most universal synthetic approach to five-membered heterocycles formation.[7] Similar Lewis acid catalyzed (3+2) cycloadditions are reported for the generation of five-membered ring systems from cyclopropanes.[8]

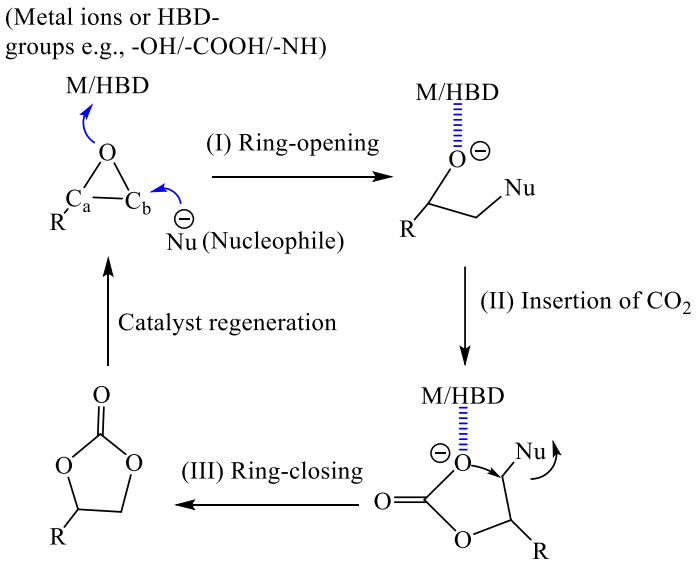

Scheme 3 - 5. Elementary reaction steps for the cycloaddition of CO_2 to an epoxide. (Adapted from Liu et al.[5])

The regio- and stereo- selectivity of CO_2 coupling with epoxides depend on the epoxide structure. The mono-substituted terminal epoxides are more reactive than the internal epoxides.[9] Scheme 3 - 6 shows the regioselectivity of ring-opening of mono-substituted terminal epoxides for LA-catalyzed CO_2 cycloaddition with epoxides. In case of 1,2-disubstituted (internal) epoxides, if two consecutive S_N2 reactions proceed through a S_N2 mechanism, final carbonate will retain the configuration of the carbon atoms. For the terminal epoxides, the final configuration of cyclic carbonate will be the same regardless the regioselectivity of the nucleophilic attack. The right panel of the scheme shows the mechanism followed by an epoxide ring-opening from the nucleophilic attack at the less substituted C_b whereas the left panel reveals the ring-opening by the nucleophile attach at the more substituted C_a.

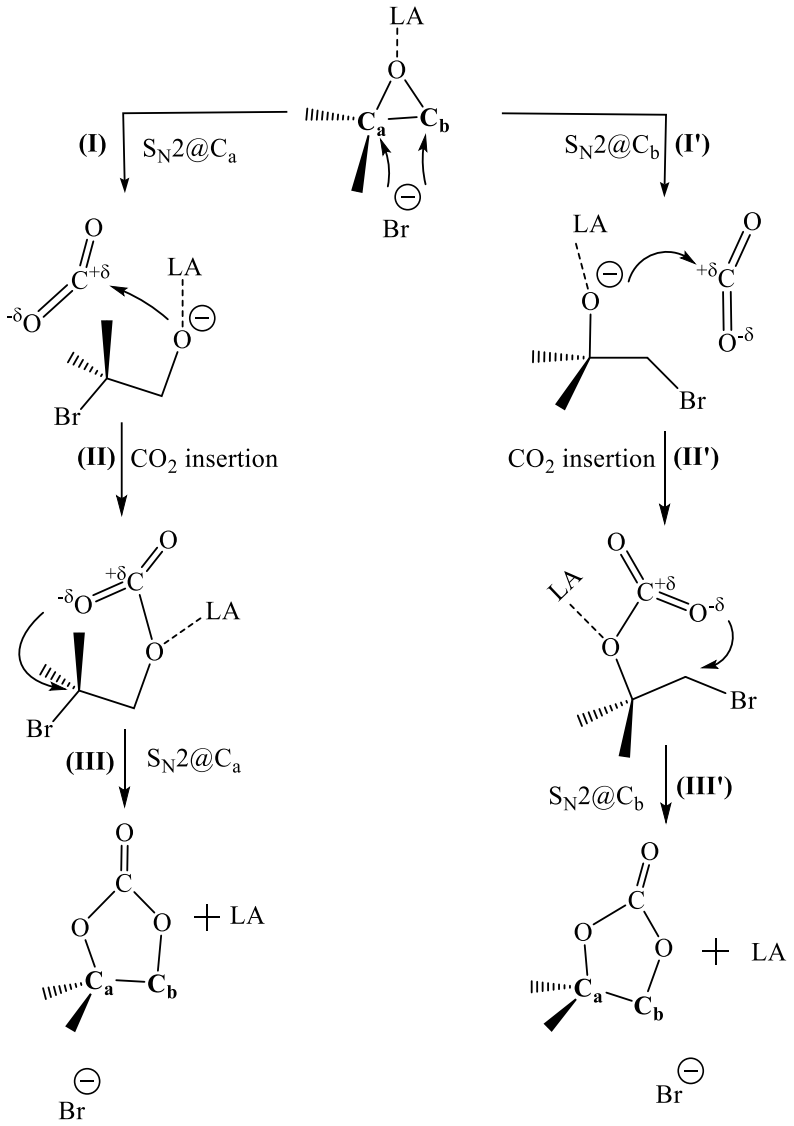

Scheme 3 - 6. LA-catalyzed CO_2 cycloaddition with epoxides: (**I/I'**) ring-opening of epoxides, (**II/II'**) CO_2 insertion in the alkoxide, and (**III/III'**) ring-closure. Steps (**II/II'**) and (**III/III'**) constitute the 1,3 dipolar cycloaddition mechanisms.

3.3 On Some Mechanistic Aspects

3.3.1 Energetics of Catalytic Reactions

In general, a mechanism is an account of all structural changes that occur as a reactant is transformed into a product. To rationalize experimental observations and to develop new synthetic methodologies, the determination of reaction pathways of organic reactions is essential. Only from experiments, the full characterization of a mechanism is extremely difficult. Computational studies deliver information that are complementary to the experiments and become fundamental to elucidate the detailed reaction mechanisms.

Many chemical reactions do not occur merely in a single step but rather may have several elementary steps with one or more intermediate and transition state structures (activated complex) as shown in Figure 3 - 1. The overall sequence of steps is termed a mechanism which is usually represented by a reaction coordinate diagram.[10] Mechanisms may be established from computations by elucidating all possible sequences from reactants to products and then identifying that particular sequence with the lowest-energy rate-limiting TS. When the (potential) energy of a molecule/cluster is represented against its geometric parameters, the multidimensional surface obtained is called potential energy surface (PES). A simplified representation of the PES in front of a generic

geometrical coordinate provides an energy profile like the one shown in Figure 3 - 1.

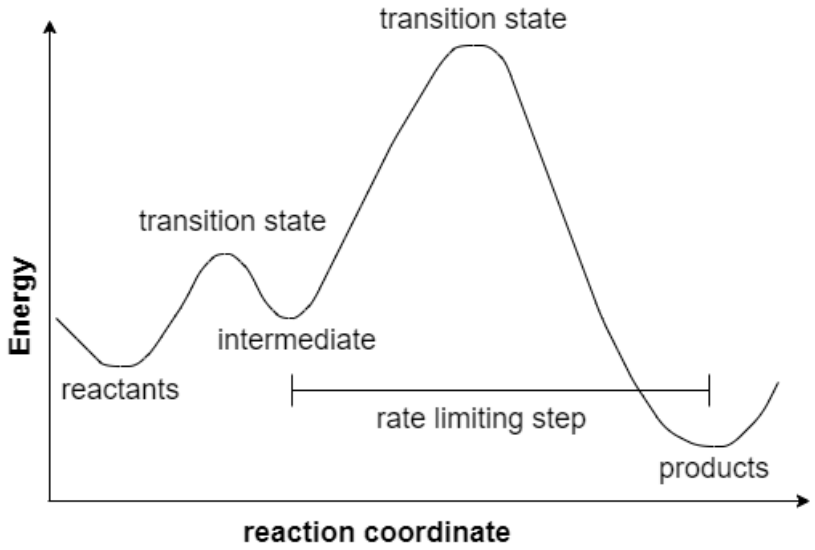

Figure 3 - 1. Example of an energy profile of a PES along the reaction coordinate with the basic components of a reaction mechanism.[10]

When a catalyst interacts with one or more species of a reaction, in most cases, the reaction is catalyzed by changing its mechanism. Any elementary reaction can be accelerated by decreasing the activation free energy $\Delta^{\ddagger}G$ or can be retarded by increasing the activation free energy $\Delta^{\ddagger}G$ if the reactants and/or the transition structures make complexes or adducts with spectator molecules such as solvent, additive, catalyst, inhibitor and a combination of them. This is represented in Figure 3 - 2. Figure 3 - 2(a) shows the profile of the free energy for a bimolecular reaction involving reactants A and B on their own. A catalyst C, Figure 3 - 2(b), stabilizes the transition structure more than that of the uncatalyzed

gas phase reaction, i.e., $\Delta^{\ddagger}G(B) < \Delta^{\ddagger}G(A)$. On the contrary, an inhibitor D, Figure 3 - 2(c), destabilizes the transition structure relative to the uncatalyzed gas phase reaction, i.e., $\Delta^{\ddagger}G(C) > \Delta^{\ddagger}G(A)$.

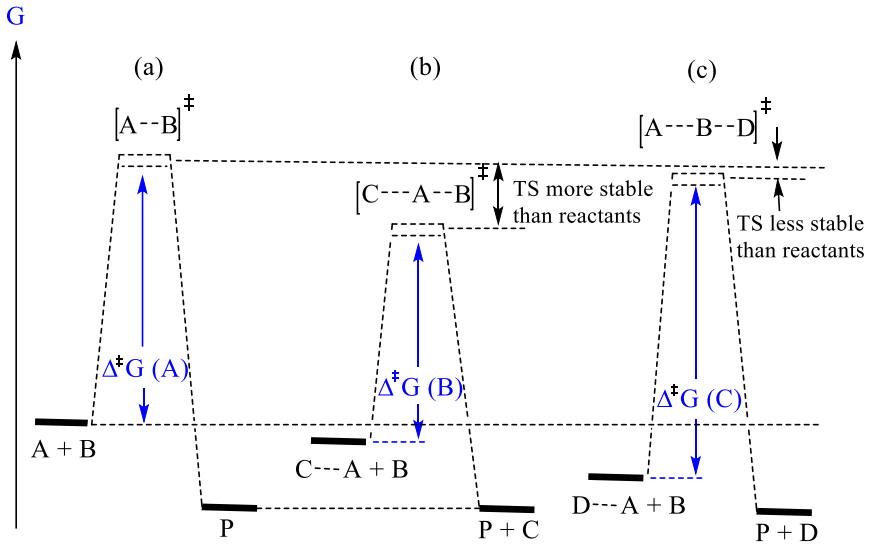

Figure 3 - 2. Free energy diagram of (a) uncatalyzed gas-phase bimolecular reaction A + B → P, (b) catalyzed (catalyst C) bimolecular reaction, and (c) bimolecular reaction inhibited by additive D.[11]

3.3.2 Some Factors associated with Chemical Reactivity

The molecular geometry and its chemical reactivity are highly influenced by the conformation. Identifying important conformers is crucial. The equilibrium ("thermodynamic") abundance of conformers depends on their relative energies. According to Boltzmann distribution,

the lowest-energy conformer (global minimum) appears in the greatest amount whereas the second lowest-energy conformer is the next greatest amount and so on. Some higher conformers become in rapid equilibrium with the global minimum are called "reactive conformers". Any barriers which separate these conformers are much smaller than the reaction barrier and will be replenished throughout the reaction.[12]

Stereoelectronic effect is often wrongly thought as a combined steric and electronic effect. Rather, it is strongly associated with conformations. In fact, stereoelectronic effects are the stabilizing interactions coming from increased delocalization in a favorable conformation. Herein, a particular geometric arrangement in a favorable orbital overlap maximizes the stabilizing electronic interactions.[13]

Stereoelectronic effect may affect at any stage of a reaction and thus modify PES in different ways. It is known that TS stabilization is the most direct way to lower the activation barrier. As can be seen in Figure 3 - 3, the preferential stabilization for a particular TS is not determined by the relative energies of ground state conformers. Rather, according to the Curtin-Hammett principle, the relative TS energies determine the nature and the ratio of the products, as long as the reactive conformers (Scheme 3 - 4) can quickly equilibrate. Therefore, as shown in Figure 3 - 3(a), even though R_A is the more stable conformer in the ground state, the TS_B might be the more stable TS. It means the stereoelectronic stabilization of A would be unproductive if the TS_B is the rate- and product-determining TS.[14] When such stabilization fails during the conversion of A to B and then to TS_B, it will decrease the reaction rate. On the contrary, as seen in

Figure 3 - 3(b), the stabilization of TS_A is productive. In summary, the stabilization of TS originated from major conformer by a stereoelectronic effect will be productive if it is greater than the stabilization of reactant by same effect. The stereoelectronic control also be done by deactivation of unproductive stabilization. Going from left side to the right side of Figure 3 - 4, the stabilization of an unproductive conformer R_A by deactivating its electronic effect would remove the stereoelectronic penalty for reaching the productive TS.[15]

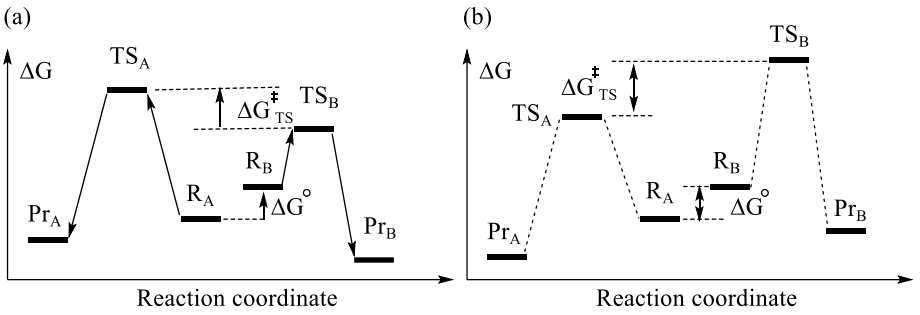

Figure 3 - 3. Comparison of TS stabilization (a) from a minor conformer and (b) from the major conformer.[14]

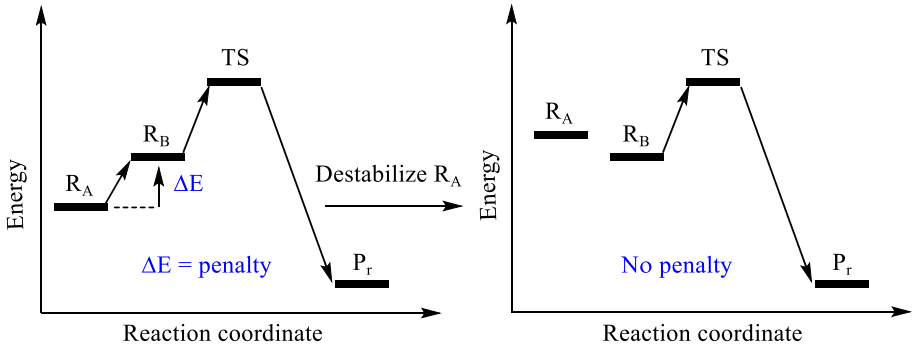

Figure 3 - 4. Destabilizing unproductive ground state.[16]

3.3.3 Ways to Elucidate Reaction Paths and Mechanism

To clarify a reaction mechanism, a systematic determination of the structures and energies of all intermediates and transition states is required. Moreover, one has to explore all the possible pathways too. However, locating all intermediates and all pathways for a reaction experimentally is difficult, expensive, and very time-consuming.

Determination of pathways can be examined in three different ways: (a) from chemical guess, (b) using experimental results, or (c) without any preconception.[17] In last decades, computational chemistry has been used as a complementary tool to help in the difficult task of reaction pathway exploration. The development of powerful theories, software tools, and capacity and speed of computers has made computational methods an almost essential help in this endeavor. Still, elucidation of reaction mechanisms computationally is not an easy task.

Until recently a "chemical guess" had been the practice to identify all intermediates and steps of all pathways of a reaction. Sometimes experiments guide the exploration of reaction pathways. Different tools like Nuclear Magnetic Resonance (NMR), Mass spectroscopy and X-ray diffraction (XRD) techniques can be used to determine the *in situ* existence and nature of an intermediate. In some cases, experimentalists are successful to trap and isolate some of the intermediates involved in a reaction.

3.4 Quantum Chemical Principles

3.4.1 Brief on Density Functional Theory

Density Functional Theory (DFT) first developed to calculate the electronic states of solids containing huge number of electrons. However, soon after, in the 1990s, DFT began to be used in calculations on molecules, and today more than 80% quantum chemical calculations are done by this predominant method.[18] Chemical reactions typically require sophisticated methods with well-balanced inclusion of dynamic and nondynamic corrections. DFT meets the requirement simply in exchange-correlation functionals of electron density. Moreover, it calculates energy quantitatively with a similar cost of the Hartree-Fock (HF) method.

The electronic wavefunction depends on $3n$ (being n the number of electrons of the system) variables: the x, y, and z-coordinates of each electron which is quite complicated. However, the total electron density $\rho(\mathbf{r})$ only depends on three variables, the x, y, and z coordinates that determine $\mathbf{r}$, the position vector in space. Therefore, $\rho(\mathbf{r})$ becomes simpler than the wavefunction and it could be a direct observable to obtain the molecular energy.

According to Hohenberg-Kohn[19] theorem, there is a unique functional such that it allows to obtain the molecular energy from the electronic density:

$$E[\rho(r)] = E_{elec} \tag{3.1}$$

where E_{elec} is the exact electronic energy. Moreover, the theorem demonstrates that the electron density obeys the variational theorem which states that for a given electron density, its energy will be greater than or equal to the exact energy. These two theorems together constitute the basis of DFT.

Kohn and Sham[20] proposed that the $E[\rho(\boldsymbol{r})]$ functional has the form:

$$E[\rho(\boldsymbol{r})] = T_{e'}[\rho(\boldsymbol{r})] + V_{ne}[\rho(\boldsymbol{r})] + V_{ee}[\rho(\boldsymbol{r})] + E_{xc}[\rho(\boldsymbol{r})] \tag{3.2}$$

In this decomposition of the energy, V_{ne} , the nuclear-electron attraction term, is:

$$V_{ne}[\rho(\boldsymbol{r})] = \sum_{1}^{N} \int \frac{Z_I}{|\boldsymbol{r} - \boldsymbol{r}_I|} \rho(\boldsymbol{r}) d\boldsymbol{r} \tag{3.3}$$

and V_{ee}, the classical electron-electron repulsion term is:

$$V_{ee}[\rho(\boldsymbol{r})] = \frac{1}{2} \iint \frac{\rho(r_1)\rho(\boldsymbol{r}_2)}{|\boldsymbol{r}_1 - \boldsymbol{r}_2|} d\boldsymbol{r}_1 d\boldsymbol{r}_2 \tag{3.4}$$

The exchange-correlation functional, $E_{XC}[\rho(\boldsymbol{r})]$, however, is the sum of exchange and correlation parts which further can be rewritten in terms of energy density ε,

$$E_{XC}[\rho(\boldsymbol{r})] = E_X[\rho(\boldsymbol{r})] + E_C[\rho(\boldsymbol{r})]$$

$$= \int \rho(\boldsymbol{r}) \varepsilon_X[\rho(\boldsymbol{r})] d\boldsymbol{r} + \int \rho(\boldsymbol{r}) \varepsilon_C[\rho(\boldsymbol{r})] d\boldsymbol{r} \tag{3.5}$$

The exchange-correlation functional is not known and it must be approximated. The development of exchange-correction functional is aimed to fulfil two criteria: (a) satisfying fundamental physical conditions and (b) accurately reproducing various reactions and properties for a wide variety of molecules. Functionals are physically assessed on the degree of which they satisfy fundamental physical conditions for each energy component. They are also numerically assessed to reproduce the energetic data and spectroscopic constants of molecules.[21]

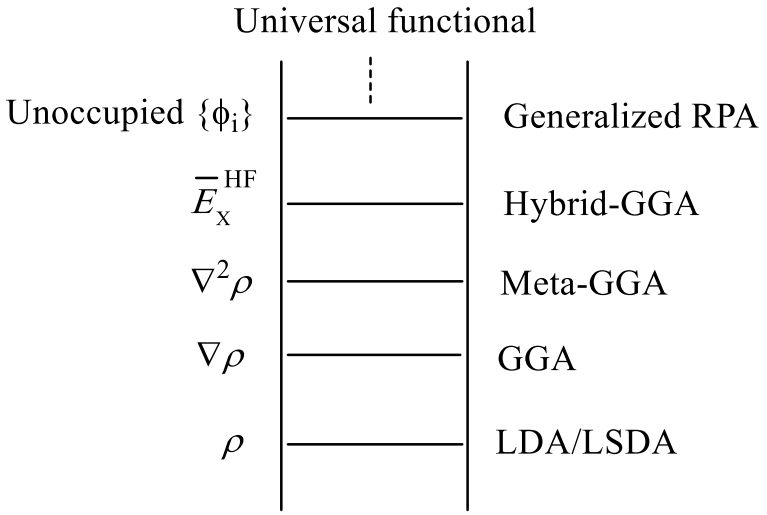

Scheme 3 - 8. Density functional approximations to the exchange-correlation energy in Jacob's ladder.[21]

Perdew[22] describes the hierarchy of approximate treatments of the exchange-correlation functional (eqn. 3.5) in the so-called "Jacob's Ladder" as depicted in Scheme 3 - 8. The ladder is grounded in HF theory, and gradually reaches the universal (exact) functional. The first rung comprises the local density approximation (LDA) functionals which only

depend on ρ. This can be extended to the local spin density approximation (LSDA) where the a and β spin densities are not equal. At the second row, the generalized gradient approximation (GGA) functionals correct LDA functionals with the density gradient $\nabla\rho$. At the third row, the meta-GGA functionals correct GGA functionals with the kinetic energy density τ. On the fourth rung, the hybrid functionals mix the HF exchange integral E_x^{HF} at constant ratio. Finally, the fifth row incorporates the unoccupied Kohn-Sham orbitals.[21]

The hybrid methods (fourth row) are among the most widely used functionals which combine the exchange-correlation functionals with some admixture of the HF exchange term. The most frequently used DFT method is the hybrid B3LYP functional which includes Becke's exchange functional along with the LYP correction functional:

$$E_{XC}^{B3LYP} = (1-a)E_X^{LSDA} + aE_X^{HF} + bE_X^{B} + (1-c)E_C^{LSDA} + cE_{CX}^{LYP} \qquad (3.6)$$

The "3" in the acronym stands for the three variables a, b, and c. Since these variables are set to reproduce the experimental data, B3LYP as well as other hybrid methods contain some degree of "semiempirical" nature. B3LYP functional frequently gives accurate chemical properties for small molecules and often it is used as a benchmark for the results of time-consuming *ab initio* wavefunction methods. However, several problems have recently been reported for this functional, particularly in the calculations of chemical reactions and properties of large systems.[21] B3LYP functional was used in the calculations in Chapter 4.

3.4.2 Corrections on Functionals

Like any theory, DFT has also its own limitations. Many corrections are incorporated in exchange-correlation functionals.[23] Among them, long-range correction, orbital energy correction and dispersion correction are discussed below.

3.4.2.1 Long-range Correction and Orbital Energy Correction

Long-range correction is the correction on the exchange functionals for long-range electron-electron exchange interactions which are insufficiently incorporated in conventional exchange functionals. Since exchange functionals are based on one-electron integrals, they always require a long-range correction. However, long-range exchange interactions are naturally integrated in the HF exchange integral which is based on an explicit two electron integral.

The long-range correction has solved the low accuracy of DFT results in a wide variety of problems such as the van der Waals binding energies, electronic excitation spectra, optical response properties, and orbital energies. Without the long-range correction, the Kohn-Sham method using any conventional functional significantly underestimates either the orbital energy gaps or the exchange-correlation integral kernel.

For LDA exchange functional, Savin[24] suggested the formulation of long-range correction (LC) scheme. Following this correction, the two-

electron operator, $\frac{1}{r_{12}}$, is divided by the standard error function as can be seen in eqn. 3.7.

$$\frac{1}{r_{12}} = \frac{1 - erf(\mu r_{12})}{r_{12}} + \frac{erf(\mu r_{12})}{r_{12}} \tag{3.7}$$

where μ is a parameter for determining the division ratio.

The CAM-B3LYP functional[25] is a long-range corrected hybrid functional using eqn. 3.8,

$$\frac{1}{r_{12}} = \frac{1 - [\alpha + \beta . erf(\mu r_{12})}{r_{12}} + \frac{\alpha + \beta . erf(\mu r_{12})}{r_{12}} \tag{3.8}$$

as a substitute of eqn. 3.7. Instead of the incomplete long-range exchange integral, this functional includes short-range HF exchange integral at a constant ratio. The CAM-B3LYP functional improves on poor atomization energies while maintains the features in the benchmark set calculations of the original long-range corrected functional. This functional was used in the study of Chapter 5.

Highly accurate HOMO and LUMO energies are reproduced by the Kohn-Sham method only using long-range corrected functionals. It seems to be the most accurate method that can quantitatively reproduce HOMO and LUMO energies simultaneously.[26]

3.4.2.2 Dispersion Correction

The dispersion interaction is a universal interaction that acts between two bodies with neither charge nor multiple moment. It is a pure electron correlation between two bodies which cannot be included in the

one-body mean-field approximation. Rather, it is a long-range correlation explicitly acting between distant electrons. It is the only van der Waals interaction that is not included in Kohn-Sham calculations using conventional correlation functionals. Dispersion is essential to correctly account for π-stacking and hydrogen bonding.

Although a number of approaches can be made for incorporating dispersion in DFT, the most utilized one is the semiclassical correction, called DFT-D, developed by Grimme[27] as can be seen in eqn. 3.9.[28]

$$E_{disp} = \sum_{AB} \sum_{n=6,8,10\ldots} s_n \frac{C_n^{AB}}{R_{AB}^n} f_{damp}(R_{AB}) \tag{3.9}$$

where A and B are the atom labels and the expansion is in the inverse of the distance between atom pairs to the sixth power, eighth power, and so on. Each term has a coefficient C_n^{AB} that depends on the atom pair AB. Moreover, each term is scaled by a coefficient s_n and f_{damp} which is a damping function for cutting off unnecessary short-range interactions.

The coefficients *C* and *s* are defined for each density functional, i.e., a set for B3LYP, another set for PBE0 and so on. Dispersion correction is denoted by adding "-D" to the name such as B3LYP-D. The latest version indicated by the suffix "-D3" includes two terms for $n = 6$ and $n = 8$.[29] The latter term aids in designing the mid-range dispersion along with long-range dispersion generally considered to follow the R^{-6} relation. Thus, B3LYP-D3 is developed based on the long-range Lennard-Jones-type potential.

Different damping functions are proposed for the damping term of the dispersion correction. The damping function of Becke and Johnson[30] leads to a dispersion energy term of order *n*:

$$E_{disp} = -\frac{1}{2}\sum_{AB}\frac{C_n^{AB}}{R_{AB}^n + const} \tag{3.10}$$

This damping term (eqn. 3.10) within the D3 correction "-D3(BJ)" is now included in Grimme's dispersion correction. D3 corrections for a range of functionals reduce noticeably the mean deviations for a benchmark data set of weak interactions, chemical reactions, and conformations at least by 1 kcal mol^{-1}. B3LYP-D3 model has been proven to produce excellent results in studies of molecular geometry of weakly interacting systems.[31] Dispersion correction was used in all quantum chemical calculations of the thesis.

3.4.3 Basis Set and its Superposition Error

To obtain the energy and wavefunction within the Hartree-Fock-Roothaan procedure, the atomic orbitals (AOs) must be specified. If the set of AOs is infinite, then according to the variational principle, one gets the lowest possible energy within the HF-SCF method. This is called HF limit, E_{HF}, although, it is not the actual energy of the molecule as the HF method neglects instantaneous electron-electron interactions also known as electron correlation. The choice which truncates the impractical infinite expansion of AOs defines the basis set.

The choice of the basis set is an important factor in carrying out computations. To reproduce accurate chemical reactions and properties, one needs to choose basis functions that give highly accurate molecular orbitals with a minimum number of functions. The choice of an appropriate basis set depends on the nature of the molecules and reactions in question. Major types of basis sets include minimal, Pople-type, Dunning's correlation-consistent basis sets, and effective core potential (ECP) basis sets.[32]

The basis set introduced by Pople is made up of core orbitals with valence basis functions that are split into those using contracted Gaussian-type orbitals (CGTOs) and uncontracted Gaussian-type orbitals (GTO). Pople basis sets are often called split-valence basis sets. Often, Pople basis sets are accompanied by polarization functions that introduce higher-order orbitals to hydrogen and nonhydrogen atoms yield in more accurate results. For example, polarization basis set 6-31G** or 6-31G (d, p) indicates that the hydrogen atoms have p-type Gaussian orbitals whereas the nonhydrogen atoms contain d-type Gaussian orbitals. Computations of anions, cations, and diradicals require basis sets with diffuse functions, denoted by + or ++.

Dunning's correlation-consistent basis sets have polarization functions to correlate the valence electrons. In the acronym cc-pVXZ, the "cc" stands for correlation-consistent, "pV" means the polarized valence shells, and "XZ" can be "double zeta" or "triple zeta" and so on. To include the diffusion functions, one adds "aug-" before the basis set of

choice which means the basis sets have been augmented "with additional functions optimized for atomic anions".

Effective core potential (ECP) basis sets, such as LanL2DZ and Stuttgart-ECP, approximate core orbitals. In most systems, they hardly affect reactions and properties and drastically reduce the number of basis functions. ECP basis sets can be used in most cases except for the reactions and properties where core electrons participate. In particular, they are most often used in fourth-period atoms or latter. However, for smaller metal complexes, the speedup gain by ECP doesn't compensate the ignorance of having the polarization functions. Moreover, most ECP bases exclude diffuse functions, thus, it is not worthy to use them for systems with localized anions.

The basis set superposition error (BSSE)[33] is attributed to the artificial stabilization of the energy coming from the overlap of nonorthogonal basis functions. Atoms approaching closer to each other suffers this error. The counterpoise method is frequently used to remove this error. For example, if a system AB is calculated with a+b basis functions, the counterpoise method estimates the BSSE as:

$$\Delta E = E_A^{a+b} + E_B^{a+b} + E_A^a + E_B^b \tag{3.11}$$

where E_A^{a+b} refers the energy of system A calculated with both a and b basis functions. The BSSE (ΔE) is then subtracted from the total energy. The BSSE in calculating weak bonds (e.g., van der Waals bonds) is crucial. However, overlap of basis functions is obvious in chemical bonds. Therefore, the BSSE is neglected in most calculations involving

reactions and properties. The effect of BSSE was checked for the calculations in Chapter 4.

3.4.4 Computational Methods to Explore PES

A PES describes how the energy of a molecule or cluster changes with the change of its nuclear positions and associated electron distribution for a given electronic state. In general, the interesting structures of chemical interest on the PES are critical points (also called stationary points) at which the first derivatives of the potential energy with respect to each geometric parameter are zero:

$$\frac{\partial E}{\partial q_1} = \frac{\partial E}{\partial q_2} = \cdots = 0 \tag{3.12}$$

Critical points are characterized by the eigenvalues of the Hessian matrix evaluated at the point of interest. The matrix elements of the Hessian, in general, are defined as eqn. 3.13.

$$H_{ij} = \partial^2 E \Big/ \partial q_i \partial q_j \tag{3.13}$$

where q_i is an atomic coordinate. The eigenvalues correspond to the curvatures associated with the normal vibrational modes. If all the eigenvalues of the vibrational modes are positive, then the critical point is a local minimum. However, the critical point is a TS if there is one and only one negative eigenvalue.[34]

At the TS, the only negative eigenvalue of the Hessian matrix corresponds to the eigenvector that is downhill in energy which is

commonly referred to as the reaction coordinate. Tracing out the steepest descendent vector from the TS, with the initial direction given by the eigenvector with the negative eigenvalue, the minimum energy path (MEP) linking two minima is obtained.[34] If this calculation is performed using mass-weighted coordinates, the path is usually called the intrinsic reaction coordinate (IRC).

3.4.5 Frequency Calculation and Free Energy

After a geometry optimization, one needs to conduct a frequency calculation on the optimized structure to assess the character of the stationary point located (minima have no imaginary frequencies, TSs have single imaginary frequency, and structures with more than one imaginary frequency are generally not relevant to a reaction), and to calculate the zero-point energy, internal energy, enthalpy, and free energy of a molecule. Frequencies are obtained from the diagonal terms of the Hessian matrix (eqn. 3.13). The square root of the mass-weighted Hessian eigenvalue is proportional to the vibrational frequency, ω_i whereas the eigenvector defines the atomic motion associated with that frequency. Within the harmonic oscillator approximation, the zero-point vibrational energy (ZPVE) is obtained by:

$$ZPVE = \sum_{i}^{vibrations} \frac{h\omega_i}{2} \tag{3.14}$$

The Gibbs free energy (G), is the thermodynamic magnitude that gives the spontaneity criteria of any process that takes place at constant pressure and temperature so, for this reason, it is the quantity that should be used to compare computational results with the experimental ones.

The entropy correction for an individual molecule comes from the relative motion of nuclei within the molecule. However, one needs to consider additional entropic factors when looking at ensembles of molecules. If a calculation is done for an ideal gas while the experimental system is in solution, the standard state of the molecule needs to be changed from a pressure of 1 atm to a concentration of 1 M. Such correction is essential when the number of molecules changes along the reaction path in the solution phase. If one of the reactants is a solvent molecule that comes from neat solvent, the standard state correction for only that solvent molecule needs to include an additional correction for the concentration of the solvent in its neat form.[35]

3.4.6 Solvation

The solvation models try to reproduce computationally the effect of the solvent when the system is in a condensed phase environment. This makes the modeling an organic reaction mechanism more realistic. Under certain conditions, solute molecules may change the solvent structure in the vicinity of the solute resulting in a free energy change. As can be seen in Figure 3 - 5, selective stabilization of the TS relative to the previous minimum energy structure for a rate-determining step can be

accomplished by changing the solvent. For this reason, it is important to include solvent either implicitly or explicitly.

Solvent can affect a reaction through short-range interactions like hydrogen bonding or through a long-range interactions like polarization. To reproduce computationally the first of these effects, we should include explicit solvent molecules in the model, enlarging the size of the system and consequently making more expensive the calculation. On the other hand, long-range effects can be reproduced considering the solvent in bulk, what only affect marginally the cost of the calculations.

There are many kinds of implicit models that treat solvent as a continuum. An implicit solvent model has a solute molecule placed in a cavity of a solvent with a fixed dielectric constant. The cavity of vacuum is set into the solvent. The solute charge density is then placed in the solute cavity. Thus, the solute is polarized in response to the solvent polarization.

The density-based solvation model (SMD) and the polarizable continuum model (PCM) are commonly used implicit solvent models. The SMD model uses the full solute electron density and separates the solvation free energy into an electrostatic component and interactions between solute and solvent in the first solvation shell. It uses the electron density to calculate the solvent accessible surface area (SASA) and determines dispersion-repulsion energies. This is the model that will be used along this work.

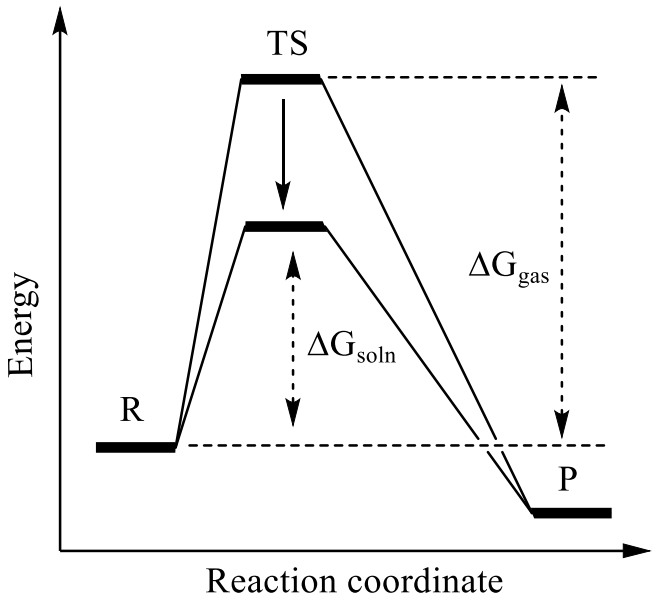

Figure 3 - 5. Solvent effect on a PES. If the solvent stabilizes the TS more than R, the relative energy of TS decreases, thus, decreases the free energy barrier i.e., $\Delta G_{soln} < \Delta G_{gas}$.[36]

3.5 References

(1) Lundgren, R. J.; Stradiotto, M. Key Concepts in Ligand Design. In *Ligand Design in Metal Chemistry*; John Wiley & Sons: West Sussex; UK, 2016; pp 1–14.
(2) Allen, A. E.; MacMillan, D. W. C. *Chem. Sci.* **2012**, *3* (3), 633–658.
(3) Moberg, C. Lewis Acid–Lewis Base Catalysis. In *Cooperative Catalysis*; John Wiley & Sons: Weinheim, 2015; pp 35–66.
(4) Wang, S.; Xi, C. *Chem Soc Rev* **2019**, *48* (1), 382–404.
(5) Liu, M.; Wang, X.; Jiang, Y.; Sun, J.; Arai, M. *Catal. Rev.* **2019**, *61* (2), 214–269.
(6) Gothelf, K. V. Asymmetric Metal-Catalyzed 1,3-Dipolar Cycloaddition Reactions. In *Cycloaddition Reactions in Organic Synthesis*; John Wiley & Sons: Weinheim, 2001; pp 211–247.
(7) Bruckner, R. Thermal Cycloadditions. In *Org. Mech;* Springer-Verlag: Berlin, 2010; pp. 643–689.

(8) Vogel, P.; Houk, K. N. Catalytic Reactions. In *Organic Chemistry: Theory, Reactivity and Mechanisms in Modern Synthesis*; Wiley-VCH, 2019; p 855.
(9) Monica, F. D.; Kleij, A. W. *Catal. Sci. Technol.* **2020**, *10* (11), 3483–3501.
(10) Hehre, W. J. A Guide to Molecular Mechanics and Quantum Chemical Calculations; Wavefunction, Inc., 2003; p 15.
(11) Vogel, P.; Houk, K. N. Catalytic Reactions. In *Organic Chemistry: Theory, Reactivity and Mechanisms in Modern Synthesis*; Wiley-VCH, 2019; p 797.
(12) Hehre, W. J. A Guide to Molecular Mechanics and Quantum Chemical Calculations; Wavefunction, Inc., 2003; p 393.
(13) Gomez, G. dos P.; Alabugin, I. V. Stereoelectronic Effects: Analysis by Computational and Theoretical Methods. In *Applied Theoretical Organic Chemistry*; World Scientific, 2018; p 451.
(14) Alabugin, I. V. Transition State Stabilization with Stereoelectronic Effects. In *Stereoelectronic Effects*; John Wiley & Sons: West Sussex, UK, 2016; pp 236–256.
(15) Alabugin, I. V. Stereoelectronic Effects in Reaction Design. In *Stereoelectronic Effects*; John Wiley & Sons: West Sussex, UK, 2016; pp 257–274.
(16) Alabugin, I. V. Stereoelectronic Effects in Reaction Design. In *Stereoelectronic Effects*; John Wiley & Sons: West Sussex, UK, 2016; p 261.
(17) Ramozzi, R.; Sameera, W. M. C.; Morokuma, K. Predicting Reaction Pathways from Reactants. In *Applied Theoretical Organic Chemistry*; World Scientific, 2018; p 321.
(18) Tsuneda, T. *Density Functional Theory in Quantum Chemistry*; Springer: Tokyo, 2014.
(19) Hohenberg, P.; Kohn, W. Inhomogeneous Electron Gas. *Phys. Rev.* **1964**, *136* (3B), B864.
(20) Kohn, W.; Sham, L. J. *Phys. Rev.* **1965**, *140* (4A), A1133.
(21) Tsuneda, T. Exchange-Correlation Functionals. In: *Density Functional Theory in Quantum Chemistry.*; Springer: Tokyo, 2014, pp. 101-124.
(22) Perdew, J. P.; Ruzsinszky, A.; Tao, J.; Staroverov, V. N.; Scuseria, G. E.; Csonka, G. I. *J. Chem. Phys.* **2005**, *123* (6), 062201.
(23) Tsuneda, T. Corrections for Functionals. In: *Density Functional Theory in Quantum Chemistry.*; Springer: Tokyo, 2014, pp. 125-160.
(24) Savin, A. *Theor. Comput. Chem.* **1996**, *4*, 327–357.
(25) Yanai, T.; Tew, D. P.; Handy, N. C. *Chem. Phys. Lett.* **2004**, *393* (1–3), 51–57.
(26) Tsuneda, T. Orbital Energy. In *Density Functional Theory in Quantum Chemistry.*; Springer: Tokyo, 2014, pp. 161–188.
(27) Grimme, S. *J. Comput. Chem.* **2004**, *25* (12), 1463–1473.
(28) Bachrach, S. M. Computational Organic Chemistry; John Wiley & Sons, Inc., 2014; p 27.
(29) Grimme, S.; Antony, J.; Ehrlich, S.; Krieg, H. *J. Chem. Phys.* **2010**, *132* (15), 154104.
(30) Becke, A. D.; Johnson, E. R. *J. Chem. Phys.* **2005**, *122* (15), 154104.
(31) Hujo, W.; Grimme, S. *J. Chem. Theory Comput.* **2013,** *9* (1), 308-315.
(32) Tsuneda, T. Hartree–Fock Method. In *Density Functional Theory in Quantum Chemistry*; Springer: Tokyo, 2014; p 50.
(33) Tsuneda, T. Hartree–Fock Method. In *Density Functional Theory in Quantum Chemistry*; Springer: Tokyo, 2014; p 53.
(34) Bachrach, S. M. Computational Organic Chemistry; John Wiley & Sons, Inc., 2014; p 41.

(35) Hare, S. R; Hudson, B. M.; Tantillo, D. J. Modeling Organic Reactions — General Approaches, Caveats, and Concerns. In *Applied Theoretical Organic Chemistry*; World Scientific: Europe, 2018; p 4.
(36) Hare, S. R; Hudson, B. M.; Tantillo, D. J. Modeling Organic Reactions — General Approaches, Caveats, and Concerns. In *Applied Theoretical Organic Chemistry*; World Scientific: Europe, 2018; p 15.

CHAPTER 4:

Lignocellulosic Materials in CO_2 Cycloaddition: Exploring Mechanisms Guided by Experiments†

4.1 Introduction

Biomasses are renewable organic matters found in various plants and animals such as agricultural crops and wastes, wood and wood wastes, animal wastes, and in municipal and industrial wastes. Biorefineries use biomass to produce chemicals, biofuels, electricity, steam, pulp, and papers. Biomasses can be extracted from palm and vegetable oils, from sucrose derived from sugar cane and sugar beets, from starch-containing crops like corn, and from lignocellulosic sources such as trees, shrubs, and grasses.[1] Due to the higher yields per area of land, lignocellulosic biomass is the most abundant plant material on Earth. Its use as biofuel feedstock is prone to reduce carbon dioxide emissions.

The major components of lignocellulosic biomass are cellulose, hemicellulose, and lignin whose structures are shown in Scheme 4 - 1. Although, depending on the species, it has varied compositions, in general, lignocellulosic biomass contains 35-50% cellulose as the main

† The results of this chapter were published in reference no. 4.

constituent along with 20-35% hemicellulose, and 15-25% lignin.[2] The interactions among different components are not fully understood and therefore the detailed structural knowledge of lignocellulosic biomass is still under development.[3]

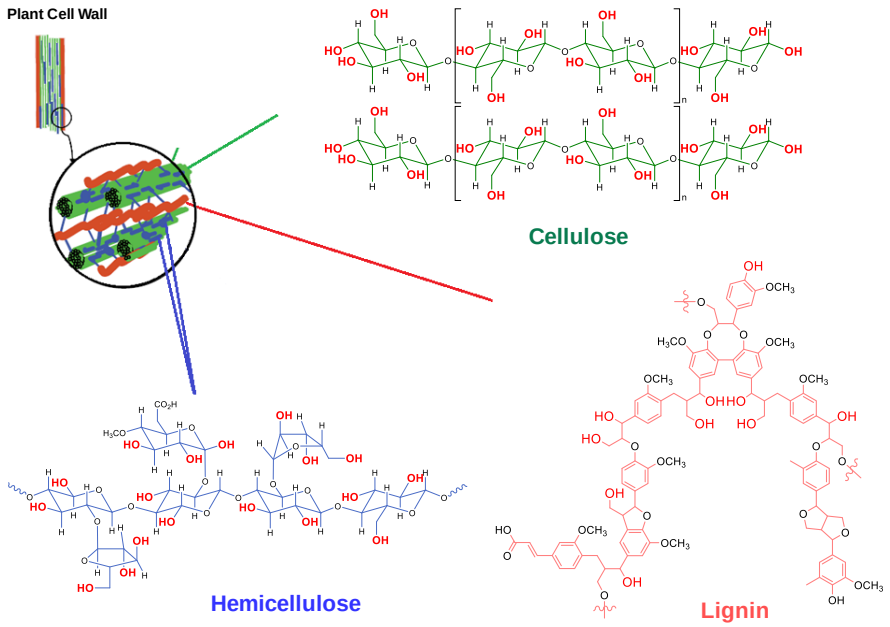

Scheme 4 - 1. Basic structure of cellulose, hemicellulose and lignin constituents in the cell walls of lignocellulosic biomass.[4]

Studies on the interactions among various plant cell wall components have been carried out by quantum chemical calculations.[5,6] In these DFT studies, a glucose tetramer was chosen as a representative cellulose structure whereas a coniferyl alcohol tetramer was used to represent the basic lignin structure of lignocellulose. However, lignin contains three basic aromatic monomers namely p-coumaryl alcohol,

coniferyl alcohol, and sinapyl alcohol shown in Scheme 4 - 2.[7] Although the complete chemical structure of lignin is not exactly determined, it is known to contain various functional groups including methoxyl, phenolic hydroxyl, aliphatic hydroxyl, and other carbonyls groups.[8] Martin-Martinez et al.[9] performed a multiscale modeling of lignocellulosic biomass using a model constituted by the aforementioned aromatic alcohol monomers. The resulting standard lignin structure is shown in Scheme 4 - 3.

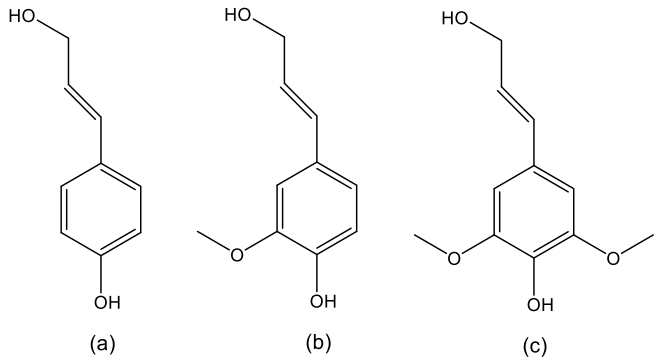

Scheme 4 - 2. Monomers in Lignin: (a) p-coumaryl alcohol (b) coniferyl alcohol and (c) sinapyl alcohol.

Biomass can also be used as organocatalyst for different transformations. Organocatalysts are usually less active in CO_2 cycloaddition to epoxides than metal-containing catalysts. However, in terms of costs and sustainability, transition metal-free catalysts are desirable. Under mild conditions, hydrogen bond donor (HBD) organocatalysts cooperating with nucleophiles can selectively couple CO_2

and epoxides into cyclic carbonates.[10,11] However, either HBD or nucleophile alone results in low product yield.

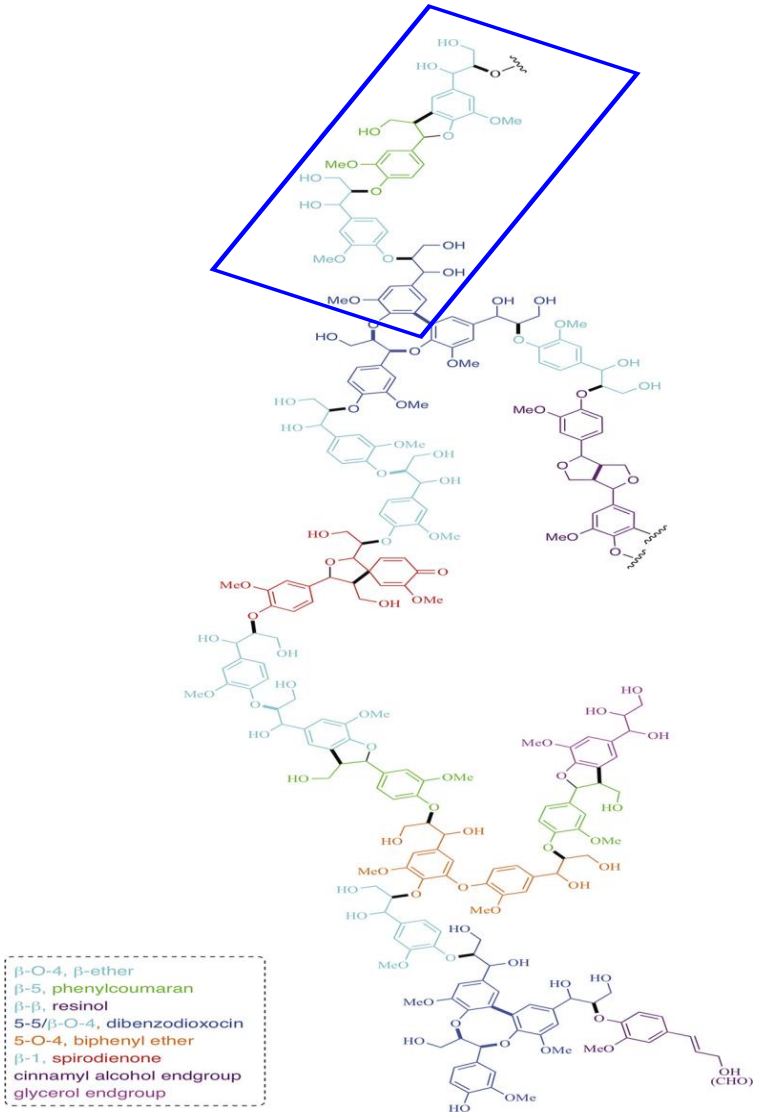

Scheme 4 - 3. Different structural constituents of a standard lignin model. The coniferyl alcohol tetramer motif is highlighted in blue. (Reproduced from Martin-Martinez et al.[9] with permission)

HBDs are known to activate epoxides by binding their oxygen to form H-bonds. Some HBDs can also simultaneously activate CO_2. A nucleophile then attacks the activated epoxide to facilitate its ring opening. From the broadest family of hydroxyl HBDs, the simple diols and simpler polyhydroxyphenolic moieties are represented in Scheme 4 - 4.

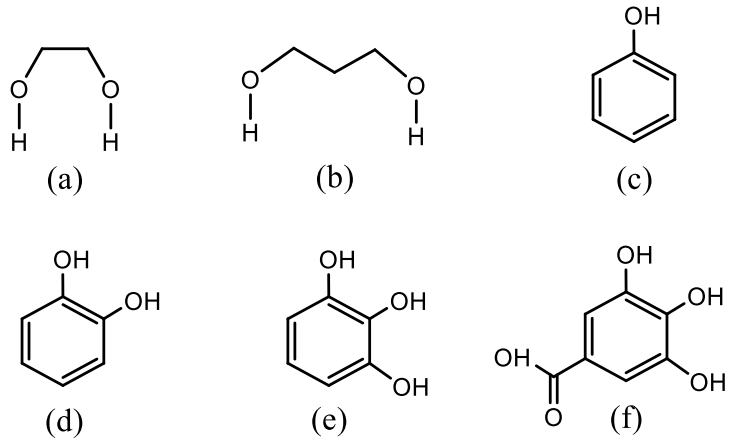

Scheme 4 - 4. Basic hydroxyl units of HBD catalysts: (a) 1,2-diol, (b) 1,3-diol, (c) phenol, (d) catechol, (e) pyrogallol, and (f) gallic acid.

Liu et al.[12] studied the synthesis of propylene carbonate (PC) catalyzed by different HBDs and 1-(2-hydroxyl-ethyl)-3-buthylimidazolium bromide (HEBimBr) as a nucleophile. The study shows that ethylene glycol with two vicinal -OH groups, Scheme 4 - 4 (a), gives a high PC yield of 96% whereas the reaction yield with a single -OH group containing catalyst, ethanol, is only 64%. Moreover, their DFT calculations suggest that the formation of a H-bond between the 1,2-diol

and the oxygen atom of the substrate propylene oxide (PO) remarkably reduces the energy barrier of the epoxide ring opening. In addition, due to this strong H-bonding, ethylene glycol further stabilizes the ring-opened intermediate and the subsequent transition state, therefor, promoting the cycloaddition reaction efficiently.

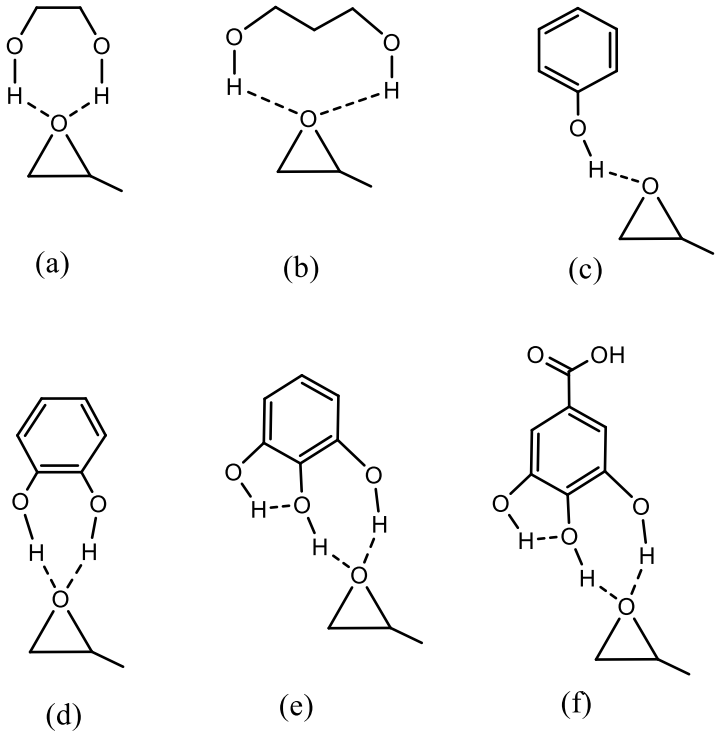

Scheme 4 - 5. Some representative H-bonding interactions of PO with (a) 1,2-diol, (b) 1,3-diol, (c) phenol, (d) catechol, (e) pyrogallol, and (f) gallic acid.[13,14]

Phenol and its derivatives, Scheme 4 - 5 (c-f), are one of the mostly studied class of hydroxyl HBDs to accelerate the CO_2 cycloaddition to epoxides.[15] Wang et al.[13] show that phenolic HBDs are more efficient than alcohols. In an extended study, Whiteoak et al.[14] revealed that catalytic

activity of phenolic derivatives changes with the variation of electron withdrawing or releasing capacity of the substituents in the *ortho*-, *meta*, or *para*-position of phenol. Moreover, from a steric hindrance viewpoint, the strength of H-bonds also would change with the readiness of the binding mode(s). Besides the substrate activation, the -OH groups also can direct the way of chemical conversions.[16] In the formation of cyclic carbonate, catechol displays higher activity and selectivity compared to phenol (Scheme 4 - 6). Phenol (10 mol%) and catechol (5 mol%) with co-catalyst TBAB provided 39% and 92% PC yields, respectively at 100 ^{o}C, 30 bar CO_2 in 0.5h.[10,13] However, having three neighboring -OH groups, a small amount of pyrogallol (2 mol%) with the co-catalyst tetra-n-butylammonium iodide (TBAI) gave 96% PC yield at 25 ^{o}C, 10 bar CO_2 in 18h.

Apart from their biomass conversion into chemicals[17], lignocellulosic biomass acts as a hydrogen bond donor catalyst for CO_2 coupling with epoxides.[15] In fact, its major constituent cellulose is a poly(D-glucose) that promotes CO_2 cycloaddition to epoxides in presence of alkali halide salts or organic bases. This abundant carbohydrate polymer is rich in vicinal -OH groups (see Scheme 4 - 1) and activates epoxides through the formation of a seven-membered ring, like that of 1,2-diol shown in Scheme 4 - 5 (a). Moreover, lignin part (see Scheme 4 - 3) of lignocellulosic biomass is a multiphenolic cross-linked polymer with a lot of two and three neighboring -OH groups and can fasten the CO_2 cycloaddition to epoxides in combination with organic bases. Lignin is expected to be more active than cellulose due to its structural resemblance

to simple multiphenolic compounds such as pyrogallol or catechol which are more efficient than aliphatic alcohols.

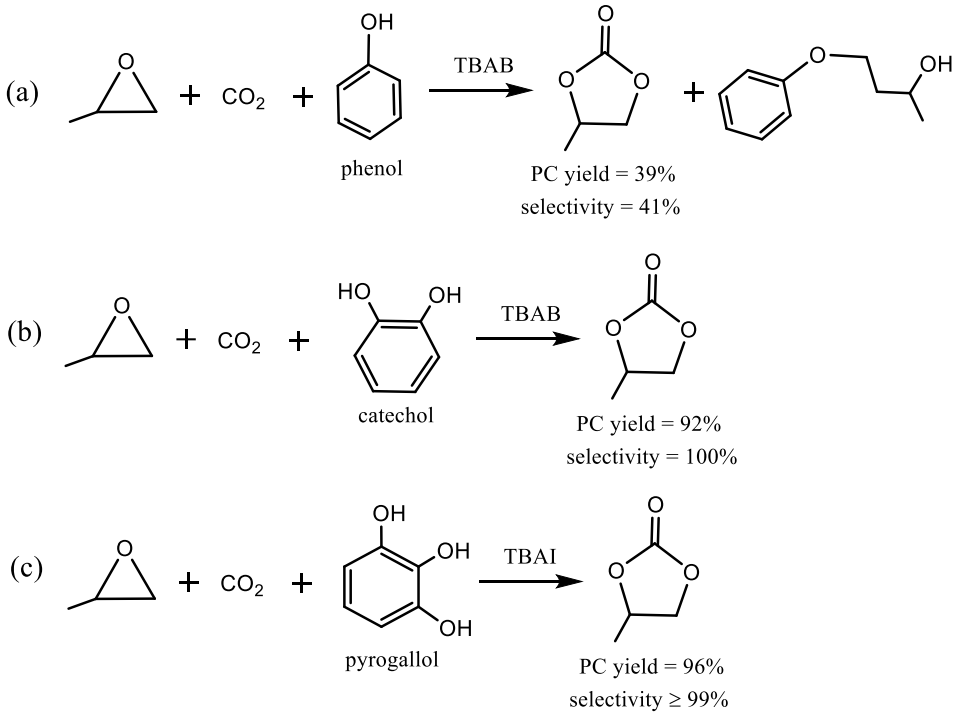

Scheme 4 - 6. CO_2 cycloaddition to PO catalyzed by (a) phenol/TBAB, (b) catechol/TBAB, and (c)pyrogallol/TBAI binary systems.[10,14]

Our group reported the catalytic activity of various lignocellulosic wastes in combination with nucleophiles for the cycloaddition of CO_2 with epoxides.[4] Vegetal residues from sugar cane bagasse, olive bone external, grape waste, grape pit etc. are shown as inexpensive, renewable, and green catalysts for the synthesis of cyclic carbonates. Although, depending on the origin of the residues, the overall catalytic conversion of CO_2 cycloaddition to 1,2-epoxyhexane by the lignocellulose/TBAB

binary systems varied from a 47% to a 79%, the study did not show any clear correlation between lignin or holocellulose content and conversion.[4]

In the study described in this chapter, we wanted to rationalize the performance of lignocellulosic materials as catalysts in CO_2 cycloaddition to epoxides to form cyclic carbonates. For this, we determined experimentally the catalytic activity of isolated cellulose and lignin components and performed a computational study to elucidate the mechanism of the reaction of interest catalyzed by models to represent both components. They were considered as natural hydroxyl HBD catalysts given that the cellulose part of lignocellulose is analogous to 1,2-diols whereas the lignin part is analogous to 1,3-diols of polyhydroxyphenolic catalysts (more in section 4.3.2). The % substrate conversion by the experimental catalyst systems were compared with the energy barriers of the rate determining step of the reaction paths found for the modeled reactions.

4.2 Catalytic Experiments and Computational Models

4.2.1 Catalytic Experiments

Catalyst material holocellulose (HC) and acid insoluble lignin (AIL) were ready from a previous work.[4] Benchmark substrate, 1,2-epoxyhexane (EPH) was received from Sigma Aldrich. CO_2 cycloaddition

reaction with 1,2-epoxyhexane was carried out at 95 ^{o}C, under 10 bar CO_2 pressure during 16h. Tetrabutylammonium bromide (TBAB) was used as co-catalyst. CO_2 gas cylinders of 99.99% purity were purchased from Linde, Germany.

The catalytic experiments were carried out in a 100 mL Berghof autoclave reactor. Reactions were set at 950 rpm (rotations per minute) stirring. After the reaction time, the autoclave was cooled in an ice bath until room temperature, and the pressure was released. Then, the autoclave was opened, and the content was analyzed by ^{1}H NMR spectroscopy using mesitylene as internal standard. ^{1}H NMR were recorded in a Varian spectrometer at room temperature in $CDCl_3$. Chemical shifts were reported in parts per million (ppm, δ). The %conversion was determined from ^{1}H NMR of the crude mixture from the integral ratio of the produced cyclic carbonate and individual substate fed.

4.2.2 Computational Models

The computational study was performed by means of DFT calculations. The B3LYP functional was chosen to be used due to its good performance in similar systems. The D3 version of Grimme's empirical dispersion was plugged in to the model to correct the basis set superposition error (BSSE) among the reaction moieties. The 6-31+G(d,p) basis set was used for main group atoms and LanL2DZ for heavier Br atom. This level of calculation, used in geometry optimizations and frequency calculations, will be represented from now on as *Level-1*. To

refine the final energies, single-point energy calculations were performed on the previously optimized geometries using B3LYP-D3BJ [18,19] method with 6-311+G (2df,p) basis set for main group atoms and SDD basis set for Br atom. This more consuming level of calculation will be denoted as *Level-2*.

The Solvation Model Based on Density (SMD) was used to describe the reaction media as a polarizable continuum.[20] In the theoretical study, to decrease computational costs, propylene oxide (PO) was selected as the model epoxide. To reproduce its effect as a solvent, we took 2-butanol instead from the Gaussian library, given that it has similar properties to PO, with a dielectric constant ε = 15.94 (ε =16 for PO) and a refractive index, η_D = 1.397 (η_D = 1.366 for PO). [18,21,22]

To afford geometry optimization calculations, the geometries of cellulose and lignin (see Figure 4 - 1) were frozen except for the hydroxyl groups that could potentially interact with the substrates. The skeleton geometry used was optimized in a calculation where the catalyst was the only species in the system, considering the PO solvent as a polarizable continuous media.

To consider the entropic effect, the reaction barriers are reported in terms of free energy of activation (ΔG‡) which is the free energy difference between each transition state and the previous stable structure along the reaction path (reactants or intermediates). The Gibbs free energy changes ΔG are calculated according to eqn. 4.1.

$$\Delta G = \Sigma(\varepsilon_0 + ZPVE + G_{corr})_{product} - \Sigma(\varepsilon_0 + ZPVE + G_{corr})_{reactant} \quad (4.1)$$

where ε_0 is the total electronic energy (calculated in this case at *Level-2*), ZPVE is the zero-point vibrational energy and G_{corr} is the thermal correction to Gibbs free energy, both calculated at *Level-1*. Final values of ΔG in the profiles also include a correction of 1.89 kcal mol^{-1}, for each reactant moiety. This value comes from the term $RT\ ln\ (c_s / c_g)$, that accounts for the change on the Gibbs free energy value due to the change from the standard condition in the gas phase (1 atm) to the standard state in solution (1 mol L^{-1}).[23] For this reason, c_s is the standard molar concentration in solution (1 mol L^{-1}) and c_g is the standard molar concentration in the gas phase (0.0446 mol L^{-1}), considering the reaction at 298 K, and being R the gas constant.

The reference energy of the reactants was obtained computing the energy of CO_2 in an independent calculation, considering that this reactant does not interact initially with the species formed by the catalytic system with the PO substrate and the bromide ion. However, all other intermediates, transition states, and products were studied including all the moieties together.

The intrinsic reaction coordinate (IRC) method was used to confirm that the TSs connect the desired minima. However, in the cases where the IRC calculation did not converge, the appropriateness of the transition state was checked by the analysis of the reaction coordinated given by the normal mode with imaginary frequency.

All the calculations were performed using computational chemistry package Gaussian 16.[22] The atomic charge distributions were

calculated by Mulliken analysis. Comparison of our results with previously published data for the reaction catalyzed by TBAB gave noticeable discrepancies which was analyzed in detail. Test calculations (see section 4.A, Appendix) indicated that small numerical differences were due to different versions of the computational program used and to the solvent considered, but the most significant discrepancy came from the solvent model used, PCM (Polarizable Continuum Model) in previous calculations *vs.* the more recent SMD one used in this work.

4.3 Experiment Driven Mechanistic Exploration

4.3.1 Catalytic Activity of Lignin and Cellulose

To understand the contribution of the components of lignocellulosic materials in the catalytic performance, lignin and cellulose were isolated from the waste samples and its catalytic activity was studied. AIL and HC content were separated in a previous work following established methods.[4]

When AIL and HC were used as catalysts under the same reaction conditions, the conversion of the substrate EPH obtained with the catalytic system AIL/TBAB was higher (72%) than the conversion obtained with holocellulose/TBAB (38%). The Brönsted acidity of the hydroxyl groups (in pKa) of HBD catalysts has been related to the catalytic activity in CO_2

cycloaddition to epoxides. Therefore, an ideal range of 9<pKa<11 has been identified which includes phenolic derivatives such as the ones contained in lignin structure. Nevertheless, there can be other factors associated with this increment of catalytic activity of lignin with respect to holocellulose. For this reason, they are seen as a subject of mechanistic studies.

4.3.2 Modeling Lignocellulosic Catalytic Systems

To unfold the above reasoning, the HC and AIL part of the lignocellulosic residues were modeled. Cellulose was modelled by cellutriose (CtS), as shown in Scheme 4 - 7(a). Based on previous studies[24], CtS was chosen as the model of cellulose which consists three β-D-glucose units connected through β-1,4-glycosidic linkages. The lignin of the lignocellulosic residues was modelled by four monomeric coniferyl alcohol motifs linked via β-O-4 ether bonds (LiG, Scheme 4 - 7(b)), also based on previous studies.[6] One of the main differences of these catalysts is that CtS is a 1,2-diol (with two vicinal -OH groups) whereas the active sites of LiG contain two -OH groups in 1,3– relative positions, as compared in Figure 4 - 1.

TBAB was considered as cocatalyst. Nevertheless, test calculations didn't show any interaction between TBA+ and the substrate. Since the cation TBA^+ did not play any role (see section 4.B, Appendix), only the Br^- anion was included in the computed system.

The substrate used to study the reaction was PO. Therefore, the reaction profiles of CO_2 cycloaddition to PO were carried out with a) CtS

+ bromide and b) LiG + bromide systems. We also modelled the reaction only with TBAB as catalyst to compare with previous studies [6,19,25] (see details in Table 4A – 1, Appendix).

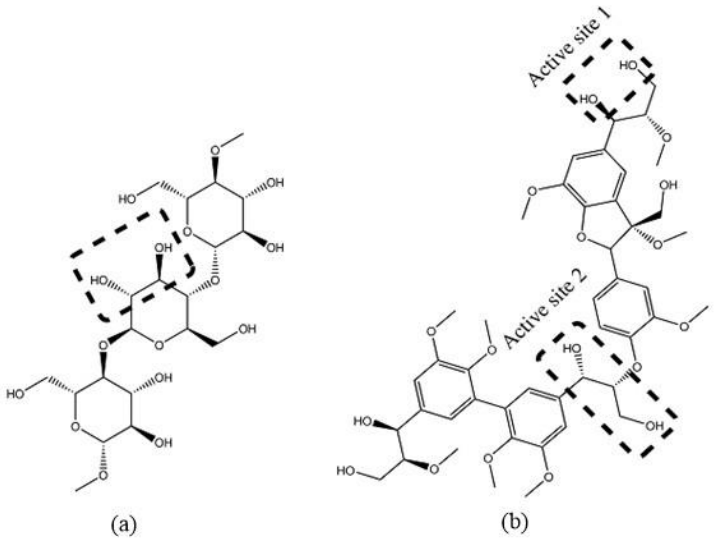

Scheme 4 - 7. Schematic (a) cellutriose (CtS) and (b) lignin (LiG) model. Catalytic active sites are highlighted in square dashed boxes. CtS has only one active site whereas LiG has two possible active sites: active site 1 and active site 2.

To analyze the interaction between a catalyst (CtS or LiG) and the substrate PO, the latter was placed in different positions around the catalyst, always close to the -OH groups. In this way, we identified the active sites that showed the strongest interaction with the substrate to select the most appropriate reaction path to follow. Active site used in CtS is highlighted by a square dashed box in Scheme 4 - 7(a). In case of LiG, the active sites 1 and 2 were tested as can be seen in Scheme 4 - 7(b). The active site 1 was found the strongest interaction with the substrate. So, the

study of the mechanism was initiated from the interaction of the substrate with this site.

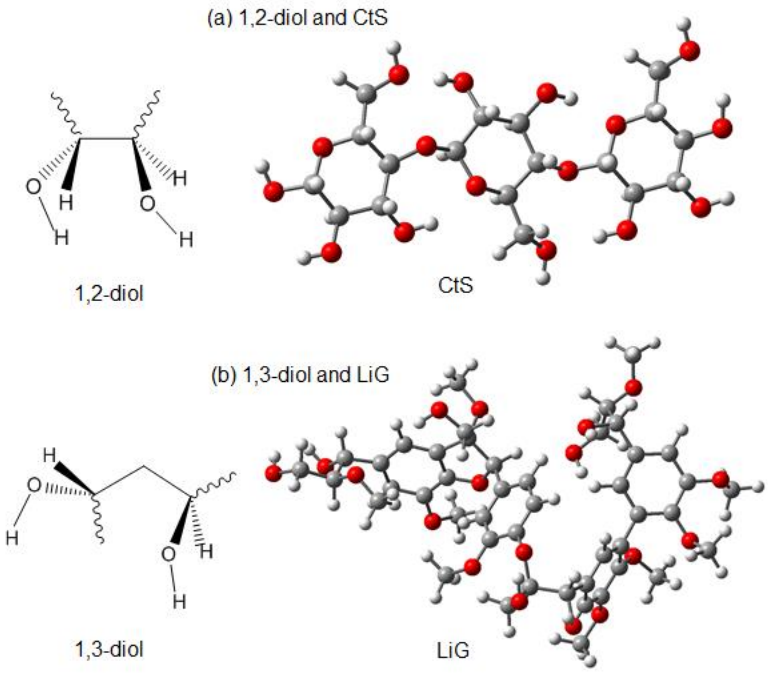

Figure 4 - 1. Comparing (a) 1,2-diol with CtS and (b) 1,3-diol with LiG model.

4.3.3 Reaction Paths

TBAB-catalyzed CO_2 cycloaddition to PO is considered as the reference reaction. Based on reported studies[19], the assumed reaction pathway using TBAB as catalyst includes the following steps: PO ring-opening by the nucleophile Br^-, CO_2 insertion and ring closure to form the cyclic carbonate. In substituted epoxides ring-opening may take place at

the more substituted carbon atom, C_a, or at C_b instead. In the case of PO it is already known that the nucleophile attack favored is the one to the less hindered non-substituted carbon C_b.[25,26] We obtained that the rate-determining step for the reaction with TBAB as only catalyst is the initial ring-opening of the epoxide by the nucleophilic attack of Br^- with an activation energy of $\Delta G^{\#} = 16.09$ kcal mol^{-1} (see Figure 4B – 1, Appendix).

Next calculations began optimizing the CtS and LiG models obtaining the geometries shown in Figure 4 - 1. Then, we explored the potential energy surface (PES) of the ground states of the catalytic CtS/TBAB and LiG/TBAB systems along the most plausible paths.

Figure 4 - 2 and Figure 4 - 3 show the reaction profiles found for reactions with CtS/TBAB and LiG/TBAB catalytic systems, respectively. The geometries of the critical points for catalytic CtS/TBAB and LiG/TBAB systems are shown in Figure 4 - 4 and in Figure 4 - 5 respectively.

Given that in the experimental setup the epoxide is the solvent, the interaction between the vegetal material and the epoxide is considered to exist before the reaction begins. So, the reactants are modelled with a biopolymer-PO adduct plus Br^- and CO_2. In both CtS and LiG cases, the catalytic cycle initiates with the interaction of the epoxide with two consecutive hydroxyl groups of the vegetal material through two H-bond (Int1, Figure 4 - 2 and Figure 4 - 3). The intermediate Int1 formed with LiG is more stable than the one formed with CtS by 1.24 kcal mol^{-1}. This suggests a slightly more efficient interaction of the epoxide with LiG.

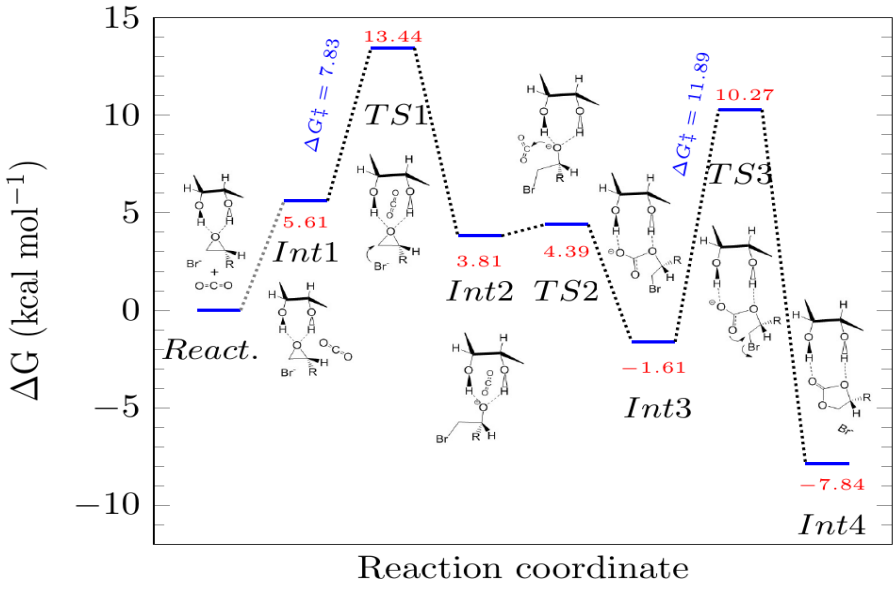

Figure 4 - 2. Gibbs free energy profile of the CtS/TBAB-catalyzed cycloaddition of CO_2 to PO. Only the active sites of the biopolymer (CtS) are represented in the models for clarity.

These interactions activate the epoxide and decrease the ring-opening energy barrier to 7.83 and 9.94 kcal mol^{-1} for CtS/TBAB and LiG/TBAB respectively, in comparison to that of the reaction catalyzed by TBAB (16.09 kcal mol^{-1}). An open-ring intermediate, Int2, is so formed.

Next step, the insertion of CO_2 to Int2 to form Int3, (Figure 4 - 2 and Figure 4 - 3) takes place with a very low barrier (0.58 and 2.57 kcal mol^{-1} for CtS/TBAB and LiG/TBAB respectively). The insertion occurs through a CO_2-adduct with the electron-rich alkoxide species (TS2, Figure 4 - 2 and Figure 4 - 3) that breaks the linearity of CO_2, given the gradual change of the C atom hybridization from sp to sp^2.

The O-C-O angle, ~161º at TS2, changes to ~129º at Int3 for both models. That makes CO_2 a C-electrophile leading to its insertion.[27] Concerted bromide leaving and ring-closing of the carbonate is the highest energy barrier step for the CtS/TBAB catalytic system ($\Delta G^{\#}$ = 11.89 kcal mol^{-1}).

Despite TS1 being more energetic than TS3, the height of the latter barrier is larger due to the stability of the precedent intermediate, Int3, relative to that on Int1. On the other hand, for the LiG/TBAB system the last barrier of the mechanism is comparable ($\Delta G^{\#}$ = 9.20 kcal mol^{-1}) to the barrier of the ring-opening step. For both catalysts the intermediate reached (Int4) is the most stable species of the profile (-7.84 and -12.82 kcal mol^{-1} for CtS/TBAB and LiG/TBAB respectively).

To close the catalytic cycle, the product must be released, substituted by a new substrate molecule (PO) that interacts with the active site. To model this step, another PO and CO_2 molecules should be included in the model, which makes the simulation unpractical.

The global comparison of the profiles obtained for the reaction catalyzed by the cellulose and lignin models indicates that the initial part of the reaction is very similar in both systems (from reactants to Int2). The energy changes (Figure 4 - 2 and Figure 4 - 3) as well as the geometry modifications are similar (Figure 4 - 4 and Figure 4 - 5). The average energy difference in this part of the reaction amounts less than 1 kcal mol^{-1}, and the main distances of the reactive species differ less than 0.05 Å between systems.

On the other hand, larger differences are found between the energies and geometries involved in the last step of the reaction. The average energy difference between the structures involved in this step (Int3, TS3 and Int4) is almost 4 kcal mol^{-1}. Regarding geometries, Int3 shows a non-negligible difference between systems: the $O_{CO2}\cdots C_{PO}$ distance is 0.4 Å larger in the cellulose system than in the lignin one.

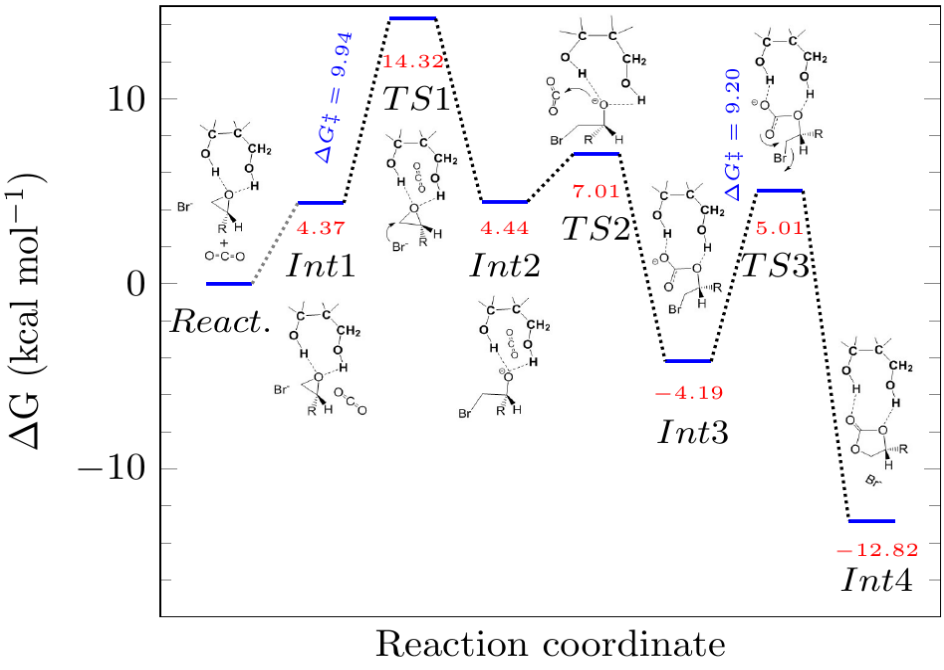

Figure 4 - 3. Gibbs free energy profile of the LiG/TBAB-catalyzed cycloaddition of CO_2 to PO. Only the active sites of the biopolymer (LiG) are represented in the models for clarity.

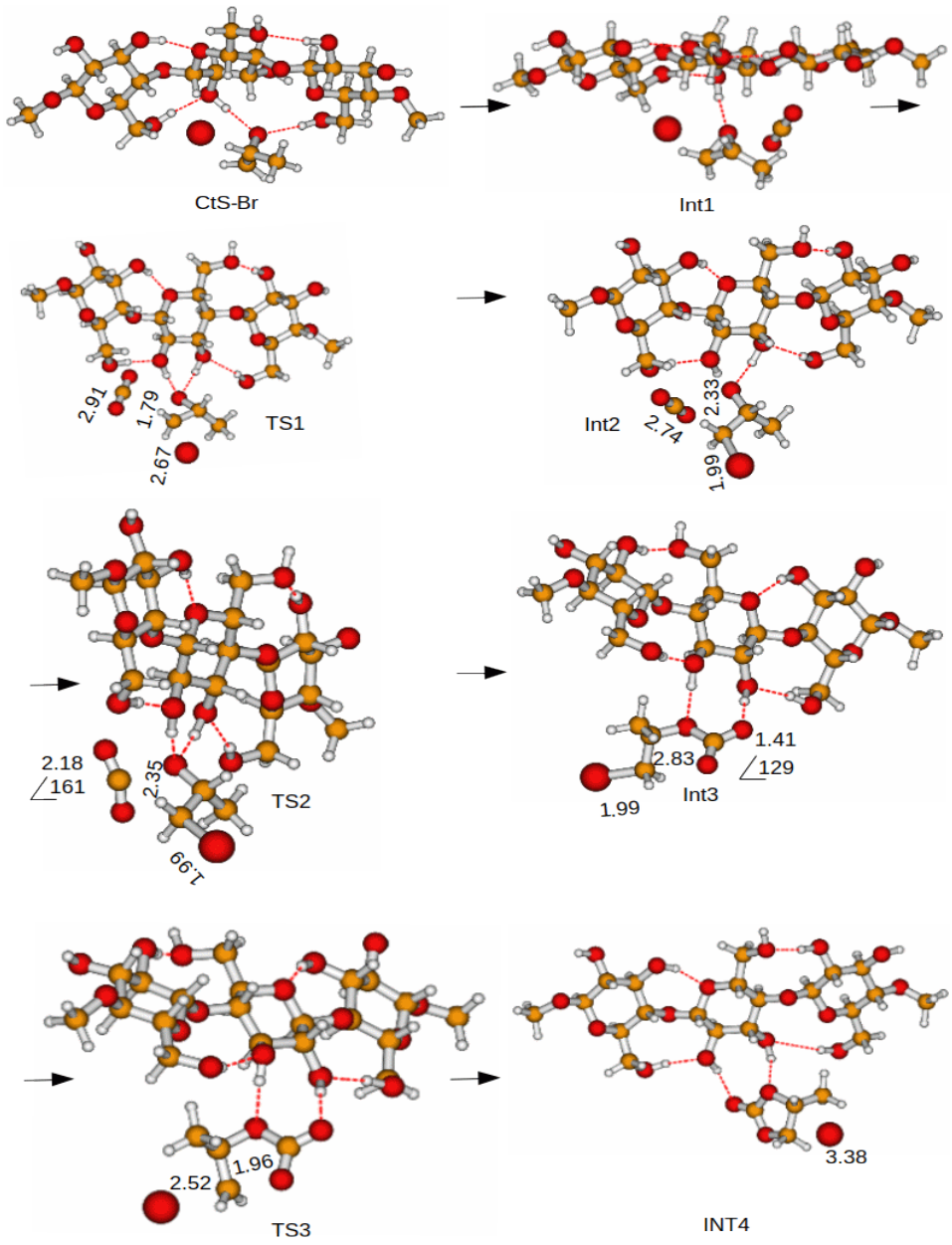

Figure 4 - 4. Geometries of the critical points located along the reaction path of the cycloaddition of CO_2 to propylene oxide using CtS/TBAB as catalyst. Distances in Å. The orientation of the catalyst has been changed in the different critical points to better show the reactant moiety of the system.

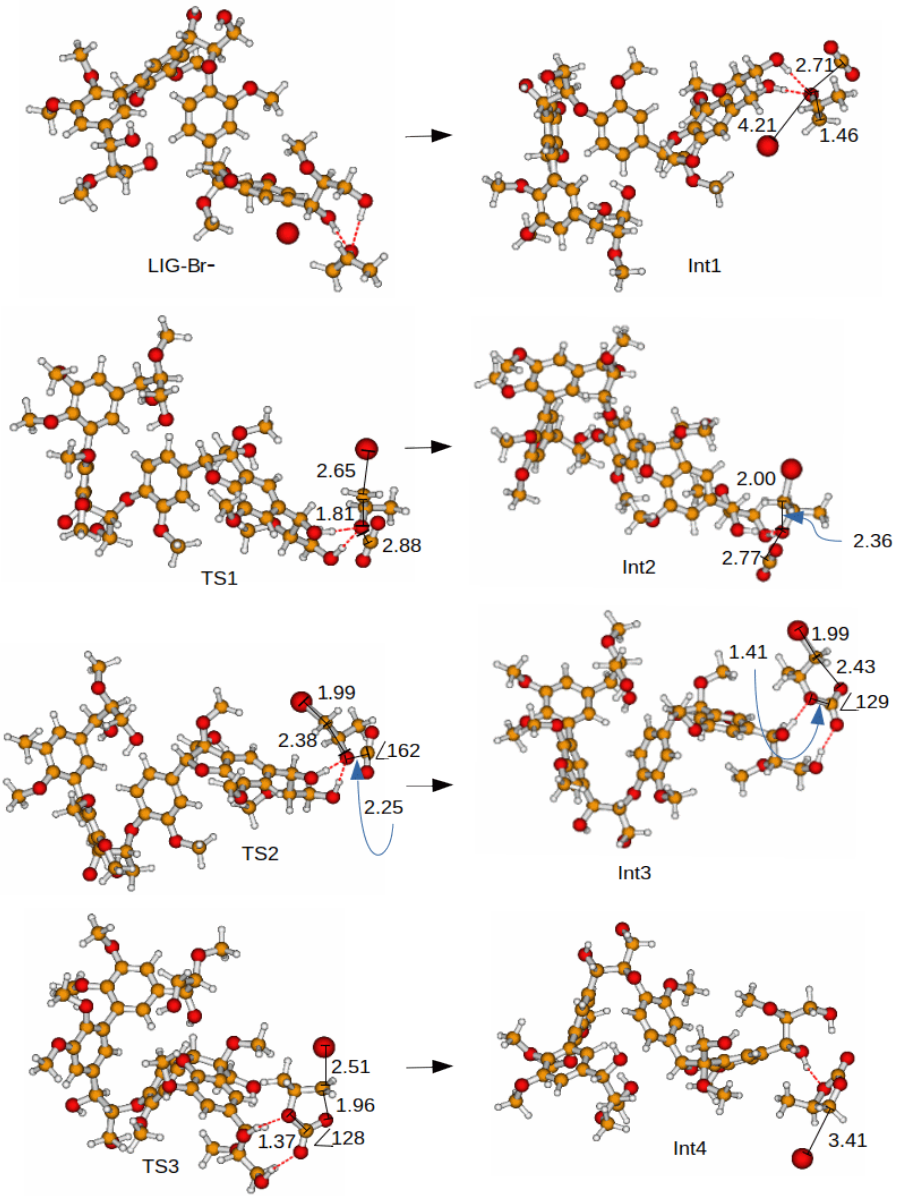

Figure 4 - 5. Geometries of the critical points located along the reaction path of the cycloaddition of CO_2 to propylene oxide using LiG/TBAB as a catalyst. Distances in Å. The orientation of the catalyst has been changed in the different critical points to better show the reactant moiety of the system.

This variation can be due to the nature of the H-bond interactions of the catalyst and substrate in the different parts of the reaction. In the initial species (from reactants to Int2), the two hydrogen bonds generated between the catalyst and the substrate are formed with only one oxygen atom, that of the epoxide. On the other hand, from Int3 to products, the two hydrogen bonds are established with two different oxygen atoms, making a more stable species when lignin is the catalyst. It seems to indicate that the 1,3-relative position of the hydroxyl groups in lignin is more adequate than the 1,2-relative position of these groups in cellulose to facilitate the ring closure of the cyclic carbonate.

4.3.4 Comparison of Experimental and Computational Results

Table 4 - 1 shows the %substrate conversion of TBAB, CtS/TBAB and LiG/TBAB catalyzed CO_2 cycloaddition to the substrate 1,2-epoxyhexane. This table also compares the activation energy barriers from mechanistic studies of the reactions. A correlation was found between the energy barriers and the catalytic activities of the reactions studied. Thus, the relative order of activation energies for the model catalytic systems TBAB > CtS/TBAB > LiG/TBAB agrees with the relative order of activity observed experimentally. Nevertheless, the conversions obtained with the residue's lignocellulose/TBAB are in the range of 47-79%.[4] These values indicate that not only the cellulosic and lignin fragments contribute to the

activity of the whole material but also that there can be a synergic catalytic effect due to the interaction between the biopolymers.

Table 4 - 1. Comparison of %conversion with the energy barriers calculated by DFT using different catalytic systems.

Catalytic system		Energy barrier (kcal mol^{-1})		%Conv[a]
Entry		Ring-opening	Ring-closing	
1	TBAB	**16.1**	10.9	47
2	CtS/TBAB	7.8	**11.9**	53
3	LiG/TBAB	**9.9**	9.2	72

[a] Reaction conditions: substrate 1,2-epoxyhexane: 2.4 g (0.024 mol), HC/AIL: 150 mg (6% w/w), TBAB: 0.112 mmol (0.47 mol%) respect to the substrate. T = 95 ^{o}C, t = 16 h, P = 10 bar CO_2. Conversion determined by ^{1}H NMR.

To sum up, the DFT study shows that the interaction of the -OH groups of the lignocellulosic materials with the reactant system is crucial for the activity of these catalysts. This interaction decreases the energy barrier for the ring-opening of the epoxide by Br^- and explains why the combination of the lignocellulosic wastes with TBAB gives place to a more active catalyst than TBAB alone in most cases. The interaction of CO_2 with the activated epoxide is the key point for the second step of the reaction. Like in the case of the H-bonds, this is a noncovalent interaction that could be described as a tretel bond, established between the C atom of CO_2, a region of positive electrostatic potential (σ-hole), and the negatively charged oxygen of the epoxide. This is another example of the crucial role that noncovalent interactions have in the mechanisms of catalyzed reactions, as pointed out lately by several authors.[28] Regarding the question about which component contributes more to the total activity,

although the lignin model in combination with TBAB has the lowest energy barrier and LiG/TBAB is a more active catalyst, other factors such as the diffusivity of the reactants in the solid materials or the interconnection of the lignocellulosic biopolymers in the specific waste may account for the final activity observed.

4.4 Conclusions

The mechanistic DFT studies together with the analysis of the holocellulose and lignin content of the materials led to the conclusion that the 1,2-diol of cellulose and 1,3- diol of lignin fragments activate epoxides by H-bonding. The -OH groups present in hollocellulose and lignin of lignocellulosic materials contribute to their activity as catalysts. The %substrate conversion by LiG/TBAB binary system was higher than that of CtS/TBAB system. Also, compared to the 1,2-diol based CtS/TBAB system, the 1,3-diol based LiG/TBAB system showed lower reaction energy barriers which corresponds to its higher substrate conversion capacity. Other factors such as the diffusivity of reactants or the interconnection of the lignocellulosic biopolymers may also contribute. Lignocellulosic biomasses of various origins in combination of nucleophiles can be used as a potential cooperative catalyst for the CO_2 cycloaddition reaction to different epoxides.

4.5 References

(1) Ozokwelu, D.; Zhang, S.; Okafor, O. C.; Cheng, W.; Litombe, N. Biomass Utilization. In *Novel Catalytic and Separation Processes Based on Ionic Liquids*; Elsevier: Amsterdam, 2017; pp 203–220.
(2) Carneiro, T. F.; Timko, M.; Prado, J. M.; Berni, M. Biomass Pretreatment With Carbon Dioxide. In *Biomass Fractionation Technologies for a Lignocellulosic Feedstock Based Biorefinery*; Elsevier: Amsterdam, 2016; pp 385–407.
(3) CLSF (Center for Lignocellulose Structure and Formation) Homepage http://www.cals.lignocellulose.org/index.html (accessed 2021 -01 -18).
(4) El Ouahabi, M. S.; Yeamin, M. B.; Rivas, R.; El Guemmout, F.; Reguero, M.; Masdeu-Bultó, A. M.; Aghmiz, A. *Cellulose* **2020**, *28,* 359-375.
(5) Watts, H. D. Application of Density Functional Theory Calculations to Elucidate the Structure of Lignin Linkages and the Intermolecular Interactions among Proxies of Lignin, Hemicellulose, and Cellulose. Ph.D. Thesis, The Pennsylvania State University, 2011.
(6) Yang, H.; Watts, H. D.; Gibilterra, V.; Weiss, T. B.; Petridis, L.; Cosgrove, D. J.; Kubicki, J. D. *Interdiscip. Sci. Comput. Life Sci.* **2019**, *11* (3), 485–495.
(7) Chung, H.; Washburn, N. R. *Green Mater.* **2013**, *1(3)*, 137.
(8) Chakar, F. S.; Ragauskas, A. J. *Ind. Crops Prod.* **2004**, *20* (2), 131–141.
(9) Martin-Martinez, F. J.; Dobado, J. A.; Sanchez-Gonzalez, A.; Barreiro, D. L.; Buehler, M. J. Multiscale Modeling of Lignocellulosic Biomass. In *Handbook of Materials Modeling: Applications: Current and Emerging Materials*; Springer International Publishing: Cham, 2018; pp 1–22.
(10) Liu, M.; Wang, X.; Jiang, Y.; Sun, J.; Arai, M. *Catal. Rev. - Sci. Eng.* **2019**, *61* (2), 214–269.
(11) Yingcharoen, P.; Kongtes, C.; Arayachukiat, S.; Suvarnapunya, K.; Vummaleti, S. V. C.; Wannakao, S.; Cavallo, L.; Poater, A.; D' Elia, V. *Adv Synth Catal* **2019**, *361* (2), 366–373.
(12) Liu, M.; Gao, K.; Liang, L.; Wang, F.; Shi, L.; Sheng, L.; Sun, J. *Phys. Chem. Chem. Phys.* **2015**, *17* (8), 5959–5965.
(13) Wang, J.-Q.; Sun, J.; Cheng, W.-G.; Dong, K.; Zhang, X.-P.; Zhang, S.-J. *Phys Chem Chem Phys* **2012**, *14* (31), 11021–11026.
(14) Whiteoak, C. J.; Nova, A.; Maseras, F.; Kleij, A. W. *ChemSusChem* **2012**, *5* (10), 2032–2038.
(15) Alves, M. Carbon Dioxide and Vegetable Oil for the Synthesis of Bio-Based Polymer Precursors. Ph.D. Thesis, Bordeaux; Université de Liège, 2016.
(16) Friedfeld, M. R.; Margulieux, G. W.; Schaefer, B. A.; Chirik, P. J. *J. Am. Chem. Soc.* **2014,** *136* (38), 13178.
(17) Schlaf, M.; Zhang, Z. C. *Reaction Pathways and Mechanisms in Thermocatalytic Biomass Conversion II*; Springer: Singapure, 2016.
(18) Hong, M.; Kim, Y.; Kim, H.; Cho, H. J.; Baik, M.-H.; Kim, Y. *J. Org. Chem.* **2018**, *83* (16), 9370–9380.
(19) Li, X.; Cheetham, A. K.; Jiang, J. *Mol. Catal.* **2019**, *463*, 37–44.

(20) Marenich, A. V.; Cramer, C. J.; Truhlar, D. G. *J. Phys. Chem. B* **2009**, *113* (18), 6378–6396.
(21) Bhanage, B. M.; Arai, M. *Transformation and Utilization of Carbon Dioxide*; Springer-Verlag: Heildelberg, 2014.
(22) Frisch, M. J.; Trucks, G. W.; H.B. Schlegel; G.E. Scuseria; M.A. Robb; J. R.Cheeseman; G. Scalmani; V. Barone; G.A. Petersson; H. Nakatsuji; X. Li; M. Caricato; A.V. Marenich; J. Bloino; B.G. Janesko; R. Gomperts; B. Mennucci; H.P. Hratchian; J.V. Ortiz; A.F. Izmaylov; J.L. Sonnenberg; D. Williams-Young; F. Ding; F. Lipparini; F. Egidi; J. Goings; B. Peng; A. Petrone; T. Henderson; D. Ranasinghe; V.G. Zakrzewski; J. Gao; N. Rega; G. Zheng; W. Liang; M. Hada; M. Ehara; K. Toyota; R. Fukuda; J. Hasegawa; M. Ishida; T. Nakajima; Y. Honda; O. Kitao; H. Nakai; T. Vreven; K.Throssell; J.A. Montgomery, Jr.; J.E. Peralta; F. Ogliaro; M.J. Bearpark; J.J. Heyd; E.N. Brothers; K.N. Kudin; V.N. Staroverov; T.A. Keith; R. Kobayashi; J. Normand; K. Raghavachari; A.P. Rendell; J.C. Burant; S.S. Iyengar; J. Tomasi; M. Cossi; J.M. Millam; M. Klene; C. Adamo; R. Cammi; J.W. Ochterski; R.L. Martin; K. Morokuma; O. Farkas; J.B. Foresman; D.J. Fox. Gaussian 16 Rev. B.01. 2016.
(23) Yu, J. L.; Zhang, S. Q.; Hong, X. *J. Am. Chem. Soc.* **2017**, *139* (21), 7224–7243.
(24) Watts, H. D.; Mohamed, M. N. A.; Kubicki, J. D. *Cellulose* **2014**, *21* (1), 53–70.
(25) Hu, T.; Sun, Y.; Ding, Y. *J. CO2 Util.* **2018**, *28* (October), 200–206.
(26) Foltran, S.; Mereau, R.; Tassaing, T. *Catal. Sci. Technol.* **2014**, *4* (6), 1585–1597.
(27) Aresta, M.; Dibenedetto, A.; Quaranta, E. The Carbon Dioxide Molecule. In *Reaction Mechanisms in Carbon Dioxide Conversion*; Springer: Berlin, 2016; pp 1–34.
(28) Mahmudov, K. T.; Gurbanov, A. V.; Guseinov, F. I.; Guedes da Silva, M. F. C. *Coord. Chem. Rev.* **2019**, *387*, 32–46.

CHAPTER 5:

CO_2 Cycloaddition by Zn-phen-N4 Complexes: Catalyst Development through Mechanistic Studies

5.1 Introduction

Many four-nitrogen (N4) containing heterocyclic donor ligands are found in nature. First, the heme group of haemoglobin consists of a N4 ligand known as porphyrin with an iron metal in the center. Another example is chlorophyll which has a reduced porphyrin ring attached to a central magnesium ion. A third appealing example would be Vitamin B_{12} which is based on a corrin ring, alike the porphyrin ring but with a cobalt metal ion in the center.

Due to its potential similarity with biological systems, synthesis of N4-ligands and their coordinating behavior with transition metal ions remains interesting.[1,2] Porphyrin complexes were synthesized with various metals in it, for example, Co-porphyrin[3] and Zn-porphyrin[4] complexes which are widely applied in CO_2 cycloaddition. Schiff base ligands also can lead to N4-donor based complexes[5] to study CO_2 cycloaddition.[6] Some terpyridine (terpy) ligand derived complexes[7] can act as N4-ligand system to apply in CO_2 cycloaddition.[8] Coordination

complexes based on this class of N4-ligands could also be used in CO_2 cycloaddition.

Incorporation of zinc into the N4-ligands is a very interesting option due to its abundance in the environment as well as in the human body.[2,9] Zinc may adopt different coordination with an N4 ligand. Karamé et al.[10] reported a ZnN4 complex with Schiff base where all four nitrogens participate in the complexation. Porpyrin forms a variety of Zn-porpyrin complexes.[4,11] There are five-coordinated distorted square pyramidal ZnN4 complexes leaving one nitrogen non-coordinated.[2,9,12] Also, among the bi-nuclear zinc complexes reported by Wang et al.[13], there is a five-coordinated zinc center associated with another four-coordinated zinc center. Therefore, overall structural features such as bond distances and angles should be studied to define the coordination number of a Zn-complex. The capacity of N4-ligands to adopt either tri- or tetra-dentate binding modes on coordination to Zn can also be studied by the relative energies of these coordination conformers from DFT calculations.[7] To confirm the reliability of these predictions, the calculated structures can be compared with their crystallographic counterparts to fully understand the factors that influence the binding mode of N4-ligands.

The phen ligand and its derivatives have extensively been used and still are used as versatile starting material in many branches of coordination chemistry.[14] It is a rigid, planar, hydrophobic, and electron-poor heteroaromatic ligand. Phen has two aromatic nitrogens whose unshared electron pairs are well-placed to co-operatively bind to metal ions. The π-electron deficiency makes phen a brilliant π-acceptor. Amine

derivatives of phen ligands are potential ligands containing both soft and hard sites and may extend into four nitrogen containing phen-N4 systems.[1,14] These phen-N4 ligands[12,9,14] may coordinate different metals such as cobalt, manganese, iron and zinc.

Zinc complexes of N4 ligands catalyze the CO_2 cycloaddition to epoxides with assistance of a nucleophilic co-catalyst, usually, tetrabutylammonium bromide (TBAB).[4,11,15] These ZnN4 catalyst/TBAB binary catalytic systems not only lower the activation barrier to promote the reaction kinetics but also might impart stereoselectivity and regioselectivity of substrate epoxides.[16,17] Different catalysts lead to different reaction path and the reactive conformer of a catalyst directs that path. A detail understanding on the catalytic activity essentially considers the electronic structure of the ZnN4 catalyst and how it interacts with the reactant CO_2 and substrate epoxide. A thorough mechanistic study of the reaction would elucidate the reactive intermediates and transition states all the way to catalytic CO_2 conversion into the product cyclic carbonate.[10,11,18]

Herein, we studied the electronic structure of a series of previously synthesized Zn complexes of phen-N4 ligands (Scheme 5 - 1). Coordination modes of these phen-N4 ligands to central zinc ion were confirmed by comparing the most stable conformer obtained from the computational study with the x-ray structure obtained experimentally. The experimental catalytic activity of Zn complexes was optimized for the CO_2 cycloaddition reaction to epoxides. The substrate scope of the catalysis was considered in two broader categories of mono-substituted

alkyl and aryl epoxides. Finally, the computational mechanistic study unfolds the detail functions of each catalytic component.

5.2 Computational Models and Catalytic Experiments

5.2.1 Computational Models

The geometry optimizations and frequency calculations were carried out using the DFT method as implemented in Gaussian 16. The CAM-B3LYP functional was chosen for the study of CO_2 cycloaddition catalyzed by Zinc complexes. The D3BJ version of Grimme's empirical dispersion was added to the model to correct the basis set superposition error (BSSE) among the reaction moieties. As explained in Table 5A – 1 of Appendix, this correction was necessary to obtain reliable energies of the complexes.

An exploratory study was performed to determine the most appropriate basis set (section 5.A in Appendix) that provides a balance between accuracy of results and computational cost. In conformational analysis, the relatively cheaper basis set 6-311+G(2df,p), LanL2DZ(Zn) was found sufficient to reproduce the accurate energies found with expensive aug-cc-pVDZ and even more expensive aug-cc-pVTZ basis sets whereas cheapest basis set 6-31+G(d,p), LanL2DZ(Zn) was found unreliable.

The specification of the theoretical model used comprises two parts, separated by "/" i.e., type of calculation/basis set. If this is the complete designation, then this means that full optimization of the equilibrium geometry (or transition-state geometry) was done using the same type of calculation and basis set. If, however, the designation is followed by a "//" and then specification of a second "type of calculation/basis set", then this means that the calculation was preceded by equilibrium geometry (or transition-state geometry) optimization using this second type of calculation and basis set, i.e.,

$$"type\ of\ calculation/basis\ set"^{(for\ energy)}//"type\ of\ calculation/basis\ set"^{(for\ geometry)}$$

Mechanistic studies of the smaller system studied were performed with CAM-B3LYP-D3BJ/aug-cc-pVDZ,6-311+G(2df,p)(Br/Cl),SMD//CAM-B3LYP-D3BJ/aug-cc-pVDZ,6-311+G(2df,p)(Br/Cl),SMD calculations, while for the larger catalytic system, calculations were done at CAM-B3LYP-D3BJ/aug-cc-pVDZ,6-311+G(2df,p)(Br/Cl),SMD//CAM - B3LYP-D3BJ/6 31+G(d,p),LanL2DZ(Zn/Br/Cl),SMD.

The Solvation Model Based on Density (SMD) was used to describe the reaction media as a polarizable continuum (like in section 4.2.2, Chapter 4). Gibbs free energy (ΔG) and free energy of activation (ΔG‡) were also calculated as described in section 4.2.2.

5.2.2 Catalytic Experiments

Catalyst Zn-phen-N4iPr[19] was collected from a different study in the group. Substrates 1,2-epoxyhexane (EPH), propylene oxide (PO), styrene oxide (SO), and epichlorohydrin (ECH) were from Sigma Aldrich. TBAB was used as co-catalyst. CO_2 gas cylinders (99.99% pure) were purchased from Linde, Germany. ^{1}H NMR were recorded in a Varian spectrometer at room temperature in $CDCl_3$.

The catalytic experiments were caried out in a 25 mL Parr reactor. Reactions were set at 950 rpm (rotations per minute) stirring. After the reaction time, the autoclave was cooled in ice bath until room temperature, and the pressure released. Then, the autoclave was opened, and the content was analyzed by ^{1}H NMR spectroscopy using mesitylene as internal standard. ^{1}H NMR were recorded in a Varian spectrometer at room temperature in $CDCl_3$. Chemical shifts were reported in parts per million (ppm, δ). The %conversion was determined from ^{1}H NMR of the crude mixture from the integral ratio of the produced cyclic carbonate and individual substate fed.

5.3 Locating the Lowest-Energy Zn-phen-N4R Model Conformers

Zn-phen-N4R complexes were prepared in a previous work.[19] Scheme 5 - 1 summarizes the synthesis of aniline derivatives of phen-N4

ligands.[20] These extended phen-N4 systems with alkyl (-R) substituents in the aniline rings are abbreviated as phen-N4R, where R = H/Et/iPr. Ligand phen-N4Et, 2,9-bis(imino)-1,10-phenanthrolinebis-(2,6-diethylanilina), was synthesized from a reaction of the precursor 1,10-phenanthroline-2,9-dicarbaldehide with a reagent 2,6-diethylaniline whereas reaction of 2,6-diisopropylaniline reagent with the same precursor produced the ligand phen-N4iPr, 2,9-bis(imino)-1,10-phenanthrolinebis-(2,6-diisopropilanilina).

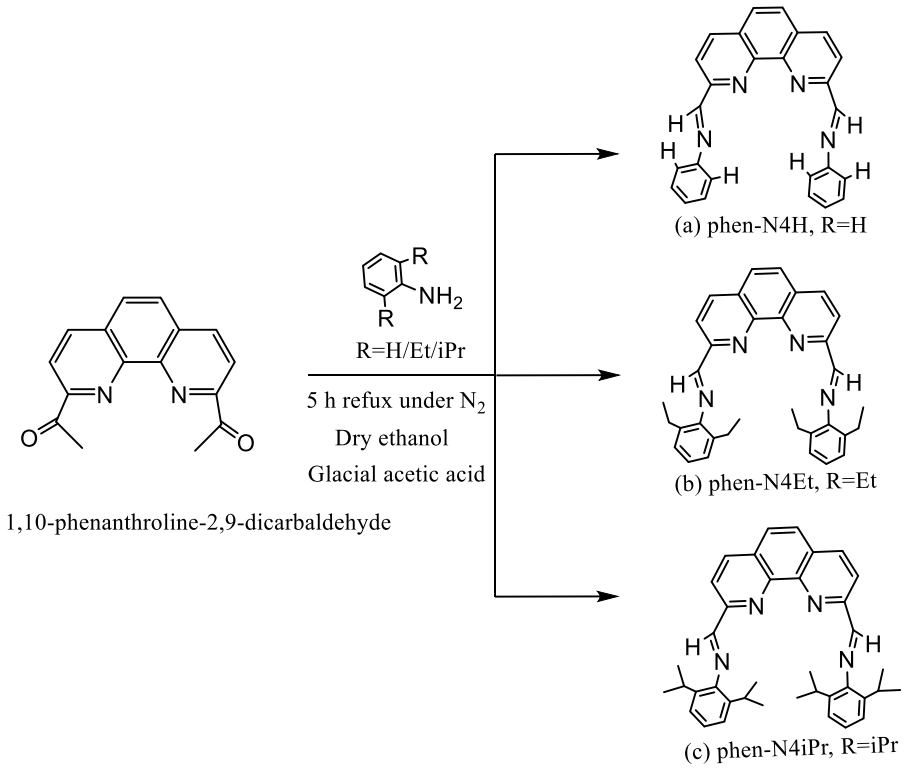

Scheme 5 - 1. Synthesis of phen-N4R ligands. (a) phen-N4H (a model ligand; no record of synthesis), (b) phen-N4Et and (c) phen-N4iPr ligand.

Reaction of phen-N4iPr with the zinc salt, $ZnCl_2$ produced Zn-phen-N4iPr complex shown in Scheme 5 - 2. The X-ray diffraction crystal structure[19] of Zn-phen-N4iPr is shown in Figure 5 - 1. It shows a pentacoordinate geometry with the ligand acting as tridentate and two chlorides occupying the rest of the coordination positions.

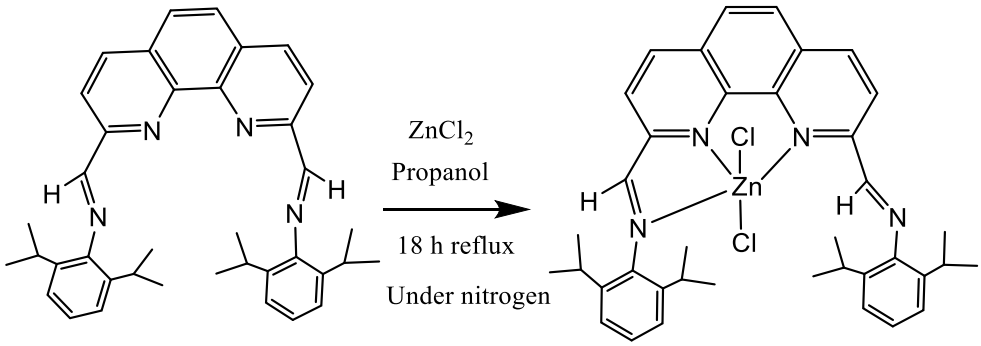

Scheme 5 - 2. Synthesis of Zn-phen-N4iPr complex.

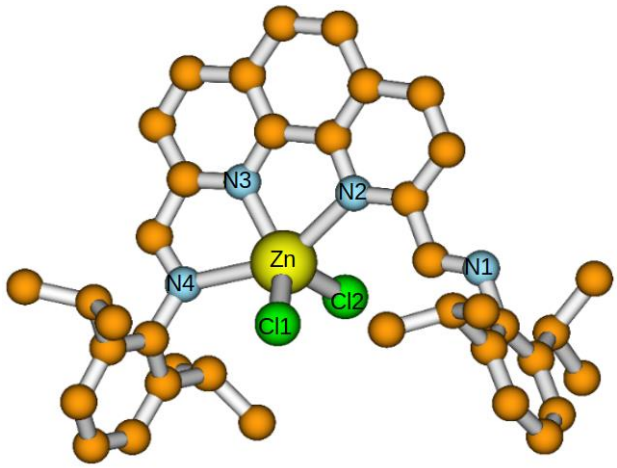

Figure 5 - 1. X-ray diffraction structure of Zn-phen-N4iPr. All hydrogen atoms and solvent molecules are omitted for clarity.

To identify the most stable structures, we performed DFT calculations of the R = H, Et and iPr derivatives of aniline to check if the model fits with the observed X-ray structure. Possible effect of alkyl substituents of aryl moieties on the stability of the complexes was also investigated.

The number of nitrogens from phen-N4R ligand that coordinate to the cationic Zn (II) center determines the structural geometry of a Zn-complex. Moreover, the spatial arrangement of imine and aryl moieties is another structural feature for the Zn-phen-N4R complexes. From a model perspective, the spatial relative disposition of the CH = NAr units imposes a given position of the N with respect to the central Zn atom. This leads to a short or long Zn-N distance that allow or not the formation of a Zn-N bond. In this way, the isomerism of CH = NAr double bond becomes an indicator for the coordination number (CN) of central Zn (II) cation. Scheme 5 - 3 shows the possible isomers of Zn-phen-N4R complexes with CN 6, 5 and 4. In the six-coordinated Zn-phen-N4R complex, the hydrogens of both imine CH = NAr units remain outside the double bond and is labeled as *exo-exo* configuration, see Scheme 5 - 3(a). On the other hand, as shown in Scheme 5 - 3(b), in the five-coordinated Zn-phen-N4R complex, the hydrogen of one of the imine CH = NAr unit points towards inside the double bond and is labeled as *exo-endo* configuration. Finally, Scheme 5 - 3(c) shows the four-coordinated complex where both imino

hydrogens remain inside the double bond providing the so-called *endo-endo* configuration.

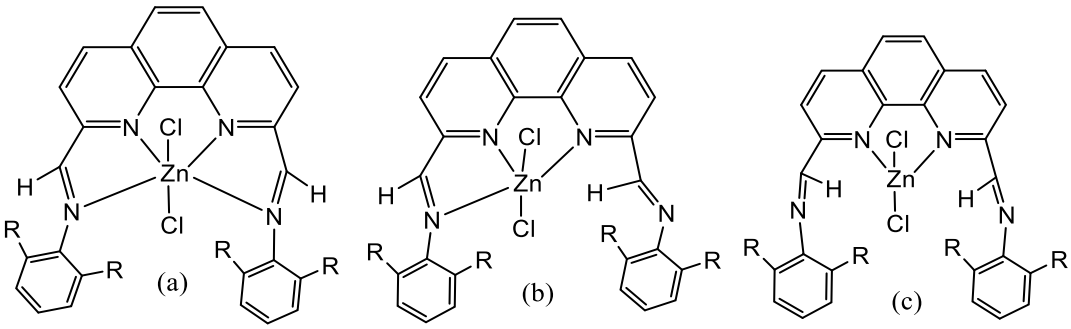

Scheme 5 - 3. (a) Six-coordinated Zn-phen-N4R*exo-exo*, (b) five-coordinated Zn-phen-N4R*exo-endo* and (c) four-coordinated Zn-phen-N4R*endo-endo* complexes where R = H/Et/iPr.

Three possible substituent -R groups have been considered in the phen-N4R ligand. Applying R = H/Et/iPr notation, we will consider the corresponding six-coordinated (*exo-exo*), five-coordinated (*exo-endo*), and four-coordinated (*endo-endo*) complexes. Furthermore, the relative disposition of the aniline groups gives place to different conformations. Following the convention of electrocyclic reactions[1], when both terminal aryl groups have conrotatory motions, they are named Zn-phen-N4R$_{con}$ complexes whereas aryl groups in the disrotatory motions are called Zn-phen-N4R$_{dis}$ isomers. We aim to find the lowest energy geometries from all these isomers. Figure 5 - 2 and Figure 5 - 3, respectively, shows the possible conrotatory and disrotatory isomers of six-, five-, and four-coordinated Zn-phen-N4H model complexes. For R = H, initial

exploratory calculations were performed at CAM-B3LYP-D3BJ/6-31+G(d,p), LanL2DZ(Zn)/SMD level. The conrotatory complexes of Figure 5 - 2 are marginally more stable than their disrotatory counterparts of Figure 5 - 3, with the exception of six-coordinated Zn-phen-N4H*exo (*more at Table 5A – 1, Appendix*)*.

The systematic study of the effect of the basis set on Zn-phen-N4H$_{con}$ complexes (Appendix 5.A) shows that at CAM-B3LYP-D3BJ/aug-cc-pVTZ//CAM-B3LYP-D3BJ/aug-cc-pVTZ level, the five-coordinated Zn-phen-N4H$_{con}$ is the most stable Zn-phen-N4H complex. Therefore, five-coordinated Zn-phen-N4H$_{con}$ structure is used as the initial catalyst structure for the mechanistic study of CO_2 cycloaddition to epoxides. Given that the same relative energies are obtained with the smaller basis set aug-cc-pVDZ,6-311+G(2df,p)(Br/Cl),SMD, this will be the one used for the subsequent mechanistic study for the Zn-phen-N4H$_{con}$ complex catalyzed reaction.

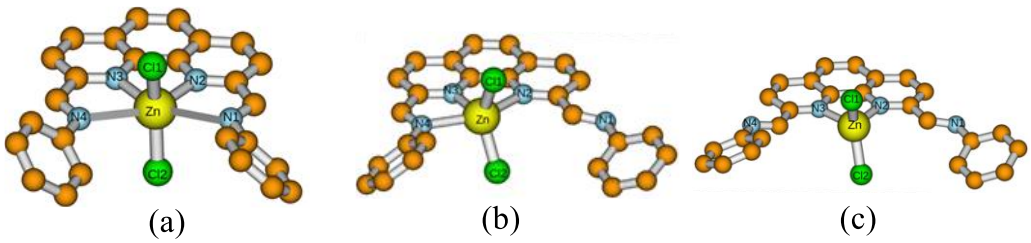

Figure 5 - 2. Optimized geometry of conrotatory (a) six-, (b) five- and (c) four-coordinated Zn-phen-N4H complexes. Nitrogens are counted anti-clockwise.

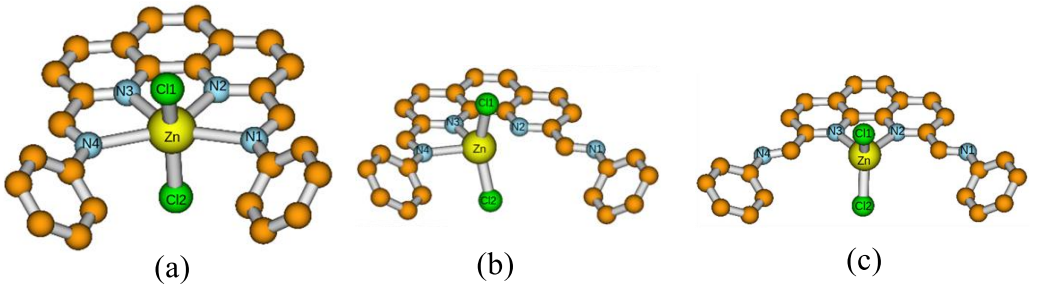

Figure 5 - 3. Optimized geometry of disrotatory (a) six-, (b) five- and (c) four-coordinated Zn-phen-N4H complexes. Nitrogens are counted anti-clockwise.

Unlike Zn-phen-N4H complexes, during the geometry optimization of Zn-phen-N4iPr complexes, the conrotatory and disrotatory isomers became almost indistinguishable, probably due to the steric repulsion generated by the iPr substituents. Zn-phen-N4iPr$_{con}$ is more stable than Zn-phen-N4iPr$_{dis}$ (see Figure 5 - 4) only by less than 0.5 kcal mol^{-1} calculated at CAM-B3LYP-D3BJ/6-31+G(d,p),LanL2DZ(Zn)/SMD. The distance parameters (see Table 5A – 6, in Appendix) of both structures are also found to be very similar.

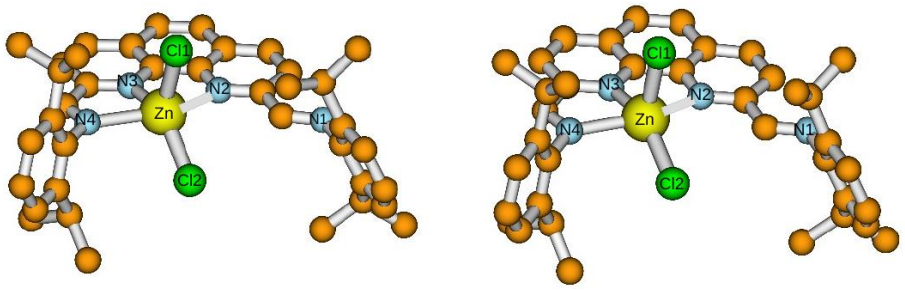

Figure 5 - 4. Optimized geometry of five-coordinated (a) Zn-phen-N4iPr$_{con}$ and (b) Zn-phen-N4iPr$_{dis}$ complex. Nitrogens are counted anti-clockwise.

The conformational energy of five-coordinated Zn-phen-N4iPr and four-coordinated Zn-phen-N4iPr are respectively 4.54 kcal mol^{-1} and 4.16 kcal mol^{-1} more stable than that of six-coordinated Zn-phen-N4iPr, revealing that, like for R = H, the five-coordinated Zn-phen-N4iPr is the most stable complex. This five-coordinated Zn-phen-N4iPr structure is then compared with that of the experimentally determined x-ray structure, shown in Figure 5 - 5. Moreover, Table 5 - 1 presents the percent error (PE) of the geometrical parameters of the Zn-phen-N4iPr model complex with those obtained from the X-ray diffraction spectra of the synthesized complex in our group. The PE of coordination bond lengths of the model was not more than 2% with exception to the Zn-N2 bond (3.75%). The PE in the bond angles Cl1-Zn-N3 and Cl2-Zn-N3 was higher to 22% and 15%, respectively. Overall, such PE values for bond lengths and bond angles reflects that the model parameters are not quite away from their experimental XRD values. This model structure is used as a catalyst for the elucidation of the reaction mechanism of CO_2 cycloaddition to epoxides.

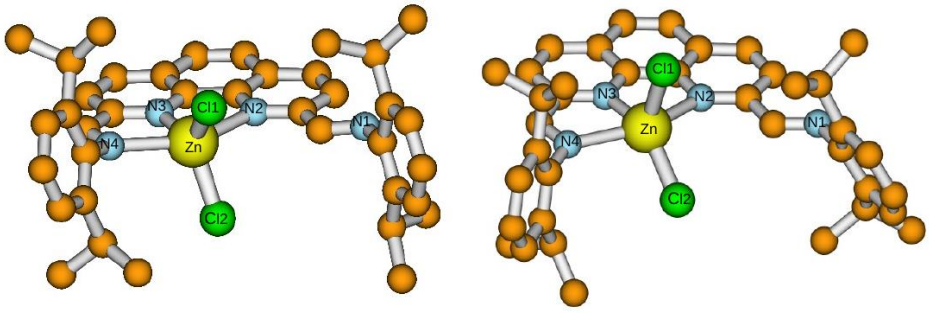

Figure 5 - 5. Comparing X-ray diffraction structure of Zn-phen-N4iPr (left panel) with the five-coordinated Zn-phen-N4iPr obtained computationally (right panel). Nitrogens are counted anti-clockwise.

Table 5 - 1. Comparison of the coordination bond lengths (Å) and bond angles (°) of model Zn-phen-N4iPr with that of x-ray structure and percent error (PE).

Length (Å)			PE	Angle (°)			PE
	XRD	Model	(%)		XRD	Model	(%)
Zn-Cl1	2.229	2.275	2.00	Cl1-Zn-Cl2	112.98	115.51	2.19
Zn-Cl2	2.244	2.290	2.01	Cl1-Zn-N3	129.83	106.24	22.20
Zn-N3	2.052	2.084	1.55	Cl2-Zn-N3	117.18	138.23	15.22
Zn-N2	2.308	2.398	3.75	Cl1-Zn-N2	101.69	94.34	7.79
Zn-N4	2.349	2.364	0.64	Cl1-Zn-N4	92.91	99.89	6.98
Zn-N1	4.814	4.891	1.57	Cl2-Zn-N2	94.12	101.92	7.65
				Cl2-Zn-N4	105.52	97.89	7.79
				N2-Zn-N3	75.13	74.03	1.48
				N2-Zn-N4	148.67	147.62	0.71
				N3-Zn-N4	74.22	74.11	0.15

5.4 Catalytic Screening of Zn-phen-N4iPr/TBAB-Catalyzed CO_2 Cycloaddition

To find an optimal reaction condition of CO_2 cycloaddition into cyclic carbonate, catalyzed by Zn-phen-N4R systems, a thorough experimental catalytic screening was carried out with different catalyst/co-catalyst ratios along with a temperature change from 80 ^oC to 60 ^oC, a pressure drop from 30 bar to 10 bar, and with an associated time contraction from 6h to 3h. The results in Table 5 - 3 show different reaction conditions for the CO_2 coupling to the chosen benchmark substrate 1,2-epoxyhexane (EPH).

As shown in Table 5 - 2, when the catalyst/co-catalyst ratio increases from 0.13/0.1 (entry 1) to 0.13/0.2 (entry 2), the catalytic conversion rises from 72% to 100% at 80 ^oC, 30 bar and 6h. Under these conditions, the average was 208 h^{-1} after 3h (entry 3, Table 5 - 2). Nevertheless, to have an initial TOF at low conversion, we further reduce the reaction time to 1h which gives a TOF of 459 h^{-1} (entry 4, Table 5 - 2). Increasing the catalyst/co-catalyst loading increases from 0.13/0.2 to 0.13/0.5, and the conversion lifts from 82% to 96% (entry 3 vs. entry 5, Table 5 - 2). Then, to see the temperature effect, going from entry 5 to entry 6, we decrease the temperature from 80 ^oC to 60 ^oC while the time duration increases from 3h to 6h, yet the reaction ends with a decrease of conversion from 96% to 90% (entry 5 vs. entry 6, Table 5 - 2).

A pressure drop from 30 bar to 10 bar decreases the conversion only by 6% from 90% to 84% (entry 6 vs. entry 7, Table 5 - 2). The conversion

using only TBAB is lower of 26% (entry 8, Table 5 - 2). Finally, decreasing the time from 6h to 3h decreases the conversion from 84% to 60% (entry 7 vs. entry 9, Table 5 - 2). It is important to note that the reference of all the entries, TBAB alone, showed quite low conversion of a range of 15 – 26% as shown in Table 5B – 1 of the Appendix.

Table 5 - 2. Screening conditions of CO_2 cycloaddition to the substate 1,2 epoxyhexane to produce cyclic carbonate catalyzed by Zn-phen-N4iPr/TBAB system.

Entry	Cat/Co-cat (mol %)	T (°C)	P (bar)	t (h)	Conv[a] (%)	TOF[b] (h^{-1})
1	0.13/0.1	80	30	6	72	93
2	0.13/0.2	80	30	6	100	128
3	0.13/0.2	80	30	3	82	208
4	0.13/0.2	80	10	1	30	459
5	0.13/0.5	80	30	3	96	246
6	0.13/0.5	60	30	6	90	115
7	0.13/0.5	60	10	6	84	107
8	-/0.5	60	10	6	26	-
9	0.13/0.5	60	10	3	60	153

[a] Averaged conversion determined by ^{1}H NMR with mesitylene as internal standard; [b]Averaged TOF in mole substrate converted as $(mol.catalyst)^{-1}.h^{-1}$.

Considering all the involved parameters, 80 °C and 10 bars were chosen as the optimal condition of this catalytic transformation. These conditions have relatively low co-catalyst loading (0.2 mol%) with a short

time of 3h at a relatively low pressure of 10 bar although it works at relatively high temperature of 80 ^{o}C.

Then, to see the substrate scope, four different substrates (see Figure 5 - 6) were examined for CO_2 cycloaddition at the chosen optimal reaction conditions of 0.13/0.2 mol% cat/co-cat ratio at 80 ^{o}C, 10 bar, and in 3h. The results are shown in Table 5 - 3. Comparing entries 1 and 3 of Table 5 - 3, one can see that the conversion of the experimental benchmark substrate 1,2-epoxyhexane (EPH) is about 82%, which is similar to that of the propylene oxide (PO), the computational benchmark substrate. Nevertheless, the %conversion with TBAB alone is again about 20% for both EPH and PO, as shown in the comparison of entry 2 and entry 4 of Table 5 - 3.

On the other hand, entry 5 of Table 5 - 3 shows that styrene oxide (SO), with TBAB alone, gives a higher %conversion of 40% which is already 20% more than the corresponding %conversion of EPH and PO. Moreover, as shown in entry 7 of the Table 5 - 3, substrate epichlorohydrin (ECH) has even higher %conversion of 50% with TBAB alone. However, total %conversion due to the catalysis by Zn-phen-N4iPr/TBAB is 62% for SO (see entry 6) and 69% for ECH. ECH shows ahigher TOF of 231 h^{-1} whereas SO shows the lowest TOF of 205 h^{-1} among all four substates.

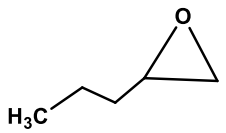

(a) 1,2-Epoxyhexane (EPH)

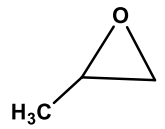

(b) Propylene oxide (PO)

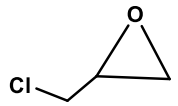

(d) Epichlorohydrin (ECH)

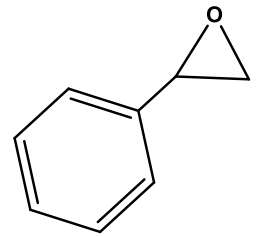

(c) Styrene oxide (SO)

Figure 5 - 6. Substrates used in Zn-phen-N4iPr/TBAB catalyzed CO_2 cycloaddition.

Table 5 - 3. Substrate scope of 0.13/0.2 mol% Zn-phen-N4iPr/TBAB catalyzed CO_2 cycloaddition to cyclic carbonate.¶

Entry	Sub.	Cat/Co-cat (mol %)	Conv[a] (%)
1	EPH	0.13/0.2	82
2	EPH	-/0.2	20
3	PO	0.13/0.2	82
4	PO	-/0.2	19
5	SO	0.13/0.2	62
6	SO	-/0.2	40
7	ECH	0.13/0.2	69
8	ECH	-/0.2	50

¶ Reaction conditions: 80 ^{o}C, 10 bar, and 3h.

[a] Averaged conversion determined by ^{1}H NMR with mesitylene as internal standard.

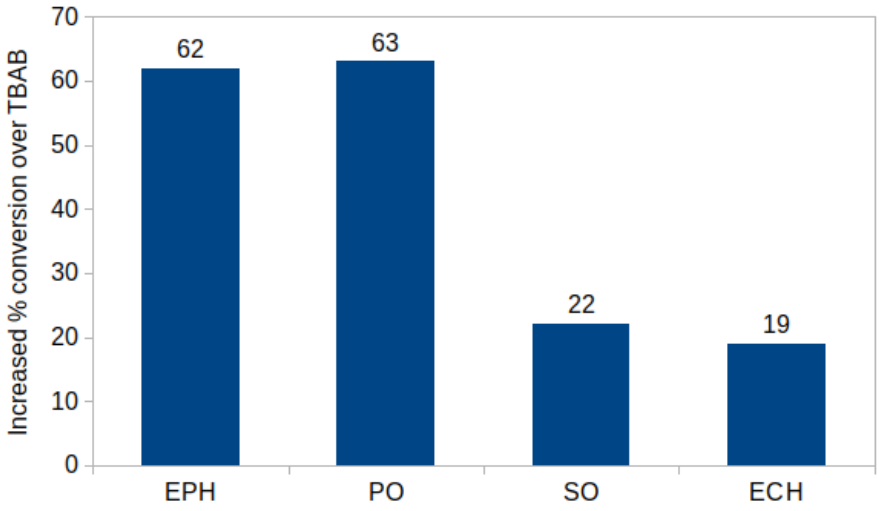

Figure 5 - 7. Increment of %conversion of different substrates due to Zn-phen-N4iPr catalyst relative to the conversion of the reaction using only the co-catalyst, TBAB. Reaction conditions: 80 °C, 10 bar and 3h.

5.5 Mechanistic Studies and Catalytic Development

Fundamental mechanistic steps[18] of a metal complex based cooperative CO_2 cycloaddition catalysis of an epoxide into cyclic carbonate are shown in Scheme 5 - 4. First, an epoxide coordinates to a Lewis acid catalyst followed by an attack by a nucleophile (co-catalyst). This nucleophilic attack opens the epoxide ring yielding a metal-bound alkoxide. The produced alkoxide then can act as a nucleophile and inserts a CO_2 electrophile into its metal alkoxide bond which results into a metal

carbonate intermediate. Finally, an intra-molecular rearrangement leads to the product, cyclic carbonate.

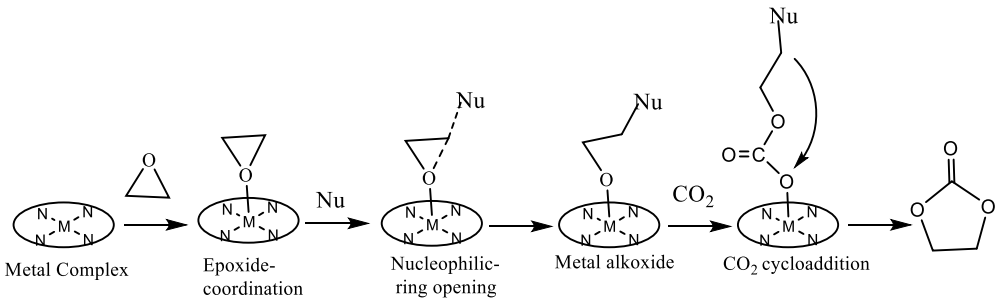

Scheme 5 - 4. Basic mechanistic steps of cooperative catalyst/co-catalyst-based CO_2 cycloaddition to epoxides.

However, the rate of reaction and selectivity towards a product (cyclic carbonate or polymeric carbonate) does not depend only on the catalyst's features but also depends on the nature of the epoxide substrate. For instance, cyclohexene oxide is more prone to form polycarbonate rather than cyclic carbonate due to the strain in forming cyclic carbonate.[18] On the other hand, epoxides with electron-withdrawing groups such as PO, SO, and ECH have the tendency of producing cyclic carbonate. Both steric and electronic effects of the substrates are important factors to govern the selectivity of a product.

From a regiochemical standpoint, the nucleophilic attack may take place either at the less sterically hindered carbon atom of the epoxide ring, i.e., at C_b or at the more hindered C_a. Scheme 5 - 5 shows the difference in the nucleophilic attacking position of PO and SO. In PO, the nucleophilic attack predominately occurs at less steric C_b. On the contrary, in SO, due

to the electron-withdrawing inductive effect of the phenyl group, the attack takes place at the stereoselective C_a.[16,18]

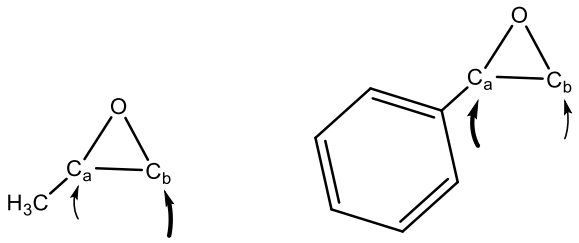

(a) Propylene oxide (PO) (b) Styrene oxide (SO)

Scheme 5 - 5. Difference in most probable (in bold) nucleophilic ring-opening of PO vs. SO.

5.5.1 Mechanistic Studies of Zn-phen-N4iPr/TBAB-Catalyzed CO_2 Cycloaddition to PO and SO

To provide insights into the species involved in the rate- and selectivity-determining steps of the catalytic cycle, a systematic computational study of structures and mechanisms is carried out. Scheme 5 - 6 shows the initial chemical constituents of the model reaction. As can be seen, the reactant system contains the catalyst, Zn-phen-N4iPr, a bromide anion (representing the co-catalyst, TBAB), the model substrate PO already coordinated to the catalyst, and a non-interacting CO_2 molecule. This model tries to reproduce the experimental conditions, where PO acts also as the solvent of the catalysts while CO_2 is added afterwards. The insertion of CO_2 into the system leads to the structure

labelled as Int1, where the weak interaction of CO_2 with the epoxide slightly increases the Gibbs free energy by 2.56 kcal mol^{-1}.

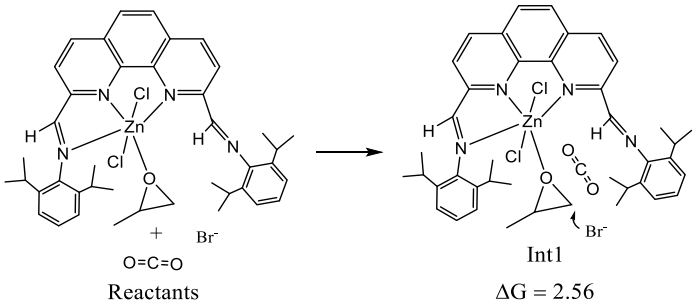

Scheme 5 - 6. Initial stage of the Zn-phen-N4iPr/TBAB-catalyzed CO_2 cycloaddition reaction. Gibbs free energy change is shown in kcal mol^{-1}.

From Int1 on, two different paths are explored: the α-path and the β-path. The α-path, following a concerted mechanism, leads to the product cyclic carbonate, without any change in the catalyst structure. However, in the β-path, a structural change in the catalyst takes place; the dissociation of an axial chlorido ligand. The reaction profile of the complete mechanistic study, including paths α and β, is summarized in Figure 5 - 8.

Going from Int1 to Int2α along the α-path, at the transition structure, the nucleophile Br^- attacks the less-hindered carbon, C_b of PO while the epoxide ring is opening (more in the discussion of Scheme 5 - 5). Then, in the step from Int2α to Int3α, the CO_2 gets inserted into the opened epoxide.

Finally, in the step from Int3α to the product, a cyclization of the produced alkoxide takes place, so a five membered ring is formed while the nucleophile is released. At the same time, the reactive part gets dissociated from the catalyst center in a concerted manner. Scheme 5 - 7 shows the structural details of all the critical species (intermediates and transition states) of these elementary steps.

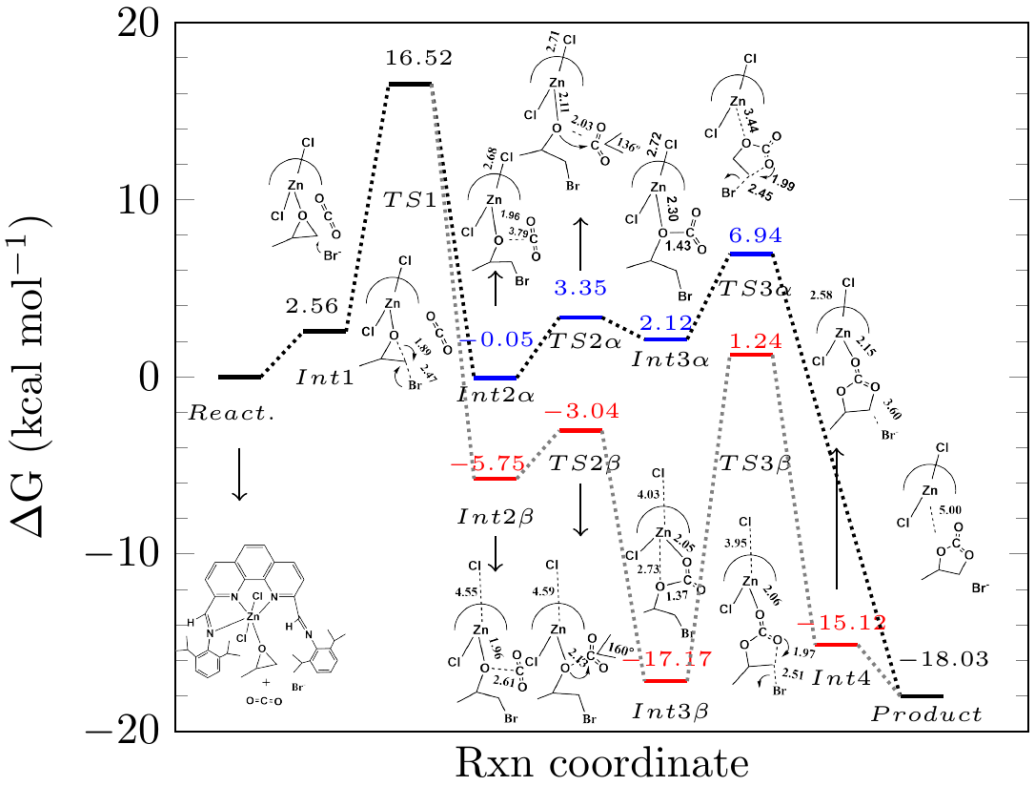

Figure 5 - 8. Gibbs free energy profile of Zn-phen-N4iPr/TBAB-catalyzed CO_2 cycloaddition to PO.

Following the β-path in the first step (going from Int1 to Int2β), unlike in the α-path, an axial chlorido ligand dissociates. Then, in the next step, the Int3β is reached from Int2β through the TS2β, similar to TS2α. After that, in the step going from Int3β to Int4β, a cyclization of the reactive part takes place but, unlike in the α-path, here the reactive part keeps coordinated to the Zn-center. Scheme 5 - 8 shows the structural details of all the critical species of the elementary steps of this path.

The activation energy barriers of the characteristic steps of the mechanisms are tabulated in Table 5 - 4. These data show that the epoxide ring opening, common for both paths, is the rate-limiting step of the Zn-phen-N4iPr/TBAB-catalyzed cycloaddition of CO_2 to PO and surprisingly the α-path largely facilitates the cyclization over the β-path by a 13.59 kcal mol^{-1} due to the high energy of the cyclization step along the latter path. Nevertheless, it must be pointed out that it is possible that an alternative path for this last step along the β-path exists, although it has been located up to now.

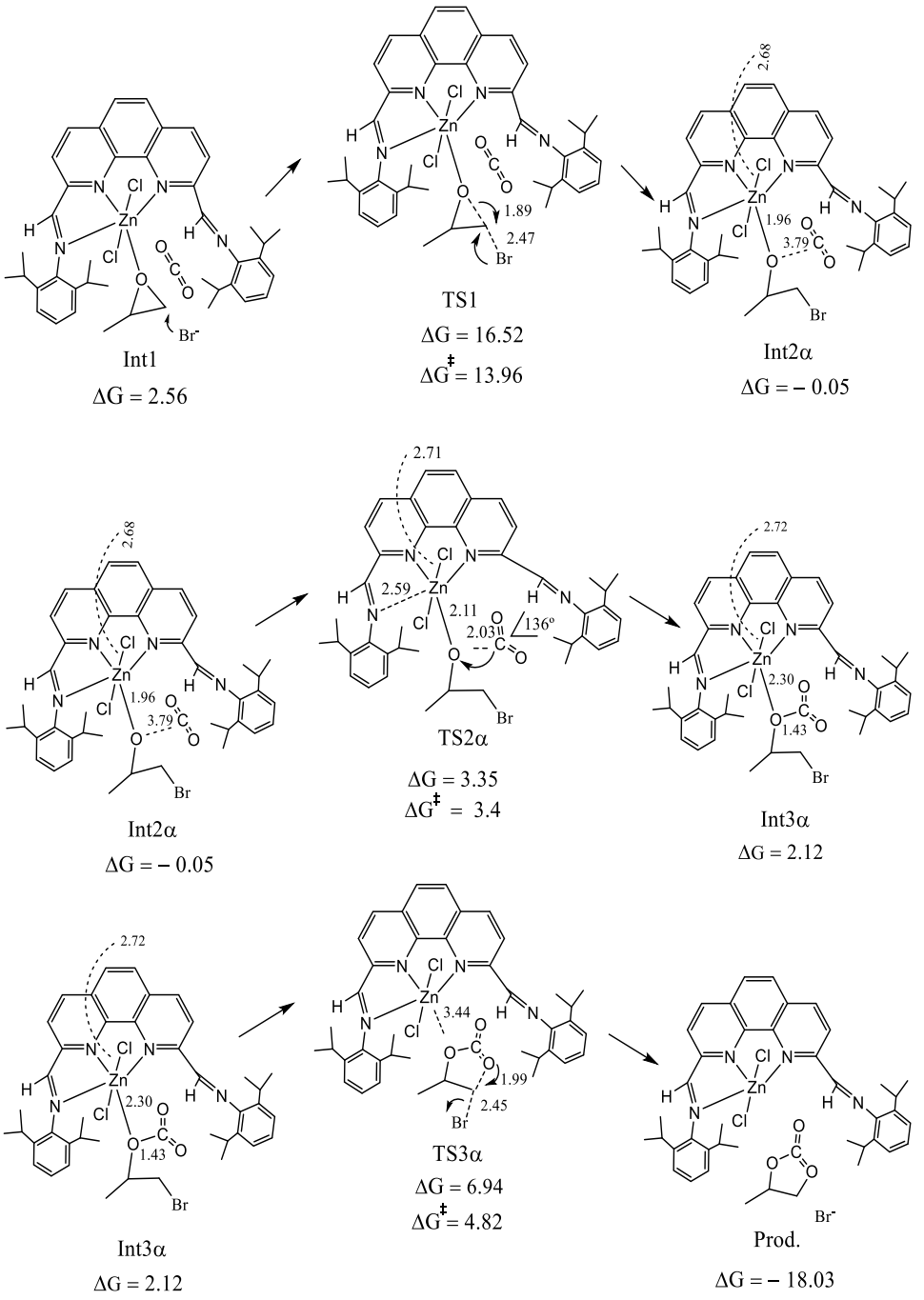

Scheme 5 - 7. Elementary steps of Zn-phen-N4iPr/TBAB-catalyzed CO_2 cycloaddition followed by α-path. Gibbs free energy change is shown in kcal mol^{-1} and the distances in Å.

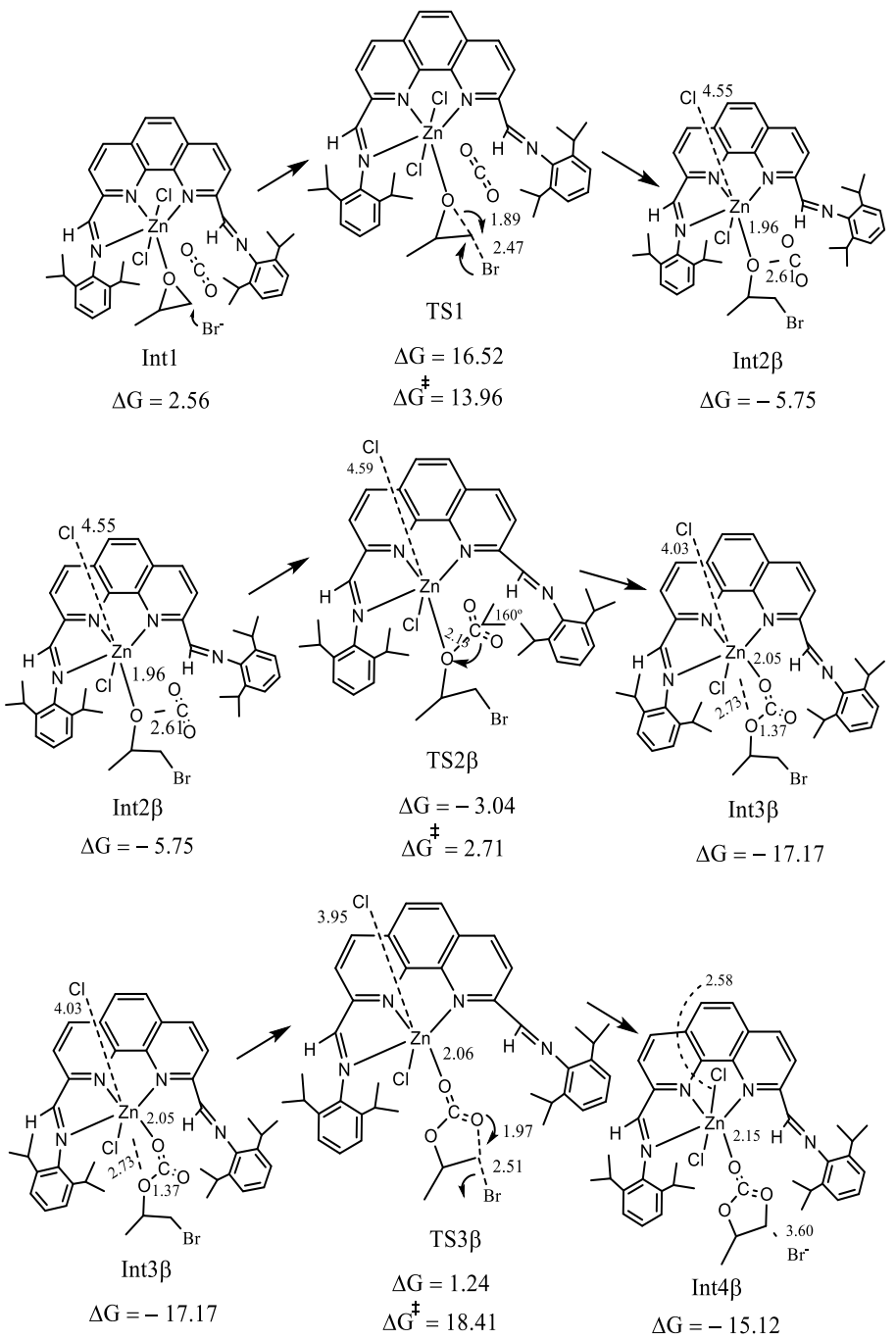

Scheme 5 - 8. Elementary steps of Zn-phen-N4iPr/TBAB-catalyzed CO_2 cycloaddition to PO followed by β-path. Gibbs free energy change is shown in kcal mol^{-1} and the distances in Å.

Table 5 - 4. Activation Gibbs free energies ($\Delta G^{\ddagger}$, in kcal mol^{-1}) of different steps of Zn-phen-N4iPr/TBAB-catalyzed cycloaddition of CO_2 to PO.

Reaction Path	$\Delta G^{\ddagger}_{Int1\rightarrow TS1}$(Epoxide ring opening)	$\Delta G^{\ddagger}_{Int2\rightarrow TS2}$ (CO_2 insertion)	$\Delta G^{\ddagger}_{Int3\rightarrow TS3}$ (Cyclization)
α-path	13.96	3.40	4.82
β-path		2.71	18.41

To verify the substate scope, we extended the mechanism to the substrate SO. The mechanistic study of the Zn-phen-N4iPr/TBAB-catalyzed CO_2 cycloaddition to the substrate SO was carried out following the nucleophilic attack at the stereoselective C_a (see the discussion of Scheme 5 - 5). The energy profile obtained for this reaction is shown in Figure 5 - 9, and the geometries of the crucial structures together with energetic information are gathered in Scheme 5 - 9. For simplicity, CO_2 molecule is treated as an individual entity until it is required in the CO_2 insertion step, i.e., in the transition structure, TS2. Unlike in PO, the nucleophilic (Br^-) attack in SO is assumed to occur at the stereoselective carbon, C_a, which lowers the activation barrier of this step to 6.20 kcal mol^{-1} (see Table 5 - 5), while the corresponding barrier for PO was 13.96 kcal mol^{-1}. These results are found in agreement with the fact described in Scheme 5 - 5. This decreasing of the barrier of this step changes the rate determining step of the CO_2 cycloaddition with SO be the CO_2 cyclization, different from α- and β-path of PO. The activation barrier for cyclization step for SO is 10.17 kcal mol^{-1} which is found lower than that of

corresponding barrier (18.41 kcal mol^{-1}) of β-path of PO but higher than the corresponding barrier (4.82 kcal mol^{-1}) of α-path of PO.

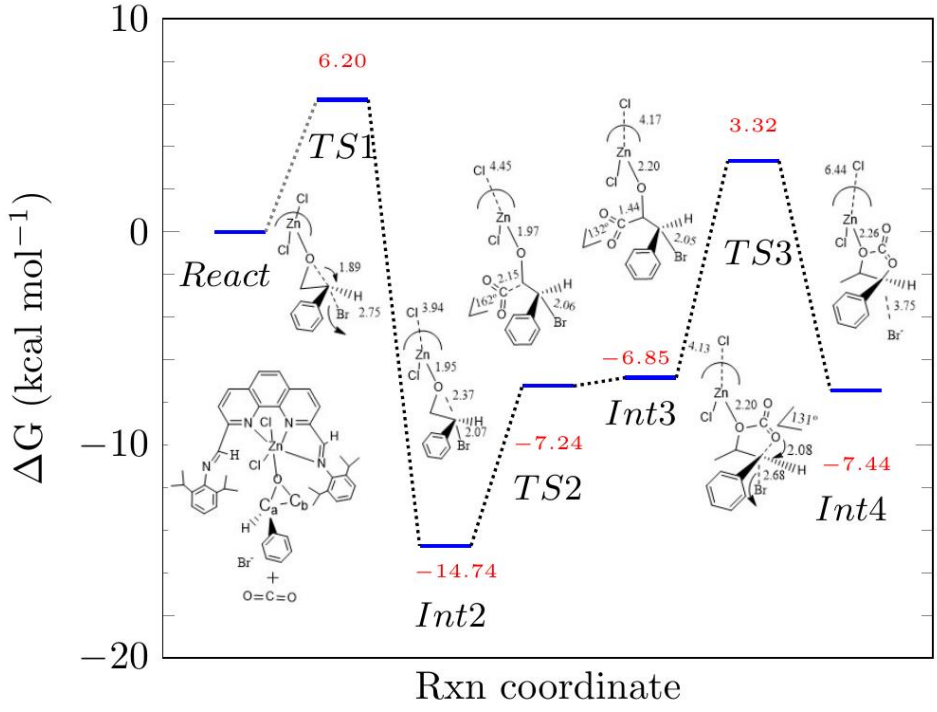

Figure 5 - 9. Gibbs free energy profile of Zn-phen-N4iPr/TBAB-catalyzed CO_2 cycloaddition to SO.

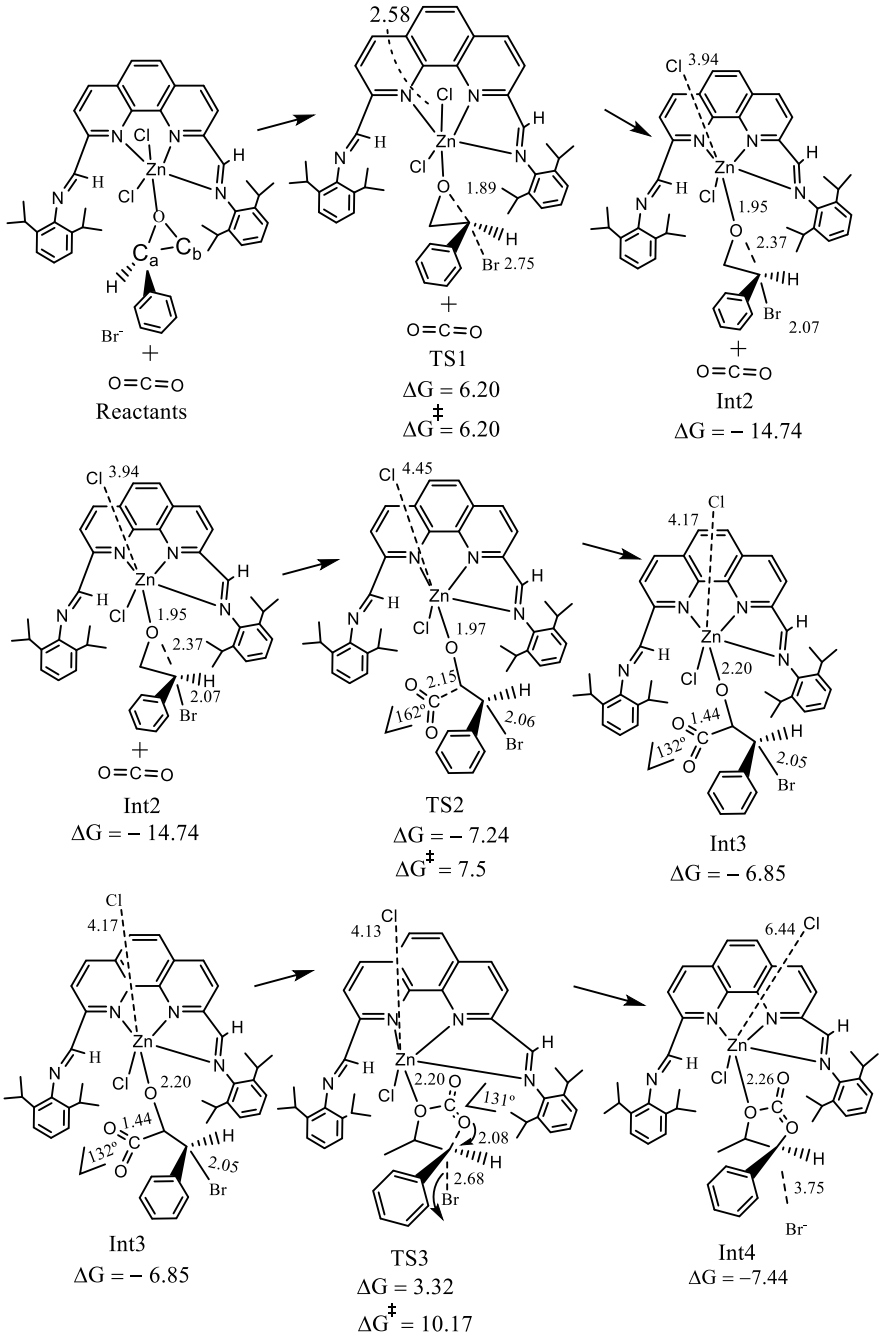

Scheme 5 - 9. Elementary steps of Zn-phen-N4iPr/TBAB-catalyzed CO_2 cycloaddition to SO. Relative Gibbs free energy is shown in kcal mol^{-1} and the distances in Å.

Table 5 - 5. Activation Gibbs free energies ($\Delta G^{\ddagger}$, in kcal mol^{-1}) of different steps of Zn-phen-N4iPr/TBAB-catalyzed cycloaddition of CO_2 to SO.

$\Delta G^{\ddagger}_{Int1\rightarrow TS1}$(Epoxide ring opening)	$\Delta G^{\ddagger}_{Int2\rightarrow TS2}$ (CO_2 insertion)	$\Delta G^{\ddagger}_{Int3\rightarrow TS3}$ (Cyclization)
6.20	7.5	10.17

5.5.2 Mechanistic Study of Model Zn-phen-N4H/TBAB-Catalyzed CO_2 Cycloaddition to PO

To check the influence of the steric effects of the structure of the Zn-phen-N4R catalytic system on its performance, a simplified model catalyst, Zn-phen-N4H, where the bulkier -iPr group is substituted by -H, was chosen to develop a parallel computational study to compare the results. The structures and mechanisms of the Zn-phen-N4H/TBAB-catalyzed CO_2 cycloaddition to PO resembles to its analogous Zn-phen-N4iPr/TBAB. Therefore, for simplicity, the detail structures and energetics of the Zn-phen-N4H/TBAB-catalyzed CO_2 cycloaddition to PO are shown in the Schemes 5C – 1, 5C – 2, and in Scheme 5C – 3 of Appendix. However, the energy profile of the reaction mechanism is represented in Figure 5 - 10.

The activation energy barriers of the characteristic steps of this mechanism are shown in Table 5 - 6. These results show that the rate-

limiting step of the α-path, the epoxide ring opening, is lower here (10.44 kcal mol^{-1}) than in the case of the reaction catalyzed by the Zn-phen-N4iPr/TBAB system (13.96 kcal mol^{-1}). Also, the α-path largely facilitates the cyclization over the β-path by 8.4 kcal mol^{-1}. The steric effect due to the bulky -iPr substituent of the phen-N4 ligand is more likely to hinder the nucleophile to attack the epoxide rather than its coordination to the Lewis acid metal center.[18]

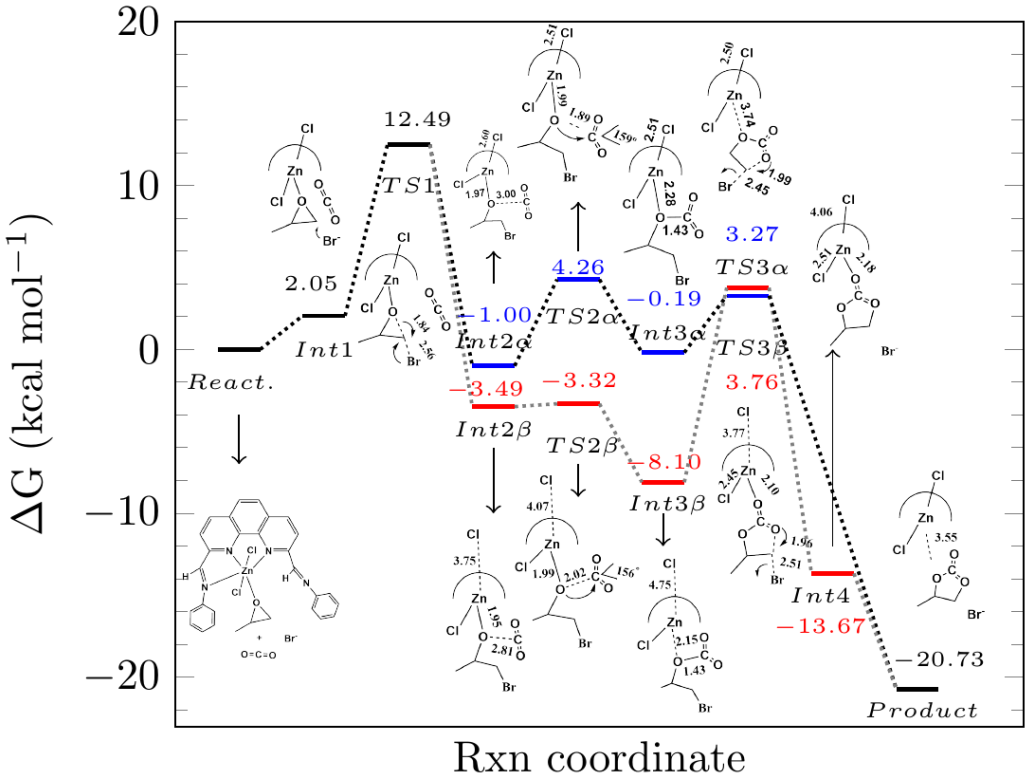

Figure 5 - 10. Relative Gibbs free energy profile of Zn-phen-N4H/TBAB-catalyzed cycloaddition of CO_2 to PO.

Table 5 - 6. Activation Gibbs free energies ($\Delta G^{\ddagger}$, in kcal mol^{-1}) of different steps of Zn-phen-N4H/TBAB-catalyzed cycloaddition of CO_2 to PO.

Reaction Path	$\Delta G^{\ddagger}_{Int1\rightarrow TS1}$(Epoxide ring opening)	$\Delta G^{\ddagger}_{Int2\rightarrow TS2}$ (CO_2 insertion)	$\Delta G^{\ddagger}_{Int3\rightarrow TS3}$ (Cyclization)
α-path	10.44	5.26	3.46
β-path		0.17	11.86

5.3.3 Comparison of Activation Barriers of CO_2 Cycloaddition Reaction Catalyzed by Various Zn Complex based Cooperative Catalysts

Table 5 - 7 summaries various computational studies carried out for the CO_2 cycloaddition to epoxides using various Zinc complex systems based on cooperative catalysts. The entry 1 of Table 5 - 7 shows the results of a study on Zinc 2-N-methyl N-confused porphyrin, $Zn(NCP)Cl^4$ that is used as an efficient catalyst for the conversion of CO_2 into cyclic carbonates. ECH is used as the substrate and the computational method used in this study is B3LYP-D3/6-31G(d). The characteristic activation barriers found, however, are high, particularly, the epoxide ring opening barrier of 15.6 kcal mol^{-1}, but also the cyclization barrier of 15.1 kcal mol^{-1}. Entry 2 of Table 5 - 7 shows the results for Zn-porphyrin/Cl^--catalyzed CO_2 cycloaddition to PO studied at M06/6-311+G(2d,2p),LanL2DZ(Br)//M06/6-31G(d) level.[11] This cooperative

catalyst system lowered the epoxide ring opening barrier to 7.6 kcal mol^{-1}, although the cyclization barrier now is even higher, of 19.5 kcal mol^{-1}.

The results of entry 3 corresponds to the study of the Zn-phen-N4iPr/TBAB catalytic system for CO_2 cycloaddition to PO at CAM-B3LYP-D3BJ/aug-cc-pVDZ,6-311+G(2df,p)(Br/Cl),SMD//CAM-B3LYP-D3BJ/6 31+G(d,p),LanL2DZ(Zn/Br/Cl),SMD level. Following the α-path, this cooperative catalyst lowers the epoxide ring opening barrier from 15.65 kcal mol^{-1} to 13.96 kcal mol^{-1}, when compared with the analogous Zn(NCP)Cl/TBAB. It is notable that this catalyst provides both CO_2 insertion and cyclization steps with low barriers of 3.4 kcal mol^{-1} and 4.82 kcal mol^{-1}, respectively.

Changing the substrate to SO, the results of this study are collected in entry 4 of Table 5 - 7. The Zn-phen-N4iPr/TBAB system lowers the epoxide ring opening barrier to 6.20 kcal mol^{-1}, however, enlarges the CO_2 insertion barrier to 7.5 kcal mol^{-1} and the cyclization barrier to 10.17 kcal mol^{-1}.

Finally, data of entry 5 of Table 5 - 7, represents the results of this work, when a model Zn-phen-N4H/TBAB cooperative system for CO_2 cycloaddition to PO is studied using CAM-B3LYP-D3BJ/aug-cc-pVDZ,6-311+G(2df,p)(Br/Cl),SMD//CAM-B3LYP-D3BJ/aug-cc-pVDZ,6 311+G(2df,p)(Br/Cl),SMD computational model. This catalytic system is able to lower the epoxide ring opening barrier to 10.44 kcal mol^{-1} which is 3.5 kcal mol^{-1} lower than that of the Zn-phen-N4iPr/TBAB system. At the same time, Zn-phen-N4H/TBAB following the α-path maintains the barriers for the CO_2 insertion and cyclization steps low, at 5.26 kcal mol^{-1}

and 3.46 kcal mol^{-1}, respectively. Therefore, Zn-phen-N4H/TBAB would be an optimal catalyst system for the CO_2 addition to epoxides.

Table 5 - 7. Activation Gibbs free energies ($\Delta G^{\ddagger}$, in kcal mol^{-1}) of CO_2 cycloaddition to various epoxides leading to cyclic carbonate.

Entry	Catalytic system	Method	Sub.	Epoxide ring opening	CO_2 insert^{n}	Cycli-zation	Ref.
1	Zn(NCP)Cl/TBAB	B3LYP-D3/6-31G(d)	ECH	15.6	4.8	15.1	[4]
2	Zn-porphyrin/Cl	M06/6-311+G(2d,2p),LanL2DZ(Br)//M06/6-31G(d).	PO	7.6	4.5	19.5	[11]
3	Zn-phen-N4iPr/TBAB (α-path)	§	PO	13.96	3.40	4.82	This work
4	Zn-phen-N4iPr/TBAB	§	SO	6.20	7.5	10.17	This work
5	Zn-phen-N4H/TBAB (α-path)	†	PO	10.44	5.26	3.46	This work

§CAM-B3LYP-D3BJ/aug-cc-pVDZ,6-311+G(2df,p)(Br/Cl),SMD//CAM-B3LYP-D3BJ/631+G(d,p),LanL2DZ(Zn/Br/Cl),SMD
†CAM-B3LYP-D3BJ/aug-cc-pVDZ,6-311+G(2df,p)(Br/Cl),SMD//CAM-B3LYP-D3BJ/aug-cc-pVDZ,6-311+G(2df,p)(Br/Cl),SMD

5.6 Concluding Remarks

Following a systematic conformational analysis, the most stable conformer of Zn-phen-N4iPr complex is obtained and compared with its already available XRD structure. By means of an experimental screening, the catalytic activity of Zn-phen-N4iPr/TBAB system was optimized at 80 ^{o}C, 10 bar and 3h with 0.13/0.2 mol% cat/co-cat ratio for the conversion of benchmark substrate, 1,2-epoxyhexane (EPH). At this optimal condition, the increment of %substrate conversion by the catalyst/co-catalyst pair over the co-catalyst alone were similarly higher for PO and EPH, with increments of 62% and 63%, respectively. Then, from the computational standpoint, we explored two different reaction paths, namely α-path and β-path, for the CO_2 cycloaddition with the model substrate, PO. Surprisingly, the α-path following a concerted mechanism was found to lower the cyclization barrier to a great extent. According to this path, the change of substituents in Zn-phen-N4R from R = iPr to R = H can lower the barrier of the epoxide ring-opening step, possibly due to less steric hindrance. Finally, with the Zn-phen-N4iPr/TBAB system, changing the substrate from PO to SO, the activation energy of the ring-opening step lowers twofold, however, the cyclization barrier is still higher than the cyclization barrier for PO following the α-path.

5.7 References

(1) Liu, T.-F.; Lin, H.-K.; Zhu, S.-R.; Wang, Z.-M.; Wang, H.-G.; Sun, H.-W.; Leng, X.-B.; Chen, Y.-T. *J. Mol. Struct.* **2002**, *605* (1), 117–122.
(2) Chai, L.-Q.; Hu, Q.; Zhang, K.-Y.; Zhou, L.; Huang, J-J. *J. Lumin.* **2018**, *203*, 234–246.
(3) Liu, Y.; Hou, H; Wang, B. *J. Organomet. Chem.* **2020**, *911*, 121123.
(4) Ge, Y.; Cheng, G.; Xu, N.; Wang, W.; Ke, H. *Catal. Sci. Technol.* **2019**, *9* (16), 4255–4261.
(5) Karamé, I.; Tommasino, M. L.; Faure, R.; Lemaire, M. *Eur. J. Org. Chem.* **2003**, *7*, 1271–1276.
(6) Adolph, M.; Zevaco, T. A.; Altesleben, C.; Staudt, S.; Dinjus, E. *J. Mol. Catal. Chem.* **2015**, *400*, 104–110.
(7) Champouret, Y. D. M.; Maréchal, J.-D.; Chaggar, R. K.; Fawcett, J.; Singh, K.; Maseras, F.; Solan, G. A. *New J. Chem.* **2007**, *31* (1), 75–85.
(8) Chen, J.-J.; Xu, Y.-C.; Gan, Z.-L.; Peng, X.; Yi, X.-Y. *Eur. J. Inorg. Chem.* **2019**, *13,* 1733–1739.
(9) Hernández-Ayala, L. F.; Flores-Álamo, M.; Escalante-Tovar, S.; Galindo-Murillo, R.; García-Ramos, J. C.; García-Valdés, J.; Gómez-Vidales, V.; Reséndiz-Acevedo, K.; Toledano-Magaña, Y.; Ruiz-Azuara, L. *Inorganica Chim. Acta* **2018**, *470*, 187–196.
(10) Karamé, I.; Zaher, S.; Eid, N.; Christ, L. *Mol. Catal.* **2018**, *456*, 87–95.
(11) Li, P.; Cao, Z. *Organometallics* **2018**, *37(3),* 406-414.
(12) Angeloff, A.; Daran, J.-C.; Bernadou, J.; Meunier, B. *Eur J Inorg Chem* **2000**, *9*, 1985–1996.
(13) Wang, A.; Fan, R.; Zhou, X.; Hao, S.; Zheng, X.; Yang, Y. *ACS Appl. Mater. Interfaces* **2018**, *10*(11), 9744-9755.
(14) Bencini, A.; Lippolis, V. *Coord. Chem. Rev.* **2010**, *254* (17–18), 2096–2180.
(15) Laia, C.-A.; Ariadna, C.-C; Castilla, J.; Reguero, M.; Masdeu-Bulto, A. M.; Aghmiz, A. *J. CO_2 Util.* **2016**, *14*, 10–22.
(16) Liu, C.; Luo, Y.; Lu, X. *J. Polym. Sci.* **2016**, *34* (4), 439–445.
(17) Yang, Y.; Li, F.; Yang, C.; Jia, L.; Yang, L.; Xia, F.; Peng, J. *Aust. J. Chem.* **2020**, *73* (1), 30–42.
(18) Pescarmona, P. P.; Taherimehr, M. *Catal Sci Technol* **2012**, *2* (11), 2169–2187.
(19) López-Redondo, C.; El Aouni, N.; Masdeu-Bultó, A. M. Unpublished Results.
(20) Wang, L.; Sun, W.-H.; Han, L.; Yang, H.; Hu, Y.; Jin, X. *J. Organomet. Chem.* **2002**, *658* (1), 62–70.

CHAPTER 6:

Fe(III)-Cyclam Derived Complex as Catalyst in CO_2 Cycloaddition to Epoxides

6.1 Introduction

Cyclam (1,4,8,11-tetraazacyclotetradecane) is a four nitrogen (N4) donor macrocyclic ligand which strongly binds to transition metals.[1] Metal complexes with cyclam derived ligands are active catalysts for many organic transformations e.g., epoxidation of olefins[2], CO_2 reduction[3], oxidation of alcohols[4,5] and water[5] etc. Cyclam is prepared from its simpler analogous ligand, ethylenediamine, reacting with 1,3-dibromopropane.[6] Both ligands are sketched in Scheme 6 - 1. Ethylenediamine and cyclam ligands are also used to synthesize coordination complexes with various metals such as Co, Ni, and Cu giving the complexes shown in Scheme 6 - 2. In ionic liquid (IL), these complexes were used as catalysts for synthesis of cyclic carbonates from CO_2 and epoxides (Scheme 6 - 3).[7]

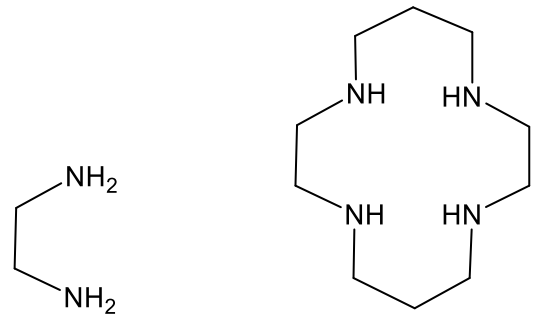

(a) Ethylenediamine (b) Cyclam

Scheme 6 - 1. (a) Ethylenediamine, and (b) cyclam ligand.

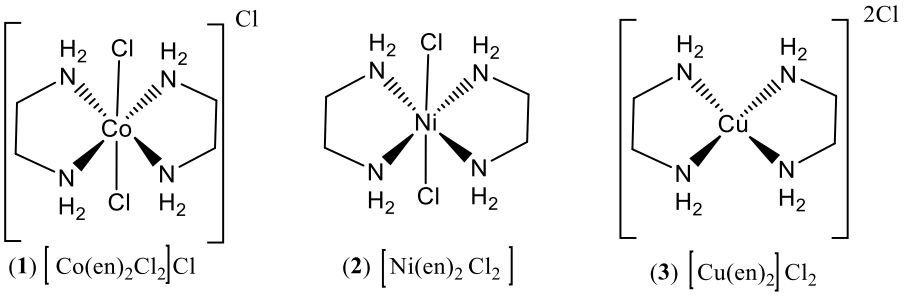

(**1**) $\left[Co(en)_2Cl_2 \right]Cl$ (**2**) $\left[Ni(en)_2 Cl_2 \right]$ (**3**) $\left[Cu(en)_2 \right] Cl_2$

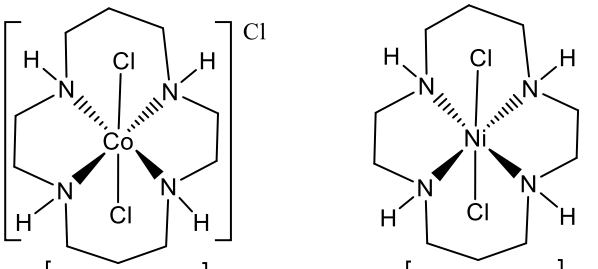

(**4**) $\left[Co(cyclam)Cl_2 \right]Cl$ (**5**) $\left[Ni(cyclam)Cl_2 \right]Cl$

Scheme 6 - 2. Metal complexes applied for CO_2 cycloaddition to epoxides.[7]

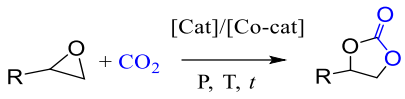

Scheme 6 - 3. General reaction scheme of CO_2 cycloaddition to epoxides.

The catalytic activity of these complexes has been studied in different conditions. In the ionic liquid 1-n-butyl-3-methylimidazolium bis (trifluoromethanesulfonyl) imide (BMIm.NTf_2), 5 mol% $[Ni(en)_2]Cl_2$ provided 84% CC at 180 °C under 5 bar CO_2 pressure during 4h. In case of 1-n-butyl-3-methylimidazolium tetrafluoroborate (BMIm.BF_4), 5 mol% of $[Ni(en)_2Cl_2]$ and $[Co(en)_2Cl_2]Cl$ at 150 °C under 5 bar pressure in 4h gave 95% and 100% yield, respectively. With propylene oxide (PO) in BMIm.NTf_2, $[Co(cyclam)_2Cl_2]Cl$ gave an yield of 19% whereas $[Co(en)_2Cl_2]Cl$ was not active. In BMIm.BF_4, $[Co(cyclam)Cl_2]Cl$ and $[Ni(cyclam)Cl_2]Cl$ complexes showed even higher yield, 73% and 61%, respectively. But, in case of the substrate styrene oxide (SO), ethylenediamine complexes gave higher yields than the corresponding cyclam complexes.[7]

Lately, complexes of high abundant and environmentally friendly iron(II) and iron(III) have demonstrated to be very active and selective catalysts for the formation of cyclic carbonate and/or polycarbonates.[5,7–9] Scheme 6 - 4 shows square pyramidal N4 donor tetraamine Fe(II) complex **1** along with its reduced diimine-diamine Fe(II) complex **2**, and N_2O_2 donor Fe(III) complex **3,** all of them are active for the CO_2 coupling to epoxides to yield cyclic carbonate. This scheme also shows a trigonal bipyramidal Fe(III) aminobis(phenolate) complex **4** which is found

selective for the formation of cyclic carbonate and/or polycarbonates. Depending on a range of factors, including the metal-center geometry, electronics of the phenolate substituents within the ligand and the ratio of iron to external cocatalyst used, the reaction was found selective towards either cyclic or polycarbonate formation.[7]

With the Fe(II) complexes, 0.1/0.1 mol% **1**/TBAB and **2**/TBAB binary systems at 130 ^{o}C, 40 bar CO_2 pressure could reach more than 99% PO conversion in 4h. In case of the substrate, epichlorohydrin (ECH), **2**/TBAB-catalyzed reaction under the same conditions but at a lower temperature of 100 ^{o}C gets a 97% conversion. However, a higher molar ratio of 0.2/0.2 mol% of **2**/TBAB was required to get a 47% cyclohexene oxide (CHO) conversion at 100 ^{o}C, 40 bar CO_2 pressure during 12h.[10,11] The results are collected in Table 6 - 1.

Among the Fe(III) complexes, 0.025/0.1 mol% of 3/TBAB at 100 ^{o}C, 20 bar CO_2 pressure in 22h converted 74% of PO, 78% of ECH, 31% of SO and 9% of CHO.[8] On the other hand, a 0.025/0.1 mol% of 4/PPNCl(Bis(triphenylphosphine)iminium chloride) binary system converted more than 99% PO into propylene carbonate (PC) at 100 ^{o}C, 20 bar CO_2 pressure after a longer time of 22h. Nevertheless, a 0.5/0.5 mol % of 4/PPNCl binary converted 99% of CHO into polycyclohexene carbonate (PCHC) and/or *cis*-CHC at relatively lower temperature of 60 ^{o}C but at higher CO_2 pressure of 60 bar during 22h.[10] These results also are collected in Table 6 - 1.

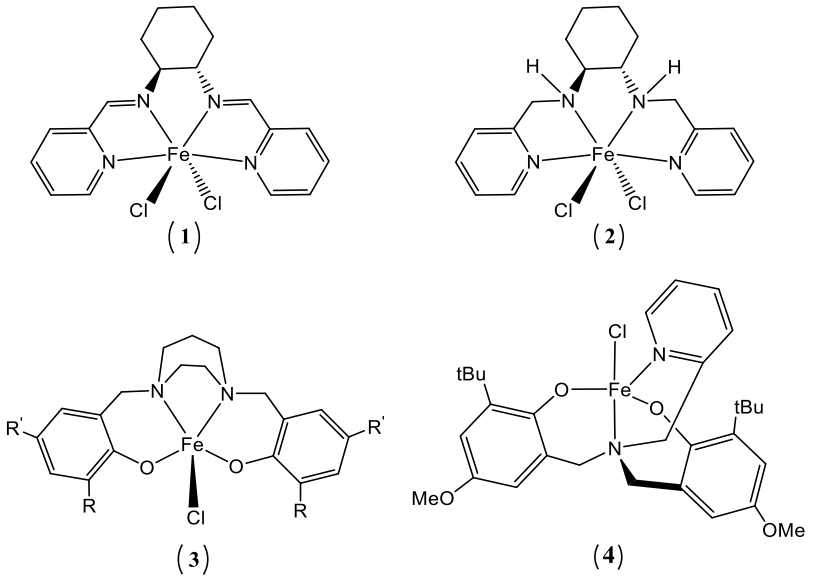

Scheme 6 - 4. Square pyramidal N4 donor tetraamine Fe(II) complex **1**, diimine-diamine Fe(II) complex **2,** N_2O_2 donor Fe(III) complex **3**, and trigonal bipyramidal Fe(III) aminobis(phenolate) complex **4**.

Table 6 - 1. Fe complex/nucleophile catalyzed CO_2 cycloaddition with epoxides to yield cyclic carbonate and/or polycarbonates.

Entry	Catalytic system	Cat/Co-cat (mol %)	Sub.	T (^oC)	P (bar)	t (h)	Conv. (%)	TOF (h^{-1})
1	**1**/TBAB	0.1/0.1	PO	130	40	4	>99	250
2	**2**/TBAB	0.1/0.1	PO	130	40	4	>99	250
3	**2**/TBAB	0.05/0.1	ECH	100	40	4	97	243
4	**2**/TBAB	0.2/0.2	CHO	100	40	12	47	20
5	**3**/TBAB	0.025/0.1	PO	100	20	22	74	135
6	**3**/TBAB	0.025/0.1	ECH	100	20	22	78	142

7	**3**/TBAB	0.025/0.1	SO	100	20	22	31	57
8	**3**/TBAB	0.025/0.1	CHO	100	20	22	9	17
9	**4**/PPNCl	0.025/0.1	PO	100	20	22	>99	-
10	**4**/PPNCl	0.5/0.5	CHO	60	60	22	99*	-

*formation of PCHC and/or cis-CHC

A synthesis of iron complexes[5] with cross-bridged cyclams is depicted in Scheme 6 - 5. These complexes can bind CO_2 in various structural motifs. In a recent ultrafast mid-infrared spectroscopic study, CO_2 was found to bind to the iron center of the cyclam complex **5**.[12] Two vastly different prominent CO_2 binding modes are shown in Scheme 6 - 6. The $\eta^1_{O,bent}$ mode, Scheme 6 - 6(a), is a recently discovered mode which involves the binding via a terminal oxygen atom but in a bent geometry. Scheme 6 - 6(b) shows the η^2_{CO} mode which includes the binding of a bent ligand forming either a π-complex or a metallaoxacyclopropane. Because of their massively different spin-density distributions over the triatomic CO_2, two quite diverse binding motifs, $\eta^1_{O,bent}$ and η^2_{CO}, display very distinct chemical reactivity.

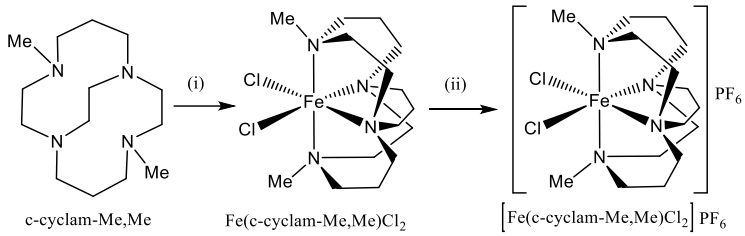

(i) $FeCl_2$, Dimethylacetamide (DMAC), 100ºC; (ii) Br_2, NH_4PF_6, Methanol, RT

Scheme 6 - 5. Synthesis of $[Fe^{III}(c\text{-cyclam-Me,Me})Cl_2]PF_6$ from c-cyclam-Me,Me.[5]

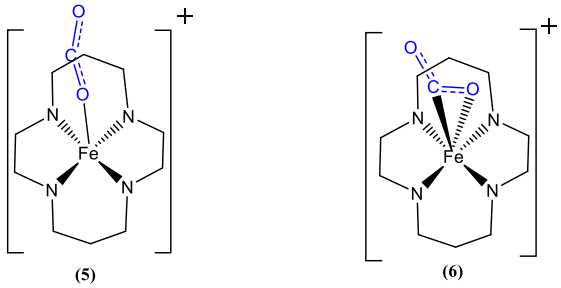

(a) $\left[Fe(cyclam)(basal\text{-}\eta_O{}^1\text{–}OCO)\right]^+$ (b) $\left[Fe(cyclam)(equat.\text{-}\eta^2{}_{CO}\text{–}CO_2)\right]^+$

Scheme 6 - 6. Two prominent CO_2 binding modes to Fe(III)-cyclam.[12]

Herein, we study the catalytic activity of $[Fe^{III}(c\text{-cyclam-Me,Me})Cl_2]PF_6$/TBAB (Scheme 6 - 5) cooperative catalytic system in CO_2 cycloaddition reaction to epoxides. The complex $[Fe^{III}(c\text{-cyclam-Me,Me})Cl_2]PF_6$ was prepared in the group of Professor F. Ruffo (University of Naples Federico II, Italy). The catalytic reaction conditions are optimized. The substrate scope of the catalysis is also investigated. Finally, considering the functions of each catalytic components, the chapter in closed with a proposal of the mechanism of this catalytic reaction.

6.2 Experimental Setup

6.2.1 Materials

$[Fe^{III}(c\text{-cyclam-Me,Me})Cl_2]PF_6$ was available from the research group of Prof. Francesco Ruffo, University of Naples Federico II, Italy.[5] Substrates 1,2-epoxyhexane (EPH), propylene oxide (PO), styrene oxide (SO), epichlorohydrin (ECH), and cyclohexene oxide (CHO) were used as received from Sigma Aldrich. Tetrabutylammonium bromide (TBAB) was used as co-catalyst. CO_2 gas cylinders (99.99% pure) were purchased from Linde, Germany. ^1H NMR were recorded in a Varian spectrometer at room temperature in $CDCl_3$. Chemical shifts were reported in parts per million (ppm, δ).

6.2.2 Catalytic Experiments

The catalytic experiments were caried out in a 25 mL Parr reactor. Reactions were set at 950 rpm stirring. Reactions were conducted with different catalyst/co-catalyst ratio by changing the temperature in between 80 ^oC to 100 ^oC, a pressure change from 20 bar to 10 bar, and during 3h. After the reaction time, the autoclave was cooled in ice bath until room temperature, and the pressure released. Then, the autoclave was opened, and the content was analyzed by ^1H NMR spectroscopy using mesitylene as internal standard. The %conversion and %yield were

determined from ^{1}H NMR of the crude mixture from the integral ratio of the signals corresponding to the produced cyclic carbonate and individual substrate epoxide fed.

6.2.3 Recycling Experiment

The recycling experiment was carried out with the product mixture from the conversion of PO into PC. Volatile PO (boils at 35 ^{o}C) was easily evaporated from the crude under vacuum and then a micro-distillation column under vacuum was used to separate the carbonate. The collected PC from the distillation was found pure in NMR study (see Figure 6A – 6, in Appendix). The distillation residue, the catalyst with co-catalyst, was then reintroduced for a following PO conversion experiment.

6.3 Results and Discussion

6.3.1 Catalytic Screening

To find an optimal reaction conditions of CO_2 cycloaddition of 1,2-epoxyhexane into cyclic carbonate, a systematic experimental catalytic screening was carried out by changing different parameters such as catalyst/co-catalyst ratio (1:2 and 1:5), altering the temperature between 80 ^{o}C to 100 ^{o}C, the initial pressure from 20 bar to 10 bar, and always at 3h of reaction time. The results in Table 6 - 2 shows different reaction

conditions for the CO_2 coupling to the chosen benchmark substrate 1,2-epoxyhexane (EPH). First, we studied the influence of cat/co-cat ratio on the reaction %conversion and %yield. Then we monitored the effect of temperature, and pressure.

Complex $[Fe^{III}(c\text{-cyclam-Me,Me})Cl_2]PF_6$ (0.05 mol%) alone or TBAB (0.1 mol%) alone were not active in the reaction as shown in entries 1 and 2 of Table 6 - 2, respectively. However, the combination of the complex and TBAB at ratio of 0.05/0.1 mol% of catalyst/co-catalyst converts 8% EPH with a TOF of 58 h^{-1} (entry 3, Table 6 - 2). Then, the influence of the complex/TBAB ratio was analyzed. Increasing the co-catalyst from 0.1 mol% to 0.25 mol% increased the %conversion from 8% to 16% (entry 3 vs. entry 4, Table 6 - 2).

Using only co-catalyst TBAB, an increase of co-catalyst loading from 0.1 mol% to 0.25 mol% with a temperature increase from 80 ^oC to 100 ^oC increases the substrate conversion from 2% to 36% (entry 5 vs. entry 2, Table 6 - 2). Similarly, entry 6 has the same 0.05/0.1 mol% catalyst/co-catalyst as the entry 3 but an increase of 20 ^oC temperature elevates the conversion fourfold from 8% to 36% with an increased TOF to 255 h^{-1}. Increasing the co-catalyst loading from 0.1 mol% (entry 6) to 0.25 mol% (entry 7) increases the conversion twofold from 36% to 63% and the TOF increases from 255 h^{-1} to 445 h^{-1}.

With 0.25 mol% of co-catalyst at 100 ^oC, a lowering of the pressure from 20 bar to 10 bar decreased the conversion to 22% (entry 8, Table 6 - 2). A pressure drop of 10 bar decreases the conversion and TOF twofold (entry 9 vs. entry 7, Table 6 - 2). At a lower temperature of 80 ^oC and lower

pressure of 10 bar, the conversion decreased to 22% (entry 11, Table 6 - 2) which is a similar value to the one obtained with TBAB under the same conditions (entry 10, Table 6 - 2).

Table 6 - 2. Screening conditions of CO_2 cycloaddition to the substate 1,2 epoxyhexane to produce cyclic carbonate catalyzed by Fe^{III}(c-cyclam-Me,Me)Cl_2]PF_6/TBAB system.

Entry	Cat/Co-cat (mol %)	T (°C)	P (bar)	t (h)	Conv. [a] (%)	Yield[b] (%)	TOF[c] (h^{-1})
1	0.05/-	80	20	3	0	-	-
2	-/0.1	80	20	3	2	2	-
3	0.05/0.1	80	20	3	8	6	58
4	0.05/0.25	80	20	3	16	13	113
5	-/0.25	100	20	3	36	31	48
6	0.05/0.1	100	20	3	36	32	255
7	0.05/0.25	100	20	3	63	53	445
8	-/0.25	100	10	3	22	19	-
9	0.05/0.25	100	10	3	38	32	264
10	-/0.25	80	10	3	18	12	-
11	0.05/0.25	80	10	3	22	20	152

[a, b] Average conversion and yield determined by ^{1}H NMR with mesitylene as internal standard; [c]TOF in mole substrate converted as $(mol.catalyst)^{-1}.h^{-1}$.

Considering all the involved parameters, the best reaction conditions were 100 °C, 20 bar with a Cat/Co-Cat ratio 1/5 (entry 7, Table

6 - 2) which give the highest conversion of 63% and highest TOF of 445 h^{-1}. These conditions were thus chosen for the following studies.

6.3.2 Substrate Scope

To study the substrate scope, a list of substrates (see Figure 6 - 1) were examined for CO_2 cycloaddition at the chosen optimal reaction conditions of 0.05/0.25 mol% catalyst/co-catalyst ratio at 100 ^oC, 20 bar and in 3h. The results are shown in Table 6 - 3. A higher conversion of 95% was found for PO whereas it converted 63% of EPH (entry 4 vs. entry 2, Table 6 - 3). The conversion with TBAB alone also follows a similar trend and is higher for PO (46%, entry 3) than that of EPH (36%, entry 1). The higher conversion obtained with PO than with EPH is attributed to steric effects of the longer alkylic chain in EPH.

With TBAB alone, conversion of SO, entry 5 of Table 6 - 3, is 59% which is already 23% more than the corresponding %conversion of the benchmark EPH. As can be seen in entry 7 of Table 6 - 3, the conversion of epichlorohydrin (ECH) with TBAB alone is even higher of 89%. Then, incorporating the catalyst, the resulting cat/co-cat system improves the SO conversion to 77% (entry 6; for ^{1}NMR, see Figure 6A – 3 in Appendix) and the ECH conversion to 93% (entry 8; for ^{1}NMR, see Figure 6A – 4 in Appendix).

However, in entry 10*, spanning a longer time up to 6h, the total conversion of cyclohexene oxide (CHO) catalyzed by Fe^{III}(c-cyclam-Me,Me)Cl_2]PF_6/TBAB reaches 44%. As indicated in Figure 6A – 5

(Appendix), this conversion may yield some PCHC along with its major product *cis*-CHC. However, NMR didn't show any evidence of polycarbonate formation. To compare with entry 9* of Table 6 - 3, in same time span, TBAB alone could convert a 36% of CHO.

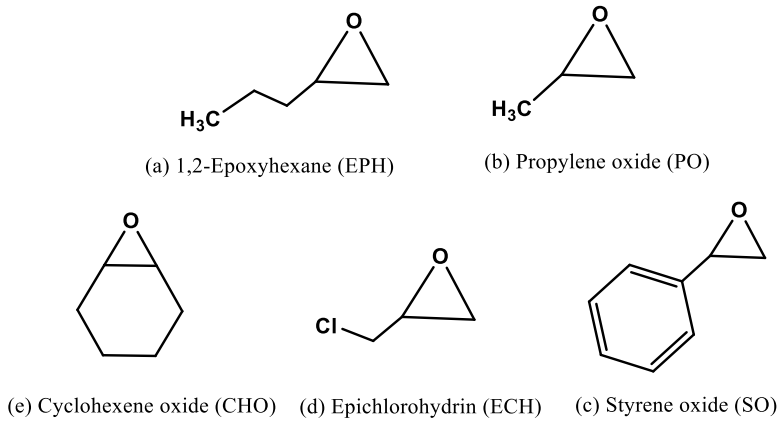

Figure 6 - 1. Substrates used in Fe^{III}(c-cyclam-Me,Me)Cl_2]PF_6/TBAB catalyzed CO_2 cycloaddition.

To see the improvement of the catalytic activity of Fe^{III}(c-cyclam-Me,Me)Cl_2]PF_6/TBAB over the co-catalyst TBAB, the corresponding increment on the conversion of the substrates is illustrated in Figure 6 - 2. As can be seen from the figure, the highest increment of 49% is obtained for the substrate PO, followed by 27% increment for EPH and 18% for SO conversion. The increment on the %conversion from ECH and CHO is found lower to 4% and 8%, respectively.

Table 6 - 3. Substrate scope of Fe^{III}(c-cyclam-Me,Me)Cl_2]PF_6/TBAB catalyzed CO_2 cycloaddition to yield cyclic carbonate.¶

Entry	Sub.	Cat/Co-cat (mol %)	Conv.[a](%)	Yield[b] (%)	TOF[c]
1	EPH	-/0.25	36	31	-
2	EPH	0.05/0.25	63	53	445
3	PO	-/0.25	46	22	-
4	PO	0.05/0.25	95	54	689
5	SO	-/0.25	59	54	-
6	SO	0.05/0.25	77	67	541
7	ECH	-/0.25	89	80	-
8	ECH	0.05/0.25	93	88	605
9*	CHO	-/0.25	36	23	-
10*	CHO	0.05/0.25	44	33	150

¶ Reaction conditions: 100 ^oC, 20 bar, and 3h.
*6h; [a, b] Average conversion and yield were determined by ^1H NMR with mesitylene as internal standard. [c]TOF in mole substrate converted as $(mol.catalyst)^{-1}.h^{-1}$.

To sum up, the combination of Fe^{III}(c-cyclam-Me,Me)Cl_2]PF_6 with TBAB produced an increase of conversion from 4% to 49%. The highest synergic effect was observed for PO, while for a more activate substrate such as ECH the improvement of using both components was low (only 4 %).

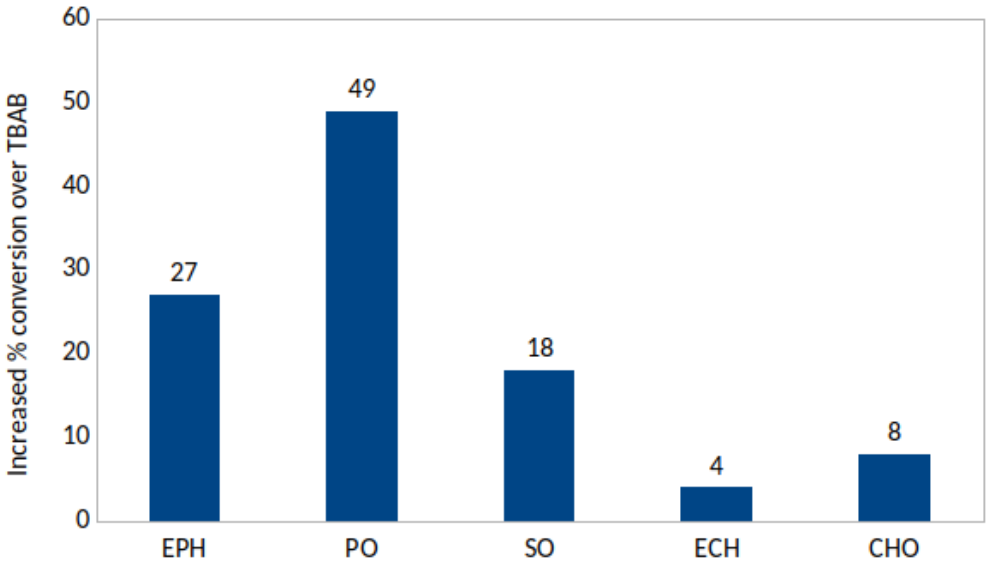

Figure 6 - 2. Increment on the % conversion of different substrates due to Fe^{III}(c-cyclam-Me,Me)Cl_2]PF_6 catalyst over TBAB co-catalyst. (Reproduced from the data in Table 6 - 3)

The catalytic activity of the [Fe^{III}(c-cyclam-Me,Me)Cl_2]PF_6/TBAB system observed in this study (entry 4, Table 6 - 3) was compared with the literature results of **1**/TBAB system (entry 1, Table 6 - 1) which contains a N4 donor tetraamine Fe(II) complex. The latter system is found as the best performing catalyst of its kind. The comparison is shown for the PO conversion into PC. From this comparison, one may conclude that the [Fe^{III}(c-cyclam-Me,Me)Cl_2]PF_6/TBAB catalytic system provides a similar performance with a twofold lower catalytic loading at relatively milder reaction conditions of 100 ^{o}C, 20 bar and 3h. Moreover, it gives a more than twofold higher TOF of 689 h^{-1} than that of the **1**/TBAB system (250 h^{-1}).

6.3.3 Catalysis with Recycled Catalytic System

Recycling of the catalyst Fe^{III}(c-cyclam Me,Me)Cl_2]PF_6 in the CO_2 cycloaddition reaction with PO is shown in Table 6 - 4 . In a regular run 1, Fe^{III}(c-cyclam Me,Me)Cl_2]PF_6/TBAB converted 95% of PO. The catalyst was separated from the remaining PO and PC by distillation and reused without addition of fresh TBAB. After recycling, the same regenerated catalytic system was used in a second run, run 2, which still gave a 73% PO conversion. The decrease in conversion may be due to partial decomposition of the complex or the TBAB.

Table 6 - 4. Recycling of the catalytic Fe^{III}(c-cyclam Me,Me)Cl_2]PF_6/TBAB system in the cycloaddition of CO_2 to PO.

Run	%Conv.
1	95
2	73

Reaction conditions: PO: 41.19 mmol, Cat/Co-cat: 0.05/0.25 mol%, T = 100 °C, P = 20 bar CO_2, t = 3h. Conversion determined by ^{1}H NMR.

6.4 Proposed Mechanism

Based on a previous report[7] and considering electronic and steric effects, Scheme 6 - 7 proposes a mechanism for CO_2 cycloaddition to epoxides catalyzed by metal-cyclam/nucleophile binary system. First, in step 1, the metal center would act as a Lewis acid which would coordinate

the oxygen atom of the epoxide while dissociating a Cl^-. Afterwards, a bromide nucleophile, from the co-catalyst TBAB, attacks and opens the epoxide ring (step 2). The generated alkoxide then, in step 3, inserts a CO_2 molecule to form a cyclic carbonate (step 4) in the subsequent cyclization step. Finally, in step 5, the product, cyclic carbonate, dissociates and the catalyst is regenerated.

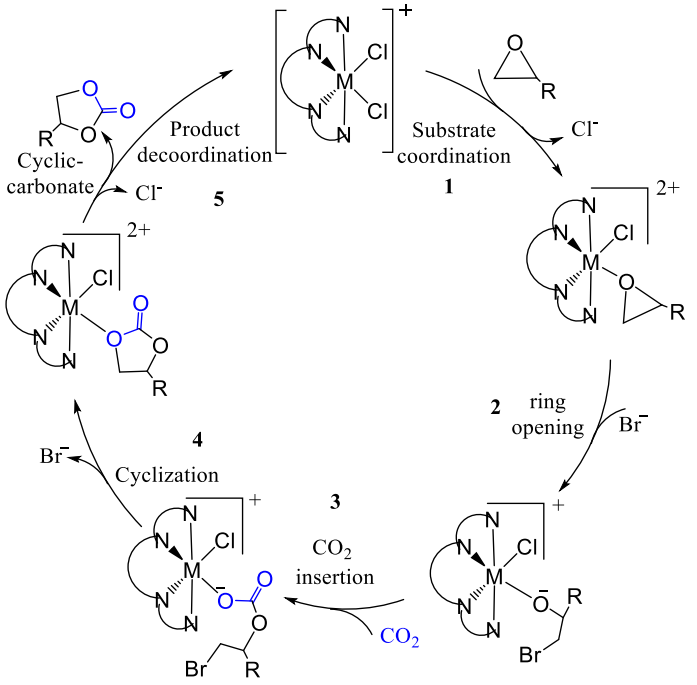

Scheme 6 - 7. Proposed catalytic cycle for Fe^{III}(c-cyclam-Me,Me)Cl_2]PF_6/TBAB catalyzed CO_2 cycloaddition with epoxides to yield cyclic carbonate.[7]

However, in the case of the substrate CHO, the catalytic cycle can be different. Some iron catalysts are reported for selective formation of

both polycarbonate and cyclic carbonate with CHO. Due to the high strain to make the cyclization (step 4), the reaction might follow an alternative path via step 3* to form polycarbonates as shown in Scheme 6 - 7. In this way, the reaction would consume two equivalent CHO and CO_2. Therefore, polycarbonate product would be favored in reaction conditions of higher CO_2 pressure and in higher concentration of CHO. But increasing the amount of cocatalyst, the product selectivity may switch from PCHC to *cis*-CHC.[10]

6.5 Conclusions

Fe (III)-cyclam complex in combination with a nucleophile, TBAB is found to be active in the CO_2 cycloaddition reaction with epoxides to form cyclic carbonates selectively. The reaction is optimized for the benchmark substrate, 1,2-epoxyhexane to achieve TOF 689 h^{-1}. Among a series of substrates, the highest increment of 49% conversion over the co-catalyst TBAB was found for propylene oxide. The catalytic system Fe^{III}(c-cyclam-Me,Me)Cl_2]PF_6/TBAB was recycled and reused for the reaction of PO conversion into PC, although a decrease of conversion was observed. A reaction mechanism is proposed for the formation of cyclic carbonates from chemical intuition.

6.6 References

(1) Barefield, E. K. *Coord. Chem. Rev.* **2010**, *254* (15–16), 1607–1627.
(2) Engelmann, X.; Malik, D. D.; Corona, T.; Warm, K.; Farquhar, E. R.; Swart, M.; Nam, W.; Ray, K. *Angew. Chem. Int. Ed.* **2019**, *58* (12), 4012–4016.
(3) Nichols, E. M.; Chang, C. J. *Organometallics* **2019**, *38* (6), 1213–1218.
(4) Zhang, Z.; Khrouz, L.; Yin, G.; Andrioletti, B. *Eur. J. Org. Chem.* **2019**, 323-327.
(5) Annunziata, A.; Esposito, R.; Gatto, G.; Cucciolito, M. E.; Tuzi, A.; Macchioni, A.; Ruffo, F. *Eur. J. Inorg. Chem.* **2018**, *28*, 3304–3311.
(6) Alphen, J. van. *Recl. Trav. Chim. Pays-Bas* **1937**, *56* (4), 343–350.
(7) Honores, J.; Quezada, D.; Chacón, G.; Martínez-Ferraté, O.; Isaacs, M. *Catal. Lett.* **2019**, *149* (7), 1825–1832.
(8) Alhashmialameer, D.; Collins, J.; Hattenhauer, K.; Kerton, F. M. *Catal. Sci. Technol.* **2016**, *6* (14), 5364–5373.
(9) Andrea, K. A et al. Inorg. Chem. **2019**, *58* (16), 11231.
(10) Andrea, K. A.; Kerton, F. M. *Polym. J.* **2021**, *53* (1), 29–46.
(11) Sheng, X. et al. *Polyhedron* **2014**, *74*, 129–133.
(12) Straub, S.; Vöhringer, P. *Angew. Chem. Int. Ed.* **2021**, *60* (5), 2519–2525.

CHAPTER 7:

General Conclusions

The aim of this doctoral thesis was to use low toxic catalysts based on natural compounds or earth abundant metals to produce organic carbonates using CO_2 as a chemical feedstock. Different types of epoxides were chosen as reactive substrates to assist the chemical transformation of the inert small molecule, CO_2. Hydrogen bond donor catalysts and metal complex catalysts in combination of co-catalysts are established as robust cooperative catalytic systems to activate the reactants and/or to stabilize the intermediate reaction species in a synergetic approach. The elucidation of reaction pathways unfolded the nature of the catalytic active sites, the effects of the substrates on the catalytic activity, and possible improvements towards rational catalytic designs. The conclusions extracted from this work are summarized as followings:

- We were able to model the catalytic components of lignocellulosic materials. Molecular modelling of these catalytic reactions showed that the 1,2- and 1,3- diol of the cellulose and lignin fragments, respectively, activate epoxides by H-bonding. In other words, the -OH groups present in hollocellulose and lignin of lignocellulosic materials contribute to their activity as catalysts. The %substrate conversion by LiG/TBAB binary system was higher than that of CtS/TBAB system, what was in agreement with the lower barrier

of the cyclic carbonate ring-closing step of the reaction of the former system.

- The most stable conformer of Zn-phen-N4H and Zn-phen-N4iPr complexes were found from systematic conformational analyses. However, in case of Zn-phen-N4iPr, the conrotatory and disrotatory motions became almost indistinguishable. The DFT optimized Zn-phen-N4iPr structure fits with its the X-ray diffraction structure. Nevertheless, during the mechanistic studies, the catalytic active site(s) had gone through structural changes that proves that the conformational analysis was useful to predict the catalytic stability but not the catalytic activity.
- The reaction conditions for the catalytic activity of Zn-phen-N4iPr/TBAB system were optimized at 80 ^{o}C, 10 bar and 3h with 0.13/0.2 mol% cat/co-cat ratio for the conversion of the benchmark substrate, 1,2-epoxyhexane (EPH) to obtain a TOF about 200 h^{-1}. At this optimal condition, the increment of substrate conversion by the catalyst over the co-catalyst were similarly higher for PO and EPH to 62% and 63%, respectively. Unfortunately, we could not recycle the catalyst, Zn-phen-N4iPr.
- We also studied the mechanism of this reaction from the computational standpoint. We explored two different reaction paths, namely α-path and β-path, for the CO_2 cycloaddition with a model substrate, PO catalyzed by of Zn-phen-N4iPr/TBAB system. Surprisingly, the α-path following a concerted mechanism was found to lower the cyclization barrier to a great extent. According

to this path, the changing of the substituents in Zn-phen-N4R from R=iPr to R=H can lower the energetic barrier of the epoxide ring-opening step, possibly due to less steric hindrance. Finally, with the of Zn-phen-N4iPr/TBAB system, changing the substrate from PO to SO, the activation energy of the ring-opening step lowers twofold. However, the cyclization barrier was still higher than the cyclization barrier for PO along the α-path.

- An Fe (III)-cyclam derived complex in combination with a nucleophile, TBAB, was found active in CO_2 cycloaddition reaction with epoxides. The reaction was optimized for the benchmark substrate, 1,2-epoxyhexane. Among a series of substrates, the highest increment of 49% conversion over the co-catalyst TBAB was found in case of propylene oxide. A highest TOF 689 h^{-1} was obtained for PO at 100 ^{o}C, 20 bar, and 3h with 0.05/0.25 mol% cat/co-cat ratio. The catalytic system Fe^{III}(c-cyclam-Me,Me)Cl_2]PF_6/TBAB was recycled and reused for the reaction of PO conversion into PC. Based on the types of the substrates, reaction mechanisms were proposed for the formation of cyclic carbonates and/or polycarbonates.

APPENDIX:

Chapter 4

4.A Choice of Solvation Model

The validation of the calculation method was done by comparison with data reported in the literature for the energy profile of the TBAB catalysed cycloaddition of propylene oxide (PO) to CO_2 to form propylene carbonate. The reference studies performed (without solvent) with the DFT method using the B3LYP functional and the 6-31+G(d) basis set, reported an activation barrier of 28.20 kcal mol^{-1} for the system in gas phase[1], and 26.86 kcal mol^{-1} for the path-a (ring-opening at the more substituted carbon, C_a) and 24.51 kcal mol^{-1} for the path-b (ring-opening at the less substituted carbon, C_b) using PCM solvation model in diethyl ether[2] (entries 1 and 2, Table 4A - 1). With the same theoretical method, we obtained an activation barrier for the path-b of 23.23 kcal mol^{-1} (entry 3, Table 4A - 1) which, despite being a result like the reported one, indicates that the method implemented in successive versions of the Gaussian package (versions 09 and 16) is slightly different.

When the zero-point vibrational energy (ZPVE) is included in the calculation, the energy barrier amounts 22.22 kcal mol^{-1} (entry 3, Table 4A - 1), slightly increasing the difference with the reported data. Maintaining the computational parameters (method and geometry) but using a different solvent (2-butanol which has ε closer to the used media

propylene oxide) to better model our experimental conditions, the energy of the barrier obtained is 24.44 kcal mol^{-1} (entry 4, Table 4A - 1). It shows that the polarity of the environment (that changes from ε = 4.24 for diethyl ether to ε = 15.94 for propylene oxide) does not strongly affect the height of the barrier. In fact, the stronger effect on this value comes from the model used to represent the environment: the more recently developed SMD model[3], used in this work, noticeably decreases the value of the barrier (16.09 kcal mol^{-1} in entry 5, Table 4A - 1) when comparing with the results of the previously used PCM (Polarizable Continuum Model).

Table 4A - 1. Validation of the rate-determining step Int1 to TS1 (Figure 4B - 1) activation barrier of TBAB profile using different methods.

Entry	Theoretical Method	Solvation Model/ε	$\Delta G^{\ddagger}$ (Int1→TS1) kcal mol^{-1}	Ref
1	B3LYP/6-31G(d)	No Solvent	$\Delta G^{\ddagger}$ = 28.20	[1]
2	B3LYP-D3BJ/6-311+G (2df,p), SDD for Br // B3LYP/6-31+G*, LANL2DZ for Br.	PCM/diethyl ether (ε = 4.24)	$\Delta G_a^{\ddagger}$ = 26.86 $\Delta G_b^{\ddagger}$ = 24.51	[2]
3	B3LYP-D3BJ/6-311+G (2df,p), SDD for Br // B3LYP/6-31+G*, LANL2DZ for Br.	PCM/diethyl ether (ε = 4.24)	$\Delta G_b^{\ddagger}$ = 23.23§ $\Delta G_b^{\ddagger}$ = 22.22§	Present Work

4	B3LYP-D3BJ/6-311+G (2df,p), SDD for Br // B3LYP/6-31+G (d,p)	PCM/2-butanol (ε = 16)	$\Delta G_b^{\ddagger}$ = 24.44 $\Delta G_b^{\ddagger}$ = 23.72§	Present Work
5	B3LYP-D3BJ/6-311+G (2df,p), SDD for Br // B3LYP-D3/6-31+G (d,p)	SMD/2-butanol (ε = 16)	$\Delta G_b^{\ddagger}$ = 16.73 $\Delta G_b^{\ddagger}$ = 16.09§	Present Work, Present Method

§ Including ZPVE corrections

4.B Study of TBAB-Catalyzed Reaction Mechanism

When studying the reaction catalyzed by TBAB, TBA^+ cation and Br^- anion were placed in a PO environment (described as a polarizable continuum with the SMD model) with an explicit PO molecule to reproduce the interaction of these moieties. For convergence problems in the geometry optimization calculations, in the first steps of the reaction CO_2 energy was calculated as an independent system (also in PO solvent). It was only included in the system together with TBA^+, Br^- and PO for the steps of the reaction where CO_2 has an active role, that is, in intermediates 3 (Int3) and 4 (Int4) and transition state 3 (TS3), as described below.

The Gibbs free energy profile obtained using only TBAB as a catalyst is depicted in Figure 4B - 1. The geometries of the critical points

of this path are shown in Figure 4B - 2. According to our results, this species does not create any interaction with PO. Our reaction profile shows that, in agreement with previous studies[1], the rate-determining step is the initial ring-opening of the epoxide by the nucleophilic attack of Br^- (activation energy $\Delta G^{\#}$= 16.09 kcal mol^{-1}) where a high energetic intermediate is formed (Int2, ΔG= 15.92 kcal mol^{-1}). This is followed by immediate insertion of CO_2 to form the much more stable carbonate species Int3 (ΔG= -1.55 kcal mol^{-1}). No transition state could be located between these last species, indicating that this insertion must be very fast. The next step corresponding to the intramolecular ring closure to form the carbonate had a barrier of 10.88 kcal mol^{-1}. Like in the case of the reactant, the product does not interact with the cation TBA^+, so no desorption process will be necessary. These results are in good agreement with the ones reported in the literature.[2,4]

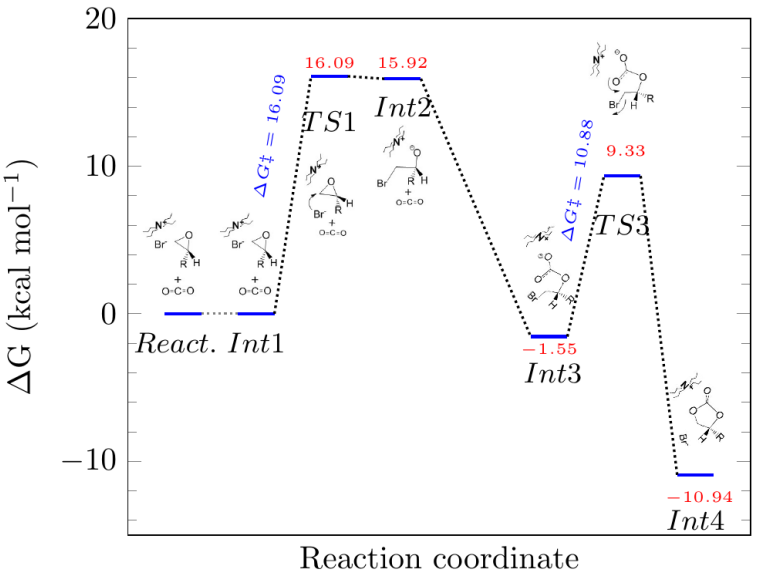

Figure 4B - 1. Gibbs free energy profile for the TBAB-catalyzed reaction.

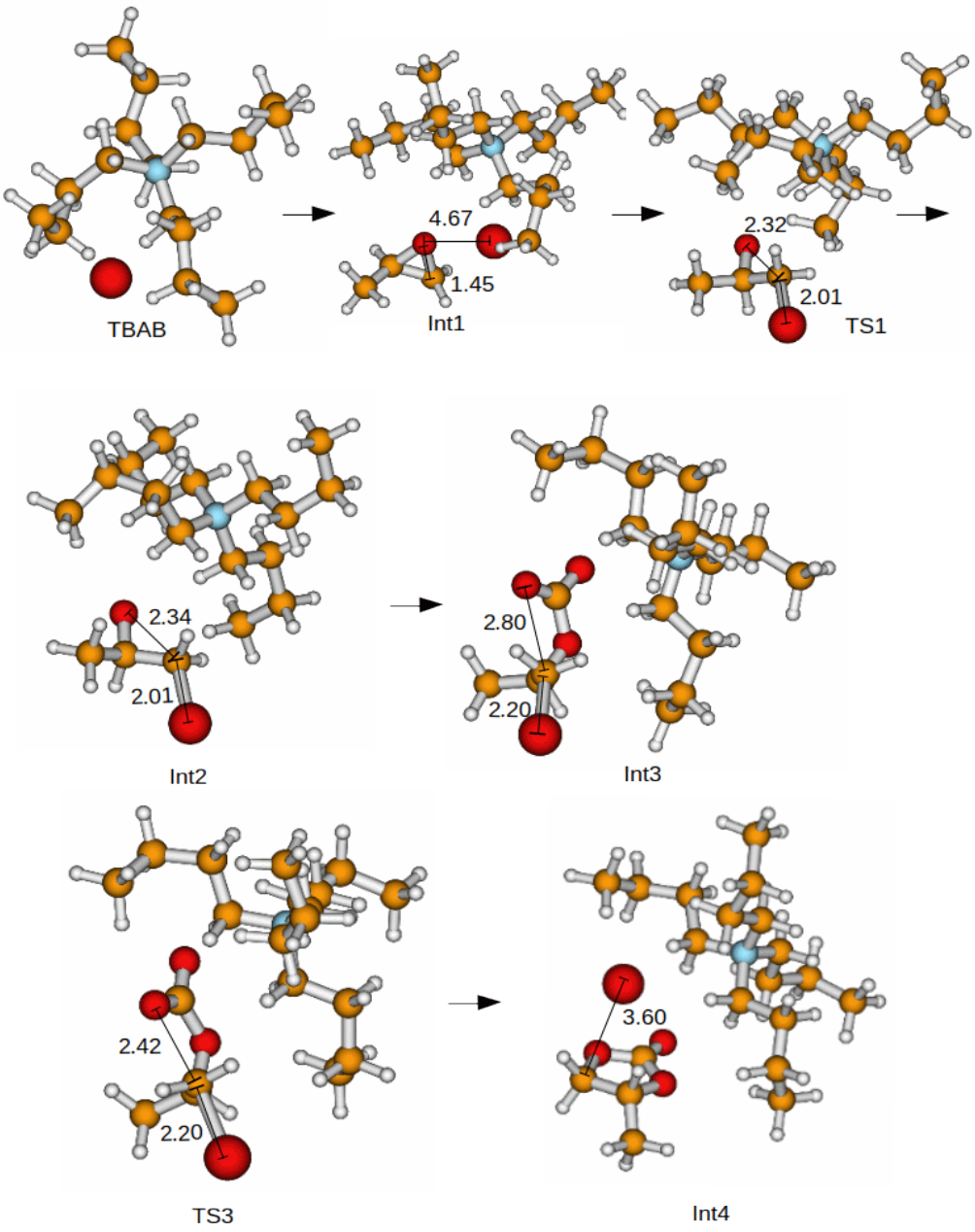

Figure 4B - 2. Geometries of the critical points located along the reaction path of the cycloaddition of CO_2 to propylene oxide, using TBAB as a catalyst. Distances in Å. The orientation of the catalyst has been changed in the different critical points to better show the reactant moiety of the system.

4.C ^{1}H NMR for 1,2-epoxyhexane Conversion into Cyclic Carbonate Catalyzed by HC/TBAB and AIL/TBAB Systems

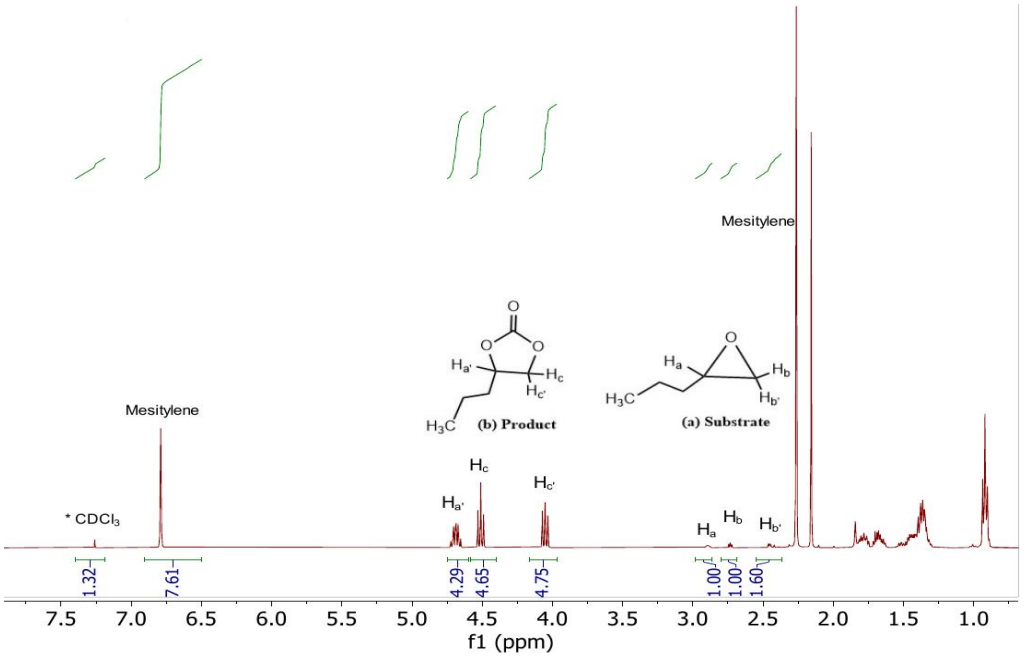

Figure 4C - 1. ^{1}H NMR spectrum (in $CDCl_3$) of reaction crude catalyzed by HC/TBAB (entry 2, Table 4 – 1).

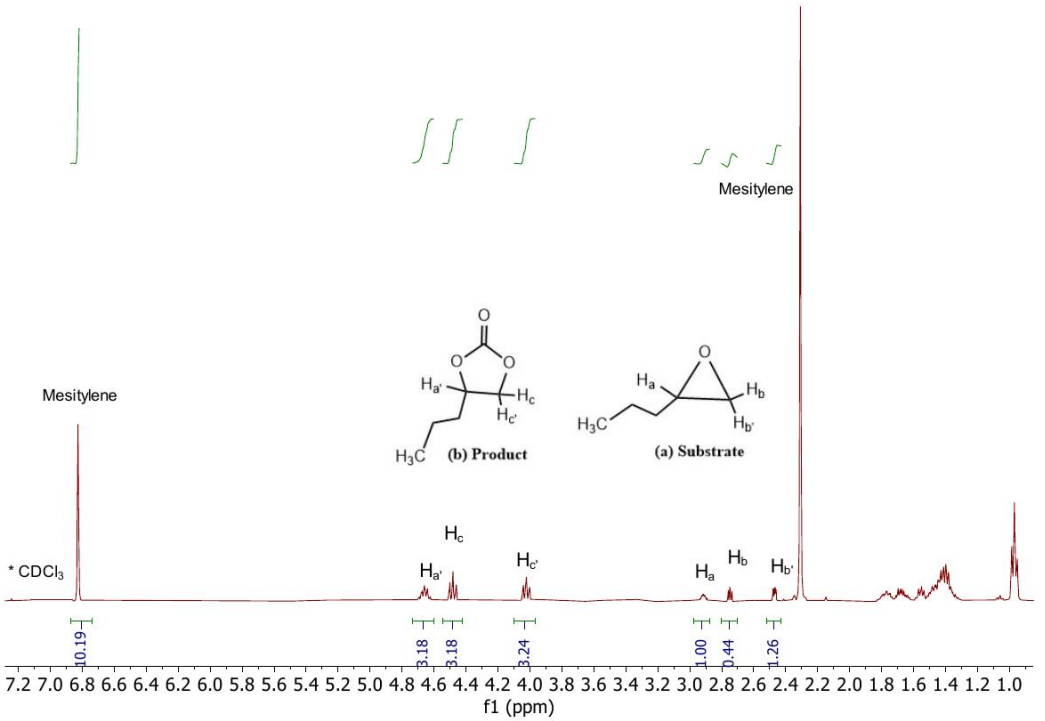

Figure 4C - 2. ^{1}H NMR spectrum (in $CDCl_3$) of reaction crude catalyzed by AIL/TBAB (entry 3, Table 4 – 1).

4.D References

(1) Li, X.; Cheetham, A. K.; Jiang, J. *Mol. Catal.* **2019**, *463*, 37–44.
(2) Hu, T.; Sun, Y.; Ding, Y. *J. CO_2 Util.* **2018**, *28*, 200–206.
(3) Marenich, A. V.; Cramer, C. J.; Truhlar, D. G. *J Phys Chem B* **2009**, *113* (18), 6378–6396.
(4) Foltran, S.; Mereau, R.; Tassaing, T. *Catal. Sci. Technol.* **2014**, *4* (6), 1585–1597.

APPENDIX:

Chapter 5

5.A Additional Computational Techniques

To determine a suitable computational strategy, first we did evaluate the necessity of dispersion correction. Then, we did search an adequate basis set to have a balance between the accuracy of results and the computational cost. With this chosen strategy, we studied the stability of the conformers.

Table 5A - 1 shows the effect of dispersion (D3BJ) on the calculated energies of conrotatory Zn-phen-N4H$_{con}$ and disrotatory Zn-phen-N4H$_{dis}$ model complexes of Figure 5 – 2 and Figure 5 - 3, respectively. At this level of calculation, six-coordinated Zn-phen-N4H$_{con}$ is less stable than its disrotatory counterpart while in case of the five- and four-coordinated Zn-phen-N4H complexes the opposite is true. Finally, the last column shows the change of energy (ΔE) among different Zn-phen-N4H$_{con}$ complexes. Six-coordinated Zn-phen-N4H$_{con}$ is 0.8 kcal mol^{-1} more stable than five-coordinated Zn-phen-N4H$_{con}$ and 4.64 kcal mol^{-1} more stable than four-coordinated Zn-phen-N4H$_{con}$.

Table 5A - 1. Energies (in atomic units, a.u.) of six-, five- and four-coordinated conrotatory (*con*) and disrotatory (*dis*) Zn-phen-N4H complexes at cam-b3lyp/6-31+G(d,p),LanL2DZ(Zn)//cam-b3lyp/6-31+G(d,p), LanL2DZ(Zn) method with SMD solvation, without and with inclusion of D3BJ correction for dispersion effects. ΔE (in kcal mol^{-1}) with respect to the most stable six-coordinated Zn-phen-$N4H_{con}$ energy including D3BJ (E = - 2206.23436512 a.u.).

Coordination No. of Zn	Zn-phen-$N4H_{con}$		Zn-phen-$N4H_{dis}$		ΔE (*Zn-phen-*$N4H_{con}$)
	No D3BJ	D3BJ	No D3BJ	D3BJ	
6	-2206.1589	-2206.2344	-2206.1596	-2206.2350	-
5	-2206.1615	-2206.2331	-2206.1609	-2206.2327	-0.81575
4	-2206.1586	-2206.2270	-2206.1555	-2206.2238	-4.6435

Now, it is known that conrotatory five-coordinated Zn-phen-$N4H_{con}$ complex is more stable than its disrotatory counterpart. Then, Table 5A **-** 2 compares six- and five-coordinated Zn-phen-$N4H_{con}$ complexes calculated at cam-b3lyp/aug-cc-pVDZ//cam-b3lyp/6-31+G(d,p), LanL2DZ(Zn) with an improved basis set aug-cc-pVDZ. These calculations show that five-coordinated Zn-phen-$N4H_{con}$ is 1.066 kcal mol^{-1} more stable than six-coordinated Zn-phen-$N4H_{con.}$

Table 5A - 2. Absolute energy (in a. u.) comparison of six-, and five-coordinated Zn-phen-$N4H_{con}$ complexes at cam-b3lyp-D3BJ/aug-cc-pVDZ//cam-b3lyp-D3BJ/6-31+G(d,p), LanL2DZ(Zn).

Coordination No. of Zn	Absolute energy at cam-b3lyp/aug-cc-pVDZ//cam-b3lyp/6-31+G(d,p), LanL2DZ(Zn)
6	-3920.3631
5	-3920.3648

To find the most stable conformation, the conrotatory Zn-phen-N4H complexes are treated with the method cam-b3lyp-D3BJ/aug-cc-pVDZ which uses even higher basis set, aug-cc-pVDZ and the results are shown in Table 5A - 3. Followed by this method, the five-coordinated Zn-phen-N4H$_{con}$ is found more stable than six-coordinated Zn-phen-N4H$_{con}$ and four-coordinated Zn-phen-N4H$_{con}$, respectively, by 4.96 kcal mol^{-1} and 2.07 kcal mol^{-1}. However, a cheaper cam-b3lyp/6-311+G (2df, p), LanL2DZ(Zn) method also retains the same trend as shown in the Table 5A - 4.

Table 5A - 3. Energies in a.u. and resulted ΔE in kcal mol^{-1} for six-, five- and four-coordinated Zn-phen-N4H$_{con}$ complexes (see Figure 5 - 2) at cam-b3lyp/aug-cc-pVDZ method with SMD solvation. ΔE values in last column are calculated with respect to the most stable five-coordinated Zn-phen-N4H$_{con}$ with D3BJ (E = -3920.31510158 a. u.).

Coordination No. of Zn	Zn-phen-N4H$_{con}$		ΔE
	No D3BJ	D3BJ	
6	-3920.2895	-3920.3072	5-6
			-4.965
5	-3920.2967	-3920.3151	-
4	-3920.2965	-3920.3117	5-4
			-2.077

Table 5A - 4. Absolute energy (in a. u.) comparison of six-, and five-coordinated Zn-phen-N4H$_{con}$ complexes at cam-b3lyp/6-311+G(2df,p), LanL2DZ(Zn).

Coordination No. of Zn	Absolute energy at cam-b3lyp/6-311+G(2df,p), LanL2DZ(Zn)
6	-3920.4829
5	-3920.4864

Finally, Table 5A - 5 collects a detail study of the effect of basis set. As of the Table 5A - 5, cam-b3lyp-D3BJ/aug-cc-pVTZ method is considered as highly accurate method which finds the five-coordinated Zn-phen-N4H$_{con}$ as the most stable Zn-phen-N4H complex.

Table 5A - 5. Effect of various basis sets (without and with dispersion) on the absolute energies (amu) of Zn-phen-N4H$_{con}$ complexes.

Coordination No. of Zn	6-31+G(d,p), LanL2DZ(Zn)		aug-cc-pVDZ		aug-cc-pVTZ	
	No D3BJ	D3BJ	No D3BJ	D3BJ	No D3BJ	D3BJ
6	-2206.1589	-2206.2344	-3920.2895	-3920.3072	-3920.6119	-3920.6872
5	-2206.1615	-2206.2331	-3920.2967	-3920.3151	-3920.6193	-3920.6913
4	-2206.1586	-2206.2270	-3920.2965	-3920.311	-3920.6196	-3920.6876

Table 5A - 6. The distance parameters (in Å) of Zn-phen-N4iPr$_{con}$ compared to Zn-phen-N4iPr$_{dis}$.

Distance parameters	Zn-phen-N4iPr$_{dis}$	Zn-phen-N4iPr$_{con}$
Zn-N1	4.897(7)	4.917(5)
Zn-N2	2.453(3)	2.444(0)
Zn-N3	2.151(7)	2.154(5)
Zn-N4	2.345(1)	2.378(8)
Zn-Cl1	2.368(7)	2.349(9)
Zn-Cl2	2.350(0)	2.345(3)

5.B Screening Conditions of TBAB-Catalyzed CO_2 Cycloaddition

Table 5B - 1 shows the %conversion of the TBAB-catalysed CO_2 cycloaddition with a temperature change from 80 ^oC to 60 ^oC, a pressure drop from 30 bar to 10 bar, and with a decrease in time from 6h to 3h. As can be seen from the Table 5B - 1, the conversion from all these reaction conditions remains in a range from 15% to 26%.

Table 5B - 1. TBAB-catalyzed activity (as a reference) of CO_2 cycloaddition to 1,2 epoxyhexane.

Entry	-/Co-cat (mol %)	T (^oC)	P (bar)	t (h)	Conv[a] (%)
1†	-/0.1	80	30	6	20
2†	-/0.2	80	30	6	26
3†	-/0.2	80	30	3	20
4†	-/0.2	80	10	1	5
5†	-/0.5	80	30	3	22
6†	-/0.5	60	30	6	18
7†	-/0.5	60	10	6	26
8†	-/0.5	60	10	3	15

[a] Averaged conversion determined by ^1H NMR with mesitylene as internal standard

5.C Structures and Mechanisms of Zn-phen-N4H/TBAB-Catalyzed CO_2 Cycloaddition

Scheme 5C - 1 shows the chemical constituents of the model catalytic reaction of Zn-phen-N4H/TBAB-catalyzed CO2 cycloaddition to PO. The reactant state contains the catalyst, Zn-phen-N4H, a bromide anion (representing the co-catalyst, TBAB), and the model substrate PO. Similarly, to the path for the reaction catalyzed by Zn-phen-N4iPr, the insertion of CO_2 into the system leads to the intermediate Int1. With Zn-phen-N4H as catalyst, the change in Gibbs free energy is 2.05 kcal mol^{-1}.

The mechanism and species involved in the Zn-phen-N4H/TBAB-catalyzed CO_2 cycloaddition to PO is like that of Zn-phen-N4iPr/TBAB, as discussed in section 5.5.1. From Int1 on, two different paths were explored: α-path and β-path. The α-path leads to the product cyclic carbonate without any changes in the catalyst structure while along the β-path a structural change in the catalyst takes place, the dissociation of an axial chlorido ligand.

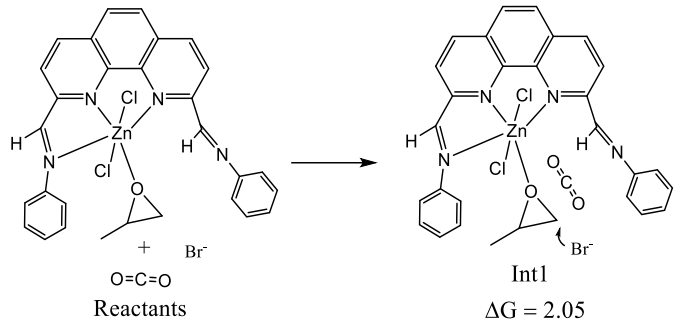

Scheme 5C - 1. Initial geometry of the Zn-phen-N4H/TBAB-catalyzed CO_2 cycloaddition reaction. Gibbs free energy change is shown in kcal mol^{-1}.

Scheme 5C - 2 shows the structural details of all the species (intermediates and transition states) of the elementary steps of the of Zn-phen-N4H/TBAB-catalyzed CO_2 cycloaddition to PO, following the α-path. Going from Int1 to Int2α, the transition structure, TS1, shows the nucleophilic attack to the less-hindered carbon of PO while the epoxide ring is opening. Then, in the step from Int2α to Int3α, the TS2α takes the CO_2. Finally, in the step from Int3α to the product, the TS3α makes a cyclization of the produced alkoxide, a five membered ring is formed

while the nucleophile is released. At the same time, the reactive part gets de-coordinated from the catalyst center, in a concerted manner.

On the other hand, Scheme 5C - 3 shows the structural details of all the elementary steps of the of Zn-phen-N4H/TBAB-catalyzed CO_2 cycloaddition to PO, followed by β-path. Going from Int1 to Int2β in the β-path, unlike the α-path, an axial chlorido ligand dissociates at the Int2β followed by same TS1, as in the α-path. Then, in the next step, the Int3β is reached from Int2β followed by the TS2β, with a similar reactive site as of TS2α. After that, in the step going from Int3β to Int4β, the TS3β make a cyclization of the reactive part but, unlike the α-path, keeps the reactive part coordinated to the Zn-center.

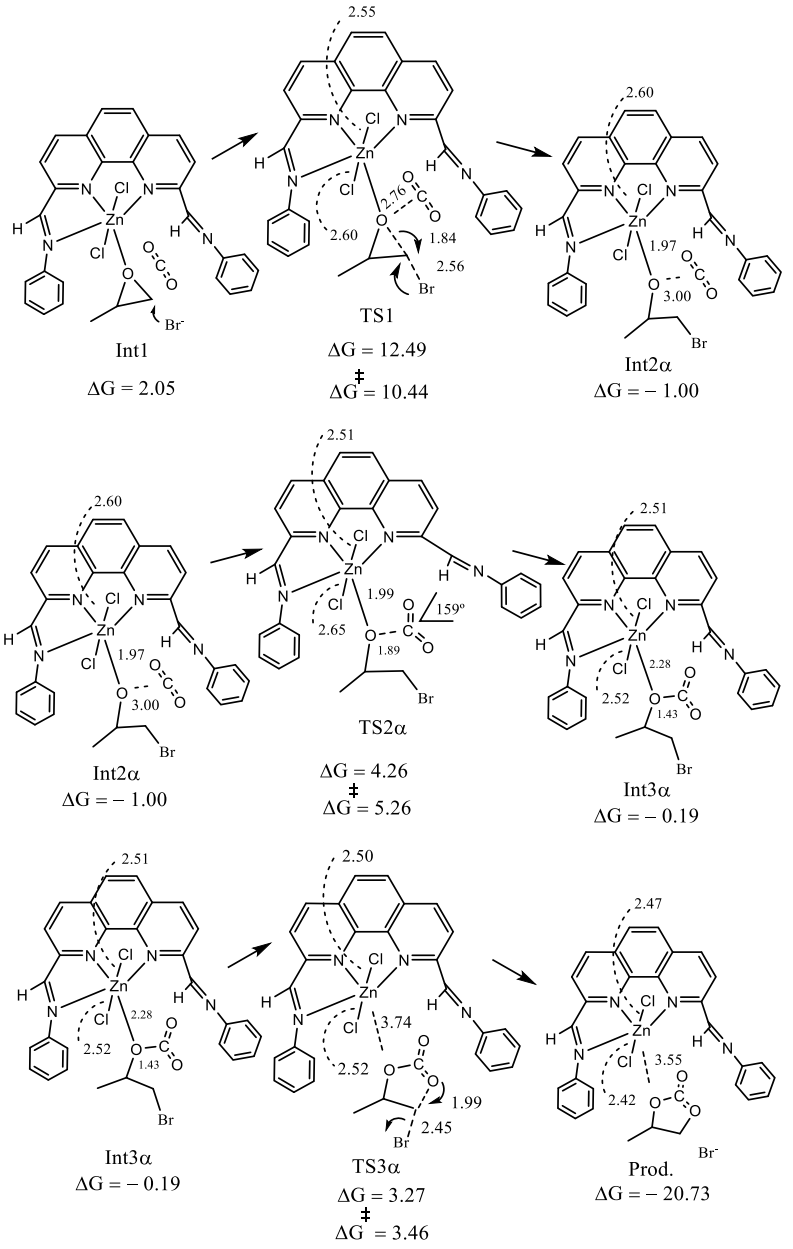

Scheme 5C - 2. Elementary steps of Zn-phen-N4H/TBAB-catalyzed CO_2 cycloaddition followed by α-path. Gibbs free energy change is shown in kcal mol^{-1} and the distances in Å.

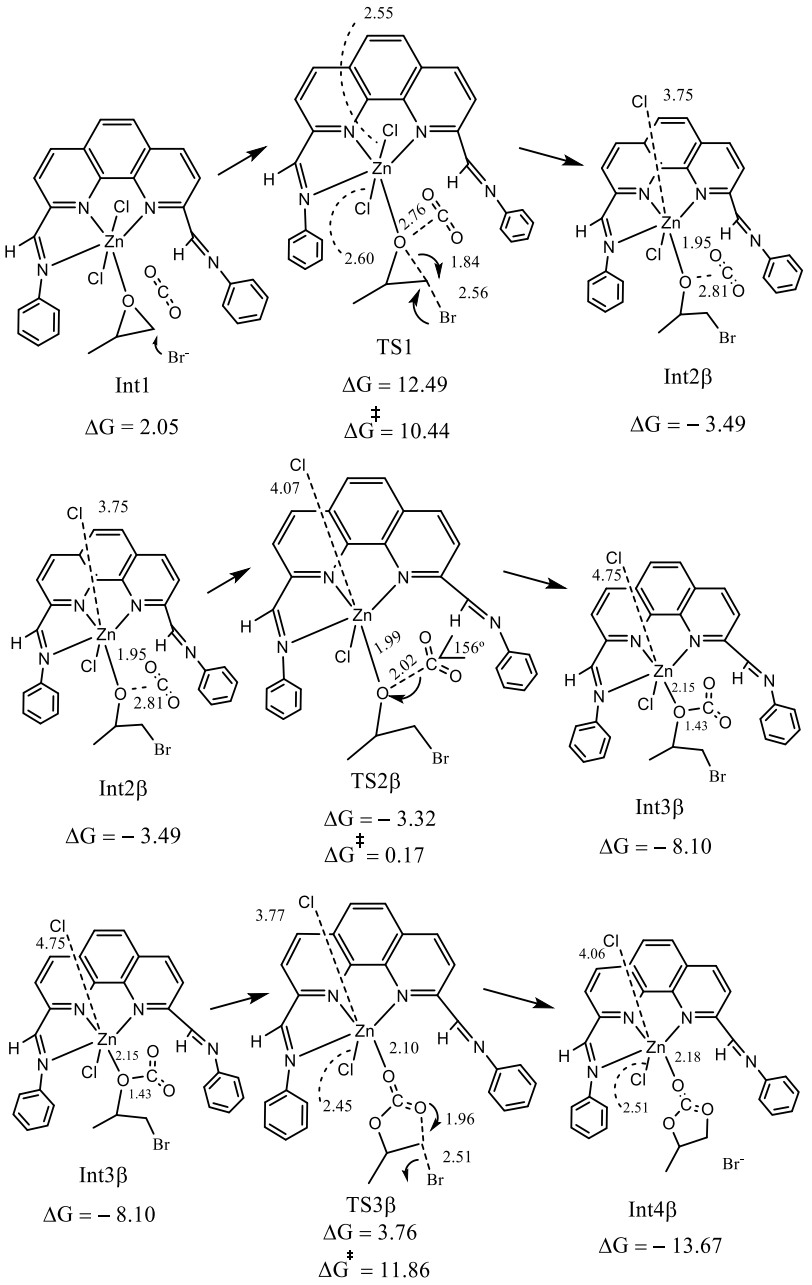

Scheme 5C - 3. Elementary steps of Zn-phen-N4iPr/TBAB-catalyzed CO_2 cycloaddition followed by β-path. Gibbs free energy change is shown in kcal mol^{-1} and the distances in Å.

5.D ^{1}H NMR of Zn-phen-N4iPr/TBAB-Catalyzed CO_2 Cycloaddition to EPH, PO, SO, and ECH.

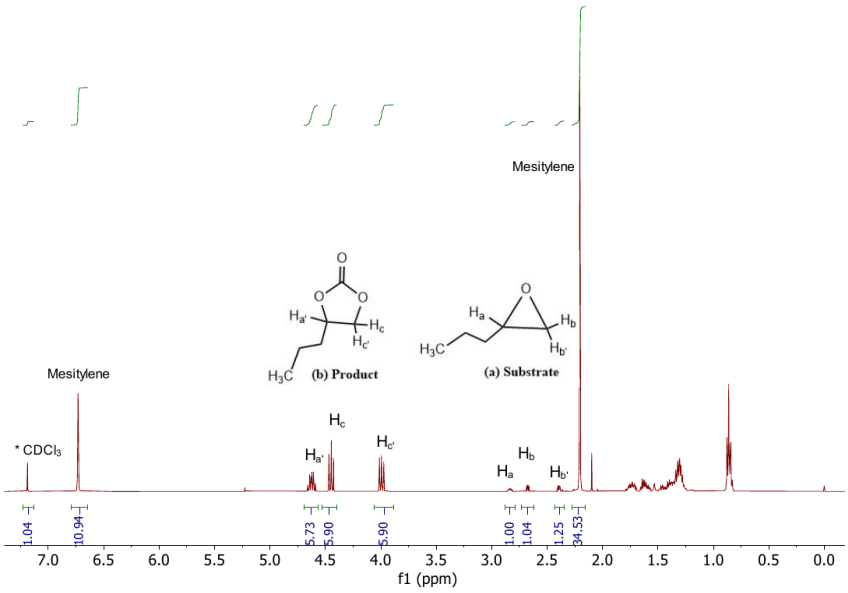

Figure 5D - 1. ^{1}H NMR spectrum (in $CDCl_3$) of Zn-phen-N4iPr/TBAB catalyzed CO_2 cycloaddition to EPH (entry 1, Table 5 – 4).

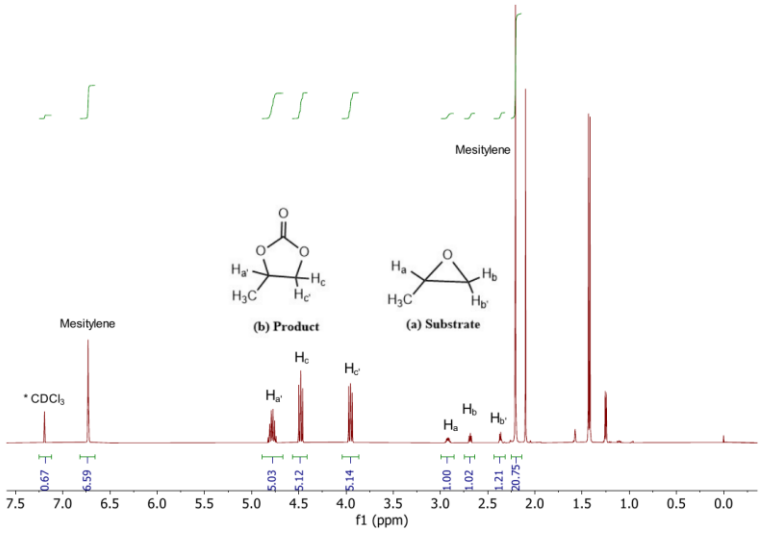

Figure 5D - 2. ^{1}H NMR spectrum (in $CDCl_3$) of Zn-phen-N4iPr/TBAB catalyzed CO_2 cycloaddition to PO (entry 3, Table 5 – 4).

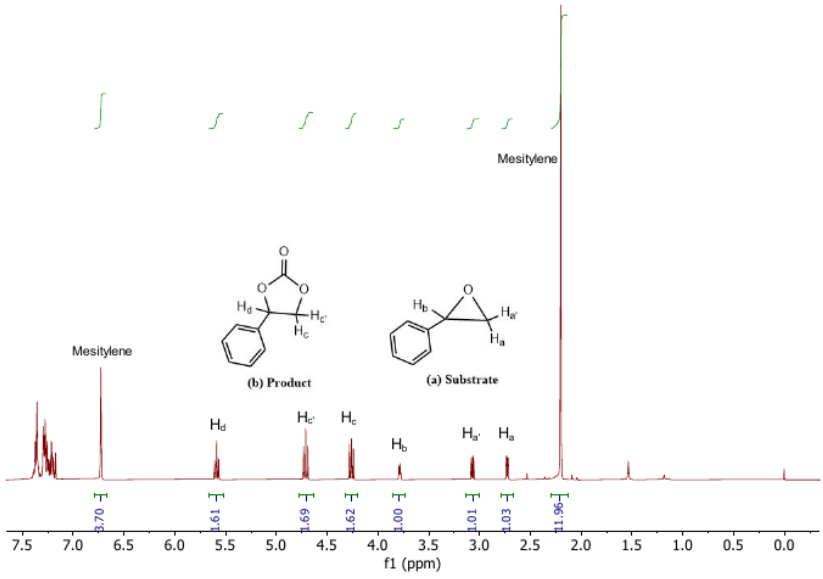

Figure 5D - 3. ^{1}H NMR spectrum (in $CDCl_3$) of Zn-phen-N4iPr/TBAB catalyzed CO_2 cycloaddition to SO (entry 5, Table 5 – 4)

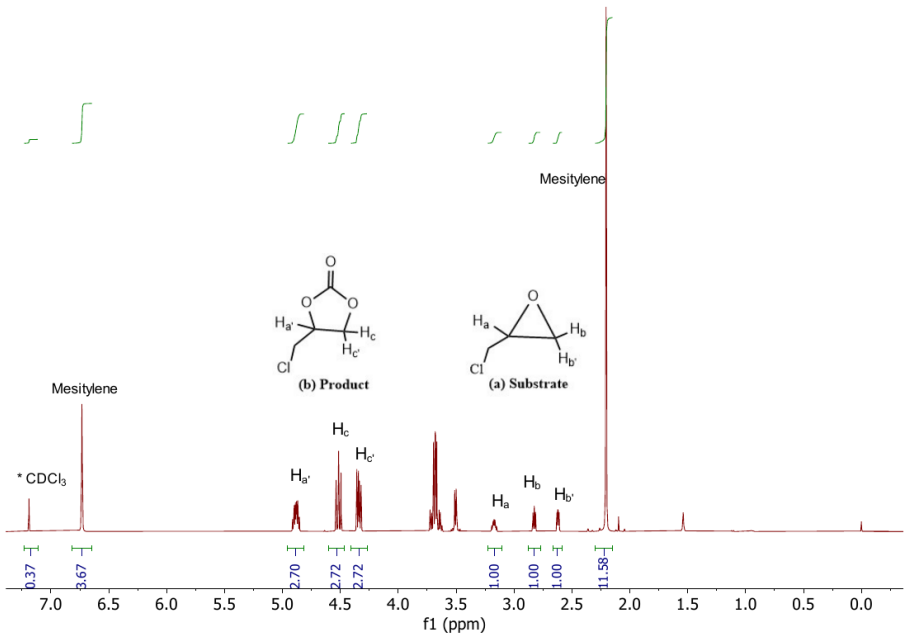

Figure 5D - 4. ^{1}H NMR spectrum (in $CDCl_3$) of Zn-phen-N4iPr/TBAB catalyzed CO_2 cycloaddition to ECH (entry 7, Table 5 – 4).

5.E References

(1) Li, X.; Cheetham, A. K.; Jiang, J. *Mol. Catal.* **2019**, *463*, 37–44.
(2) Hu, T.; Sun, Y.; Ding, Y. *J. CO_2 Util.* **2018**, *28*, 200–206.
(3) Marenich, A. V.; Cramer, C. J.; Truhlar, D. G. *J Phys Chem B* **2009**, *113* (18), 6378–6396.
(4) Foltran, S.; Mereau, R.; Tassaing, T. *Catal. Sci. Technol.* **2014**, *4* (6), 1585–1597.

APPENDIX:

Chapter 6

6.A ^{1}H NMR of [Fe^{III}(c-cyclam-Me,Me)Cl_2]PF_6/TBAB-Catalyzed CO_2 Cycloaddition to EPH, PO, SO, ECH and CHO.

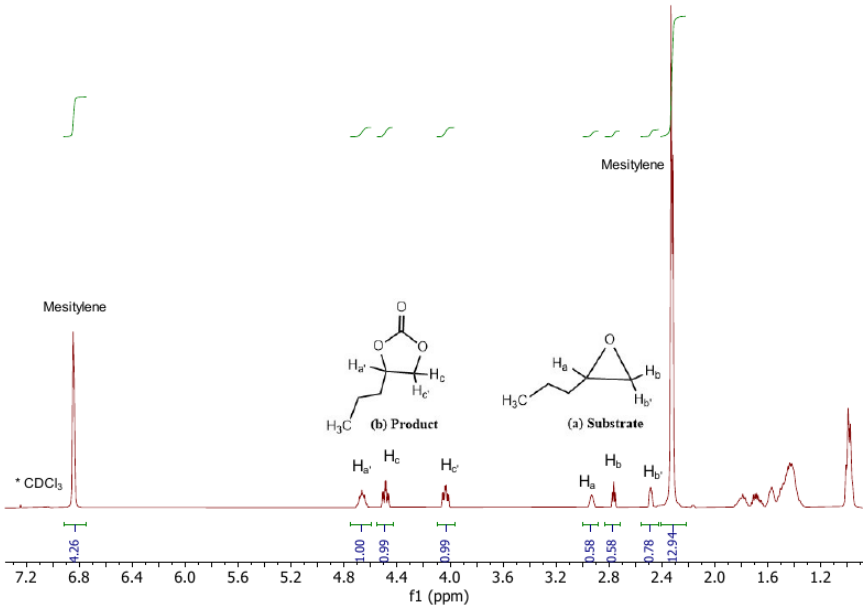

Figure 6A - 1. ^{1}H NMR spectrum (in $CDCl_3$) of [Fe^{III}(c-cyclam-Me,Me)Cl_2]PF_6/TBAB catalyzed CO_2 cycloaddition to EPH (entry 2, Table 6 – 3).

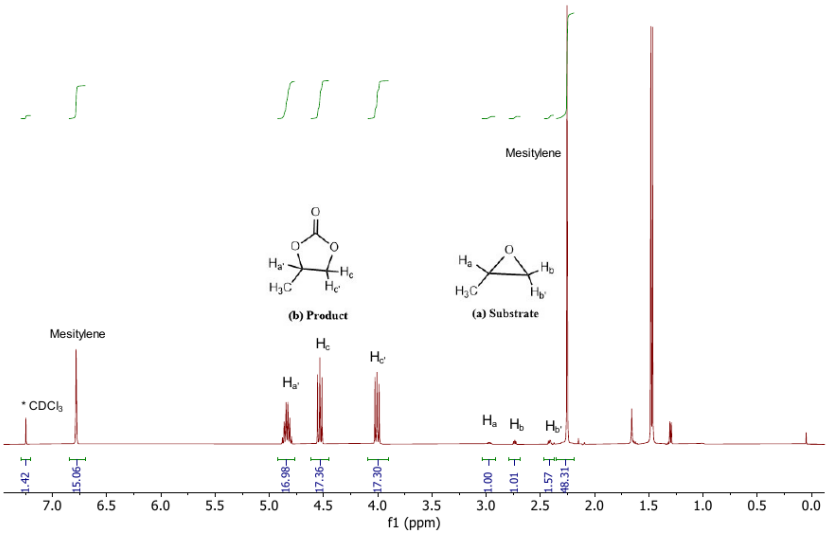

Figure 6A - 2. ^{1}H NMR spectrum (in $CDCl_3$) of $[Fe^{III}$(c-cyclam-Me,Me)$Cl_2]PF_6$/TBAB catalyzed CO_2 cycloaddition to PO (entry 4, Table 6 – 3).

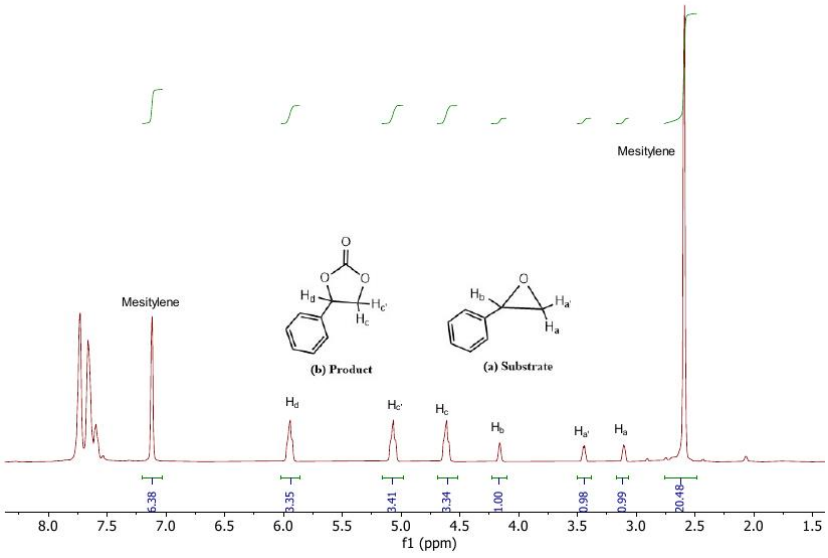

Figure 6A - 3. ^{1}H NMR spectrum (in $CDCl_3$) of $[Fe^{III}$(c-cyclam-Me,Me)$Cl_2]PF_6$/TBAB catalyzed CO_2 cycloaddition to SO (entry 6, Table 6 – 3).

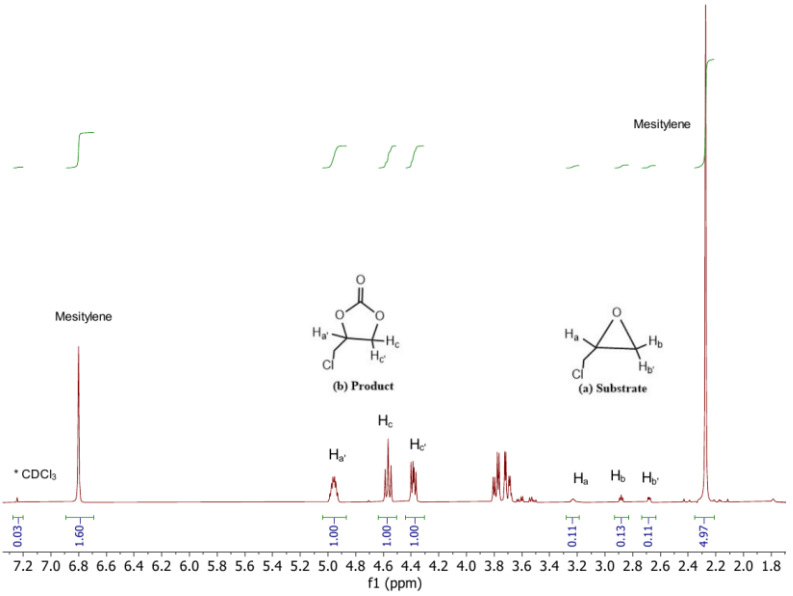

Figure 6A - 4. ^{1}H NMR spectrum (in $CDCl_3$) of $[Fe^{III}$(c-cyclam-Me,Me)$Cl_2]PF_6$/TBAB catalyzed CO_2 cycloaddition to ECH (entry 8, Table 6 – 3).

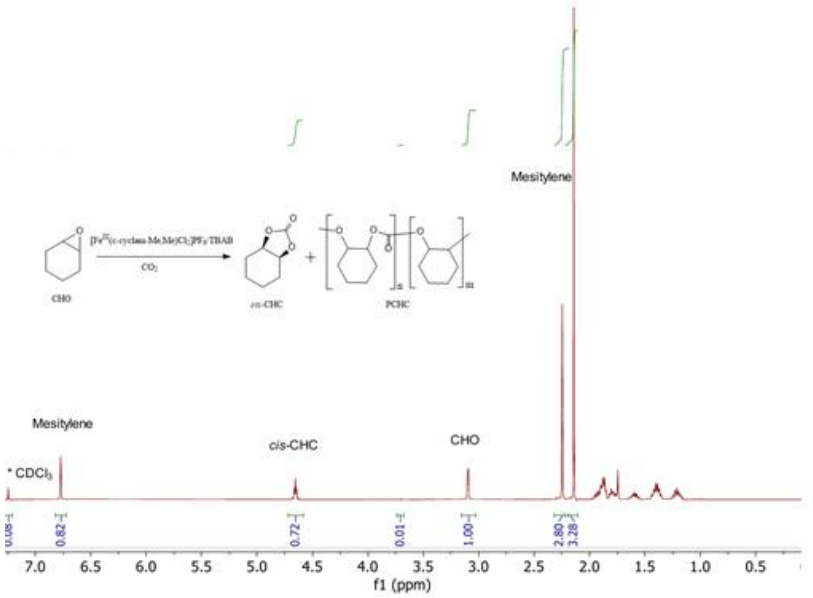

Figure 6A - 5. ^{1}H NMR spectrum (in $CDCl_3$) of $[Fe^{III}$(c-cyclam-Me,Me)$Cl_2]PF_6$/TBAB catalyzed CO_2 cycloaddition to CHO (entry 10*, Table 6 – 3).

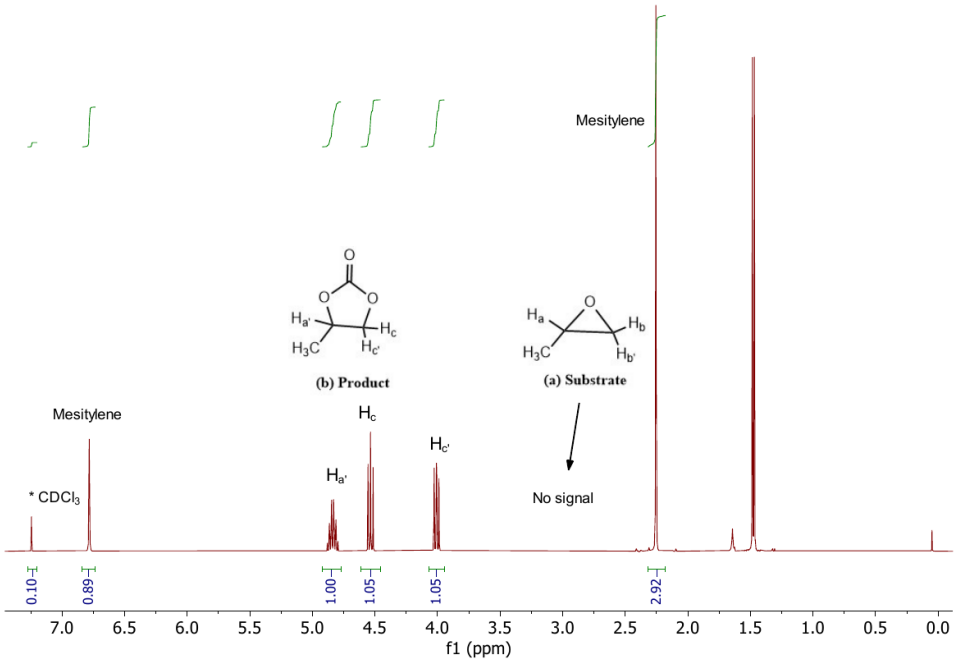

Figure 6A - 6. ^{1}H NMR spectrum (in $CDCl_3$) of distilled propylene carbonate (PC) from the experiment corresponding to Figure 6A - 2.

APPENDIX:

Scientific Contributions

Article Published:

El Ouahabi, M. S.; Yeamin, M. B.; Rivas, R.; El Guemmout, F.; Reguero, M.; Masdeu-Bultó, A. M.; Aghmiz, A. Lignocellulosic Residues as Catalysts for CO_2 Fixation: Complementary Experimental and Computational Approaches. *Cellulose* **2020**, *28*, 359-375. https://doi.org/10.1007/s10570-020-03522-x.

Manuscript in Preparation:

Yeamin, M. B.; Redondo, C. L, El Aouni, N.; Reguero, M.; Masdeu-Bultó, A. M. CO_2 Cycloaddition by Zn-phen-N4 Complexes: Catalyst Development through Mechanistic Studies. *Manuscript in preparation*.

Review Published:

Claver, C.; Yeamin, M. B.; Reguero, M.; Masdeu-Bultó, A. M. Recent Advances in the Use of Catalysts Based on Natural Products for the Conversion of CO2 into Cyclic Carbonates. *Green Chem* **2020**, *22* (22), 7665–7706. https://doi.org/10.1039/D0GC01870H.

UNIVERSITAT ROVIRA I VIRGILI
CATALYTIC CO2 CYCLOADDITION WITH EPOXIDES INTO CYCLIC CARBONATES: SYNERGIES FROM COMPUTATIONAL TO EXPERIMENTAL STUDIES
Md Bin Yeamin

UNIVERSITAT
ROVIRA i VIRGILI